Shaping of Biodegradable Bone Implants Using Computer Numerically Controlled (CNC) Multi-Axis Machining

by

Amir Hessam Rouzrokh

A thesis
presented to the University of Waterloo
in fulfillment of the
thesis requirement for the degree of
Master of Applied Science
in
Mechanical Engineering

Waterloo, Ontario, Canada, 2008

Author's Declaration for Electronic Submission of a Thesis

I hereby declare that I am the sole author of this thesis. This is a true copy of the thesis, including any required final revisions, as accepted by my examiners.

I understand that my thesis may be made electronically available to the public.

Amir Hessam Rouzrokh, 2008

Abstract

This thesis presents the use of Computer Numerically Controlled (CNC) machining as a method to manufacture anatomically-shaped synthetic grafts made from Calcium Polyphosphate (CPP) ceramic. Tissue-engineered cartilage is grown on the surface of these implants *in vitro* followed by *in vivo* implantation in the host's body for osteochondral focal defect repair. While most current implants are manufactured from simple geometries and are not specific to one patient's need, it is believed that custom manufactured implants (from computer tomography data) representing the exact shape of the original bone will be beneficial. This is because custom implants permit an even stress distribution on the cartilage, resulting in increased cartilage survival rates. The present study has successfully manufactured and delivered a custom designed implant with sufficient surface porosity and minimal chipping. This was accomplished by effectively modeling the machinability characteristics and finding the optimal cutting conditions for CPP.

CPP's machinability characteristics were investigated and a cutting force prediction model was developed. This model was verified by a comparison of experimental and predicted forces for a number of ball and flat endmilling tests. The optimal cutting conditions that would result in maximum surface porosity and minimal chipping were established through qualitative investigation of results from varied conditions using Scanning Electron Microscope (SEM) images. Using the established optimal cutting conditions from machinability studies, the multi-axis machining process for producing the designed custom implant was developed and all stages were simulated for accuracy and integrity of the final implant.

The designed toolpaths were tested on prototyping wax and verified against the actual Computer Aided Design (CAD) model using an optical microscope. The same toolpaths were executed on a block of CPP and the final implant was again investigated for surface

porosity and chipping. After final comparison against the CAD model using an optical microscope, the implant was delivered to surgeons for implantation.

Acknowledgements

First of all, I would like to thank God for all that he has given me, which is all I have and all I am.

I would like to express my sincere appreciation toward my supervisor for all his guidance and help in completing my studies here at University of Waterloo. Also, I thank my reader committee members Prof. Ehsan Toyserkani and Prof. Naveen Chandrashekar for their review and constructive feedback on this thesis. Also, this project would not have started without the contributions of Prof. Pilliar, Prof. Kandel, and Prof. Grynpas from University of Toronto, whom I extend my sincere appreciation to. I would also like to express my sincere appreciation here to Robert Wagner, for his tremendous help in machining of the implants.

I would like thank my mom, Pari, as I would have not been anything without her love and guidance, and my father, Mohammad, for providing constant support and guidance for his children. I would like to thank my sister, Mahsa, whom I grew up and shared my life, happiness, and sadness with, and my brother Ali, whom I have always looked up to and has really been the big brother for me all my life. I would also like to thank all my relatives and friends for all their support and care including Dayna for proofreading my thesis, and especially Lisa for her help with my seminar preparation and editing of this thesis.

Table of Contents

List of Figures

List of Tables

Nomenclature

a	Axial depth of cut
β	Helix angle
c	Feed per tooth
D	Cutter diameter
$F_t(\phi)$, $F_r(\phi)$, $F_a(\phi)$	Tangential, radial, and axial cutting force acting on the cutting edge
$\overline{F_x}$, $\overline{F_y}$, $\overline{F_z}$	The average cutting force per tooth period in the x-, y-, and z-direction.
F_x, F_y, F_z	The total force in the feed (X), normal (Y), and axial (Z) direction.
h	Instantaneous chip thickness
K_{tc}, K_{rc}, K_{ac}	Milling shear component of cutting force coefficients in tangential, radial, and axial directions
K_{te}, K_{re}, K_{ae}	Milling edge component of cutting force coefficients in tangential, radial, and axial directions
N	Number of flutes
ϕ	Angular immersion of the cutting edge
ϕ_p	Cutter pitch angle
ϕ_{st}	Start angle of a cut
ϕ_{ex}	Exit angle of a cut

Chapter 1

Introduction

1.1   Implant as a Treatment Option

The human body and in general, a living being, has a unique ability to heal itself against many natural and non-natural injuries and degradations that occur throughout its period of life. Focusing on joint and cartilage related issues, one study done between 1997 and 1999 on 1000 patients in Norway [1] found the mean chondral (cartilage related) or osteochondral (bone and cartilage related) total defect area to be 2.1 cm^2 (range, 0.5 to 12; standard deviation 1.5). The main focal chondral or osteochondral defect was found on the medial femoral condyle in 58%, patella in 11%, lateral tibia in 11%, lateral femoral condyle in 9%, trochlea in 6%, and medial tibia in 5% [1]. The healing ability of human joints, however, is dependent on the severity of the defect. In humans, if damage to the articular cartilage (i.e. the surface of the synovial joint) exceeds a critical size in area, then the self-healing capability of the joint is insufficient, causing the joint to be impaired from comfortable functioning [2][3].

Today, many different approaches exist for healing focal defect trauma ranging from non-invasive therapeutics and medication prescription to a full joint replacement surgery. In this surgical process, known as total joint arthroplasty (TJA), the synovial

joints are replaced with a natural or synthetic graft that improves joint functionality in comparison with the host's original damaged joint. The replacement joints can be either harvested from the patient's own body (autografts), from another host (allografts), or be synthetic. Unfortunately, statistical reports show that this procedure has high rates of failure. For instance, in the total hip replacement surgeries performed from 1986 until 1995 in Sweden, clinical failure rates were 10 to 20% (based on the failure criteria) [4].

With high failure rates and many complications involved in these synthetic graft replacement surgeries, researchers have been investigating new materials that better resemble the natural characteristics of autografts. Autografts are *Osteoconductive* (i.e. the bone can communicate and grow over the surface) [5]*, Osteoinductive* (i.e. have the ability to induce differentiation of pluriopotential stem cells to an osteoblastic phenotype) [5], *Osteointegrative* (i.e. have the ability to initiate chemical bonding with the bone without the requirement of a tissue layer coating) [5], and *Osteogenesis* (i.e. also have the ability to generate bone from osteoblastic cells remaining in the substrate) [5]. Osteoblastic cells are responsible for the synthesis and mineralization of bone during both initial bone formation and later bone remodelling. Since, currently, no synthetic material posseses all of the above characteristics (and at best only holds osteointegrative and osteoconductive properties), there has been an effort in developing certain procedures that are not total replacement surgeries but rather focus on healing the local trauma, such as repairing of the deteriorated cartilage area. This has resulted in an approach in which tissue-engineered cartilage is grown on the surface of a suitable material with similar characteristics to autografts *in vitro* (in an artificial environment outside of the living organ) and then used for local *in vivo* (within the living organism) implantation (Figure 1-1).
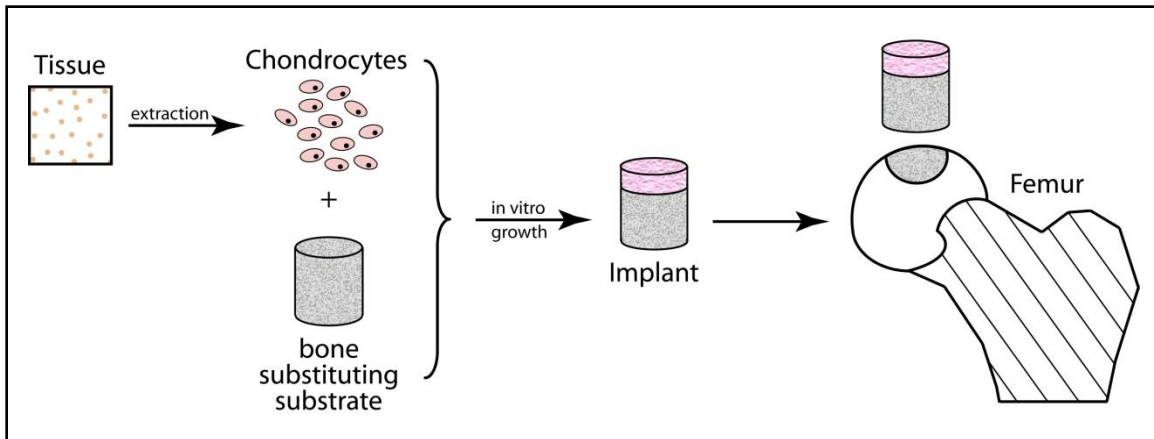
Figure 1-1: Local cartilage defect repair method with *in vivo* implantation of an *in vitro* grown tissue-engineered cartilage [6]

Recent research to the viability of this method has shown promising results [7][8][9][10][11] and has been a proposed treatment for severe osteoarthritis treatment [7].

1.2   Biodegradable CPP as Implant Material

A recent animal study has shown that Calcium Polyphosphate (CPP) is a suitable candidate as material for a biphasic implant [7]. A biphasic implant is an implant in which cartilage has grown on the porous surface *in vitro* and then is implanted *in vivo*. Recent studies at the University of Toronto have shown promising results [12][13], with superior biocompatibility [13], good degradation rate in the host body [14], rapid bone formation [12], usage as tissue-engineered cartilage base [15] and cartilage growing on the open porous surface of the CPP substrate [16]. One important factor in the success of this implantation procedure with CPP is the required geometrical matching that must exist, and the detailed effect of geometrical consistency is yet to be further investigated [17]. The geometrical mismatch has resulted in local cartilage deterioration in some study cases [7], and it has been suggested that this was the result of elevated stress due to stress

concentration at that point [18]. It is important to have the surface of the implanting CPP possess the same geometrical surface as the original implant [19], and therefore in this thesis, the goal is to construct the implant's surface to match the original bone geometry with high accuracy levels. Also, CPP's porosity must be maintained during this operation to enable cell ingrowth, as stated earlier in this section.

1.3   Thesis Goal

The goal of this thesis is to investigate the machinability of CPP as a new biomedical material suitable for implantation. Since surface porosity is vital to cell growth, it must be established that machining as a fabrication process of the implant does not block the porous surface. After establishing the right cutting conditions for surface porosity maintenance, a mechanistic model is developed to predict cutting forces. This enables the prediction of cutting forces during the whole machining process, ensuring that forces are held below the CPP breakage limit at all times.   Using results of the machinability studies, multi-axis toolpaths were developed, followed by testing of the toolpaths on prototyping wax and then actual machining of the implant. An investigation of the dimensional accuracy and surface porosity of the final implant concludes this study.

1.4   Thesis Layout

A literature review of material relating to implants and specifically CPP as implant material will be presented in Chapter 2. Chapter 3 will start with investigation of surface porosity and the effects of machining on this property of CPP. The underlying theory for the mechanistic model that predicts the cutting forces in milling operations will then be presented. This model will then be verified for accuracy at different feed rates, and this will be followed by a search for optimal cutting conditions to prevent surface porosity

loss and chipping. This chapter will then be concluded by introducing the optimal cutting conditions that will be put into use later in actual cutting. Chapter 4 will present toolpath design, machining parameters, and tools used in the shaping process of the implant. Also in this chapter, investigation of the result of the actual machining is presented and the final implant is checked for dimensional accuracy. Chapter 5 presents the conclusions and summary for the thesis, and some recommendations for future work.

Chapter 2

Literature Review

An ideal bone implant should have four main characteristics: It is (i) to be osteointegrative, that is, it must have the ability to chemically bond with the surface of the bone without the need of a fibrous tissue coating on the surface of the implant; (ii) to be osteoconductive, that is, to have the ability to support the growth of bone on its surface; (iii) to be osteoinductive, which is the ability to induce differentiation of pluripotential stem cells from surrounding tissue to an osteoblastic phenotype; and lastly (iv), to be osteogenesis, which is the formation of new bone with osteoblastic cells being present within the graft material. While only autogenous bone graft satisfies all the above conditions, synthetic bone grafts at most are only osteointegrative and osteoconductive [5]. While there are many different classes of synthetic bone graft material such as bioactive glass, glass ionomer, aluminum oxide, calcium sulphate and calcium phosphate, the main concern in this thesis is with a specific type of ceramic known as Calcium PolyPhosphate (CPP). The chemical formula for this substance is $Ca(PO_3)_2$ [20], and several research articles show that CaP ceramics are a viable choice as bone graft material [21][22][23][24]. However, they have non-complying mechanical properties when compared to cancellous bone tissue, having strength, fracture toughness, and fatigue resistance less than that of the natural bone tissue. Yet CPP is porous, and therefore, chondrocytes can enter into the pores and cartilage that forms in this region anchors the tissue to the CPP. There is some potential benefit in using CPP as a biphasic

6

construct [7]. Lateral integration into adjacent natural native cartilage is possible immediately after implantation. With CPP being porous, bone grows in pores not filled by cartilage after implantation, which results in the implant being secured and fixed in place [12][25]. CPP is biodegradable and will be replaced by bone ultimately with degradation products being calcium and phosphates which does not cause inflammatory reaction [12][25].

2.1   Calcium Phosphate (CaP)

As stated previously, there are mechanical deficiencies related to CaP group of biomaterials. As a result, usage of this material as graft substance has been limited in areas where the bone is load carrying, and they are inferior in resistance against tensile or torsional stresses [26]. An observed general trend in CaP materials is that the alteration of characteristics such as chemical composition, degree of crystallization, and porosity affects the degradation process and mechanical properties in an indirect manner. In other words, both higher density and higher extent of crystallization results in improved mechanical behaviour, while the degradation rate slows down significantly [26][27]. The sintering process, shown in Figure 2-1, determines the density of the resulting CaP. Depending on the sintering temperature, dwell time, and particle size a wide range of densities can be produced ranging from very porous (35-40%) to a fully dense structure for CaP [12] [28][29].
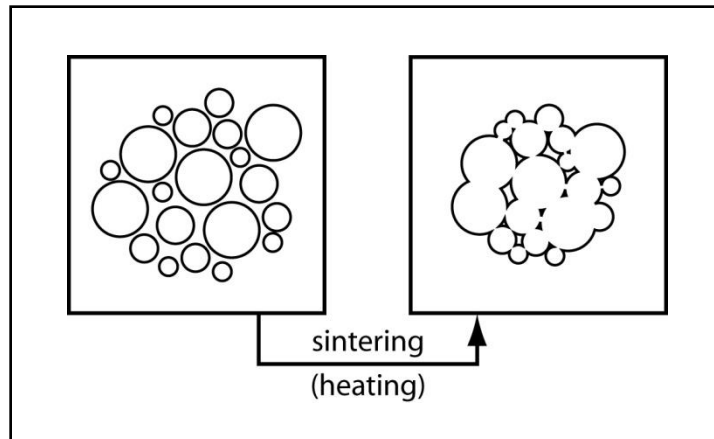
Figure 2-1: A schematic representation of the change of the particles during a sintering process [30]

2.2 Calcium Polyphosphate (CPP)

A family of condensed phosphates known as Calcium Polyphosphates (CPP) with a chemical formula of $[Ca(PO_3)_2]_n$ has shown promising biomaterial characteristics for grafting purposes [12][13][14]. CPP powder can be filtered to have certain particle sizes, and then a sintering process may be implemented to have blocks of CPP with required densities and particle sizes, again, depending on the sintering parameters. The following chemical process is started in a furnace at 500°C for 10 hours on the precursor powder:

$$n\ \text{Ca(H}_2\text{PO}_4)_2 \cdot \text{H}_2\text{O} \xrightarrow{\ 500\ °\text{C}\ } [\text{Ca(PO}_3)_2]_n + 3n\ \text{H}_2\text{O}$$
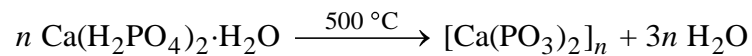
in which afterwards the resulting powder is melted at 1100°C to produce an amorphous glass and held so for another 1 hour to induce chain lengthening [27]. By quenching this material in distilled water, the resulting frit is milled and then passed through a series of mesh to separate desired particle sizes.

8

There have been research studies conducted on the biocompatibility, degradation speed, and the bone growth infiltration, both *in vitro* and *in vivo* [12][25]. Bone ingrowth for CPP was also established in a separate study [13].

One of the most important and distinct bio-features of CPP is the ability for cartilage to grow on its surface [15][31][32]. Recent studies show that *in vivo* cartilage growth on the surface of CPP in sheep models results in improved mechanical properties of this new formed cartilage [7], and all this suggests CPP as a potential candidate for bone-substituting graft as a tissue engineered substrate. The elastic modulus of CPP was 0.35MPa in a short term *in vivo* implantation (3-4 months), and 0.54MPa in long term (9 months) [7].

2.3 Machining as a Ceramic Substrate Manufacturing Method

As discussed in the previous section, CPP comes in a powder form before being sintered. One of the suggested methods of manufacturing of a synthetic graft was using rapid prototyping, in which layer by layer, powder and binder are deposited and therefore, the final spatial shape will be generated. This method of manufacturing has been investigated by Wei [6] and this process is further under investigation at the Rapid Prototyping Laboratory at University of Waterloo (rpl.uwaterloo.ca).

The method that is investigated in this thesis is machining and in particular, using multi-axis milling as the main machining process. Milling is one of the most widely used shaping methods in today's industry and while most of the materials being machined are engineering materials such as aluminium and steel, ceramics have also been investigated for machinability and milling. Some of the most widely used milling operations are shown in Figure 2-2.

9
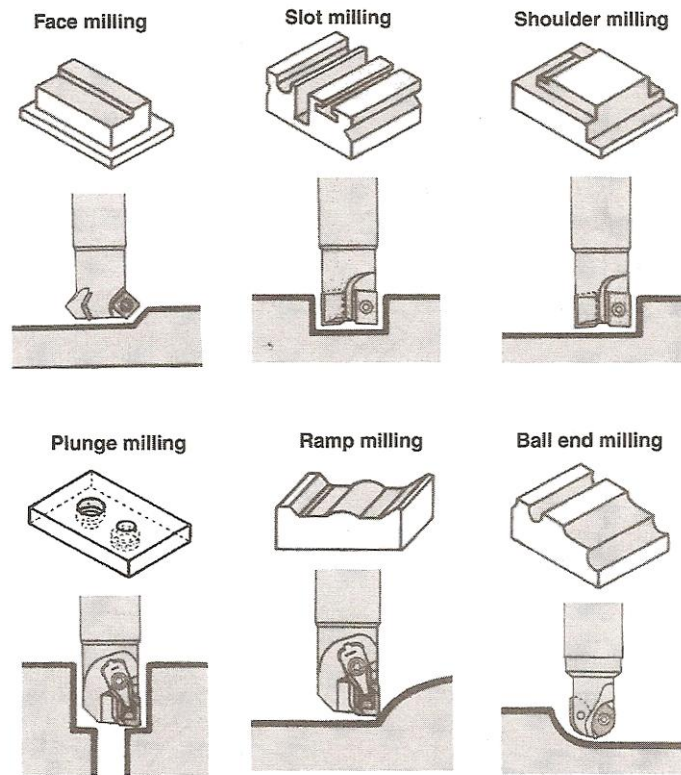
Figure 2-2: Various milling operations [33].

Glass-ceramics [34][35][36][37], multi-phase ceramics, and Ti_3SiC_2 ceramics are found to be machinable through various machinability studies that have been performed. Ceramics have been in use as artificial joints, dental prosthetics, and artificial heart valves [38]. Recently, ceramics have been widely adapted as fillers in oral cavities, since they outperform their metallic counterparts in characteristics such as biological compatibility and aesthetic appearance. Some examples include leucite reinforced porcelain, glass-infiltrated porous alumina, glass ceramics, and tetragonal zirconia polycrystals (TZP) [39]. Machinable mica based ceramics were also developed by Al-Shammery [40].

Although machining has been reported as a method of mold fabrication with anatomically-shaped surfaces or as a method of shaping trabecular bone blocks [41],

10

using multi-axis machining toolpaths to shape biomedical implants from CPP is a relatively new approach. This study is continuation of work earlier started by Wei [6] who had investigated both rapid prototyping and machining as potential approaches to shape CPP, at the University of Waterloo (www. pcl.uwaterloo.ca).

By removing residual material from a blank workpiece, milling generates the final desired shape. Using high-end universal Computer Numerical Control (CNC) milling machines, complex parts can be machined to high accuracies sufficient for many regular and non-regular manufacturing needs. To achieve high accuracy and surface finish quality, and to prevent defects such as chipping and tool breakage, the machining process requires thorough planning and choosing of machining parameters. Examples of parameters important in such operations and, specifically bone implant machining, include cutter geometry and size, tool material, tool feed rate and rotational speed, as well as a choice of coolant and chip removal method. The surface finish is mostly influenced both by the cutting forces and machining direction, which also determine chipping and tool breakage. Cutting forces also result in static and dynamic deformation of the tool and workpiece and require close attention [42]. Before implementing the machining process, the optimal machining conditions for CPP must be identified and therefore, the choice of appropriate cutting conditions, and generation of forces become very important.

All metal cutting operations have the same principles of mechanics applying to them; however, the geometry and kinematics may differ from one specific operation to another. Since milling is the specific method which is used here to machine the implant, a brief introduction to the fundamentals of cutting mechanics will be presented in chapter 3, followed by a detailed treatment of milling. Further study of other machining operations is available in literature [2][43][44].

Below is a figure showing a 2D schematic cutting of a workpiece. There are three deformation zones visible [33]. Focusing on the primary shearing zone, there are two types of assumptions associated with shearing analysis in this zone. Merchant [45] assumed that shearing happens in a thin plane in the shearing zone, while others such as

Lee and Shaffer [46] based their analysis on a thick shear deformation zone. In this thesis, the thin plane shear theory is used as is followed in Chapter 3.
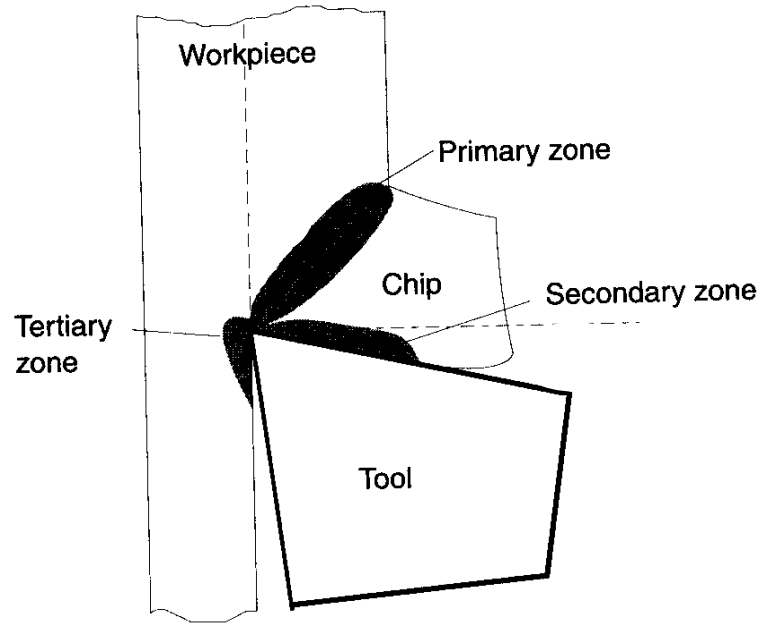
Figure 2-3: 2D schematic of cutting [33]

2.4　Summary

In this chapter, available literature on the process of implantation as a treatment option was briefly studied. A group of implant material known as calcium phosphates was presented and further review of material available on a specific group of these materials known as Calcium Polyphosphates was performed in more detail. Also, a survey of work

conducted on modeling of basic metal cutting operations as well as different milling methods was briefly presented. This study is continuation of work started earlier at University of Waterloo's Rapid Prototyping Laboratory, which is investigating machining as a potential approach to shape CPP into an implant.

Chapter 3

Optimal Cutting Conditions and a Mechanistic Model for Calcium Polyphosphate (CPP)

3.1   Introduction

Machining, grinding, and various non-mechanical chip-less processes (such as electro-discharge machining EDM) are various methods of material removal for manufacturing processes. Traditional material removal processes consist of boring, turning, reaming, drilling, milling, shaping, threading, and broaching. Abrasive processes such as grinding, lapping, ultra sonic machining, and honing are some other available manufacturing methods. Non-traditional processes include electrical and chemical means of material removal, as well as methods that involve use of abrasive jets, water jets, electron and laser beams [47].

Milling is one the most common metal removal methods used in today's manufacturing industry. As it will be explained later, universal multi-axis CNC milling machine was

used to shape the bone implant from a cubic block of CPP material. Thus, how the material reacted to this machining process was important and, consequently, machinability and optimal machining conditions for this new material were studied. Not only do the above factors need to be determined, but it should also be established whether machining and in particular milling have any negative impacts on the biomedical characteristics of CPP. In this chapter, the main focus will be on the machinability characteristics of the material. This chapter starts by looking at the impact of different spindle rotational speeds (at constant feedrate) on the surface porosity of the material from a qualitative point of view using images from a Scanning Electron Microscope and an investigation of chipping. A mechanistic model that predicts the cutting forces in the milling process was also adopted. This model was previously derived by Budak and Altintas [33] to predict the cutting forces in machining metals. The model involves cutting coefficients for CPP as a workpiece material, and considers process parameters such as the axial depth of cut, tool immersion, cutter material and geometry in predicting the machining forces. The model identification procedure was first validated by applying it to an established engineering material such as Aluminium, in order to make sure that the results and figures matched what is available in literature. Then, the same method was applied to CPP as the new material to identify the cutting coefficients. The cutting forces predicted with the model were then investigated against what was observed from experiments for the cases of flat and ball endmilling.

3.2   Optimal Cutting Conditions

Experiments were conducted to reveal the material's machining characteristics. These characteristics are either quantitative, such as the cutting coefficients' values, optimal feed rates and spindle rotational speeds, and optimal tool size, or qualitative, involving the prevention of CPP chipping, breakage, and loss of surface porosity. In this section,

15

some important machining characteristics that are useful in the planning of this machining process are noted.

3.2.1   Tool size

It has been observed that smaller tool sizes, which have lower diameter and therefore lower peripheral tooth speeds at the same spindle rotational speed, inflict less chipping and CPP breakage during the cutting operation. Therefore, from the author's experience, it was recommended that the tool diameter be below 4mm and preferably around 2mm to prevent chipping. To increase material removal rate and thus increase productivity, it is recommended to have full immersion cuts wherever possible. Full immersion means that the all the tool diameter is engaged in cutting and removing material.

3.2.2   Surface Porosity before and after Machining

As stated in the previous section, it was necessary to determine whether the machining process altered the surface porosity on the finished surface. In order to investigate this, a Scanning Electron Microscope (SEM) was used to image the top surface of a machined cylinder from CPP before and after machining. This qualitatively measured if the surface porosity had been altered in any way. The cylinders were 4mm in diameter and 6mm in length and were to be machined with the following machining parameters. Cutting speed is defined as the tangential speed at the tip of the tool's tooth.

Table 3-1: Machining parameters for surface porosity investigation

Spindle Speed: 2000rev/min	*Tool:* Refer to Table 3-2	*Feed rate:* 50mm/min
Depth of cut: 1mm	*Coolant:* Air blast	*Type:* Conventional (up-Milling)
Tool step-over: 3/64" (1.19mm)	*Cutting Speed*: 312mm/sec	*Number of Passes:* 5

Table 3-2: Description of tool used for surface porosity investigation for section 3.2.2 [48]

2 Flute Reg. Length Carbide Endmill - Inch				
Cutting Diameter	Shank Diameter	Flute Length	Overall Length	Sowa Code No.
3/32" (2.38mm)	1/8" (3.17mm)	5/16" (7.9mm)	1-1/2" (38.1mm)	103-849

As stated above, the CPP cylinders are quite small, having only 4mm in diameter and 6mm in length. At the same time, the brittle and relatively weak nature of CPP makes clamping such a small and fragile part a challenge. It was proposed that an aluminium rod be machined to have two flat surfaces. Then, a hole, 4mm in diameter and 4mm in length was drilled on the top part, with three set screws inserted to three sides to support a snug clamping of the cylinder. This way, the force applied from the vice's jaws would not be transferred directly to the small fragile cylinders, and the setscrews hold the cylinders in place with the right amount of force. The setscrews were also chosen to have Teflon heads to prevent local stresses on the cylinders and prevent fracture during the tightening stage. The cylinders themselves were wrapped in a few layers of Teflon to provide dampening and prevent local stresses from the aluminium body of the hole.

Displayed below is a picture showing the clamp (Figure 3-1):
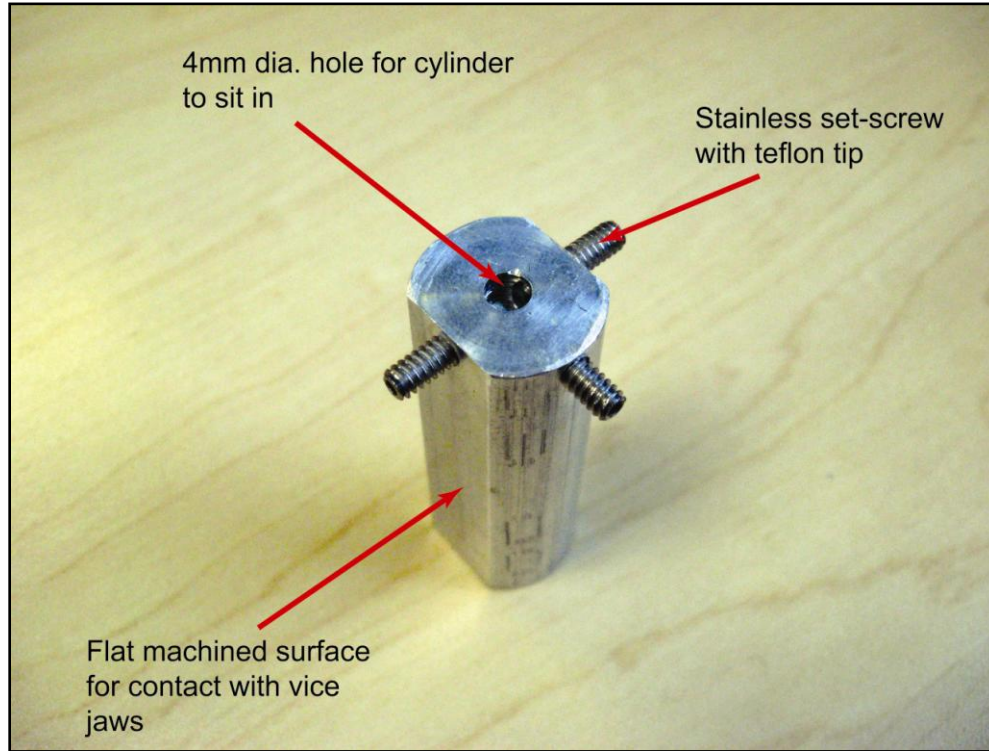
Figure 3-1: Aluminium clamp for small cylinder machining

Before using a Scanning Electron Microscope (SEM) to investigate the surfaces of the original and machined cylinders, an ultrasonic cleaner was used to remove any dirt or impurities from the surfaces of the cylinder. A Branson 5210 ultra sonic cleaner (Branson Co., Danbury, CT, USA) was used and cylinders were submerged in pure grade ethanol for 15 minutes while changing the solution each 15 minutes for a total of three times. This process was done for both the machined and original cylinders (received from University of Toronto), and then the cylinders were left to be dried in room temperature.

Samples were coated with a 10µm layer of Gold to prevent charging. Then, the samples were put in the JSM-6460 SEM machine (Jeol Ltd., Akishima, Tokyo) and the results were as follows. Starting from a low magnification of 20X, an SEM image of the

original cylinder was investigated from a qualitative point of view. The image is shown below in Figure 3-2.
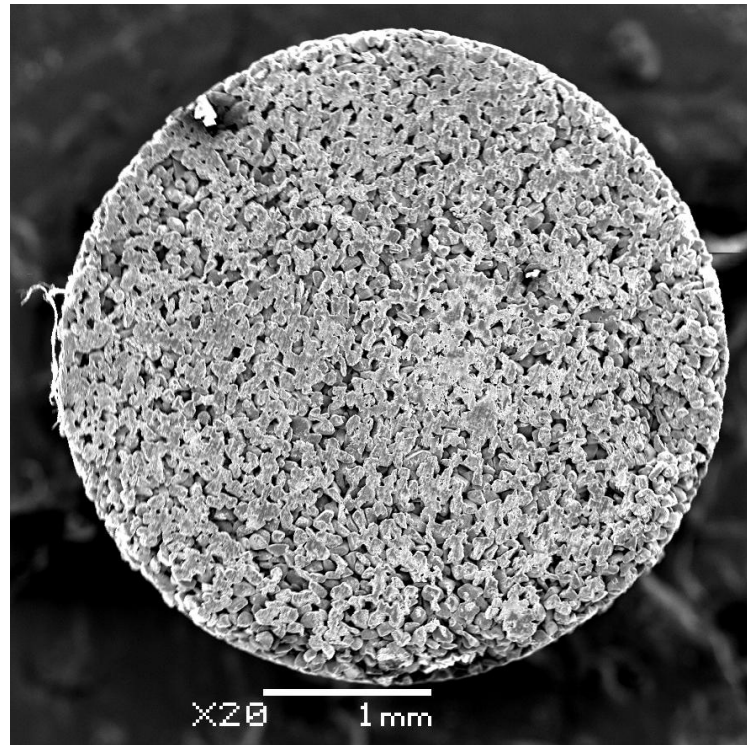
Figure 3-2: SEM image of cylinder's original top surface.

Note that some smearing is visible and that can be related to the preparation process of the cylinders, in which a long cylindrical CPP rod is cut in to smaller pieces using a knife. The blade can smear the surface of the cylinder and reduce surface porosity, yet the amount of porosity visible in Figure 3-2 is satisfactory for cartilage growth.

After machining the top surface of the cylinder using the machining process described in Table 3-1, using the tool described in Table 3-2, the sample cylinder was cleaned using the ultra-sonic cleaning method described earlier and another SEM image was captured from the top surface of the cylinder to be compared with Figure 3-2. Figure 3-3 shown

below is the captured SEM image of the machined surface with the same magnification level.
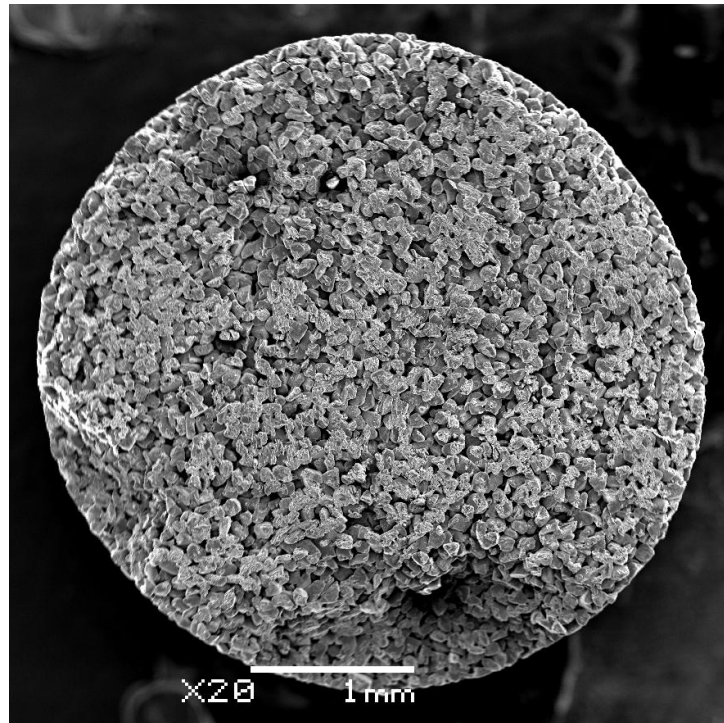
Figure 3-3: SEM image of cylinder's machined top surface.

Looking at surface porosity of the machined cylinder, if not better than before machining, it is definitely comparable to the original surface. Surface porosity exists throughout the surface of the cylinder and it is expected for the cartilage growth to be similar or better on the machined surface when compared with the original surface. Later in this section, higher magnifications will also be examined, but there is more to be noted on this lower magnification. Focusing on the lower part of the cylinder after machining, there is a small chunk that has been chipped off from the edge of the cylinder. Now, to examine the surface of the implant more closely, the magnification scale is increased to 50X, as shown in Figure 3-4. As it can be observed, the machined surface is more porous and does not show any evidence of smearing or cavity blockage. In the following Figure

3-5 to Figure 3-7, the magnifications is increased even more to levels of 100X, 200X, and a very high magnification of 1000X. In all instances, the surface porosity and cavity openings are better in the machined surface from a qualitative point of view when compared with the original surface. Note that at a very high magnification level of 1000X, not much difference is observed between the machined and original surfaces.
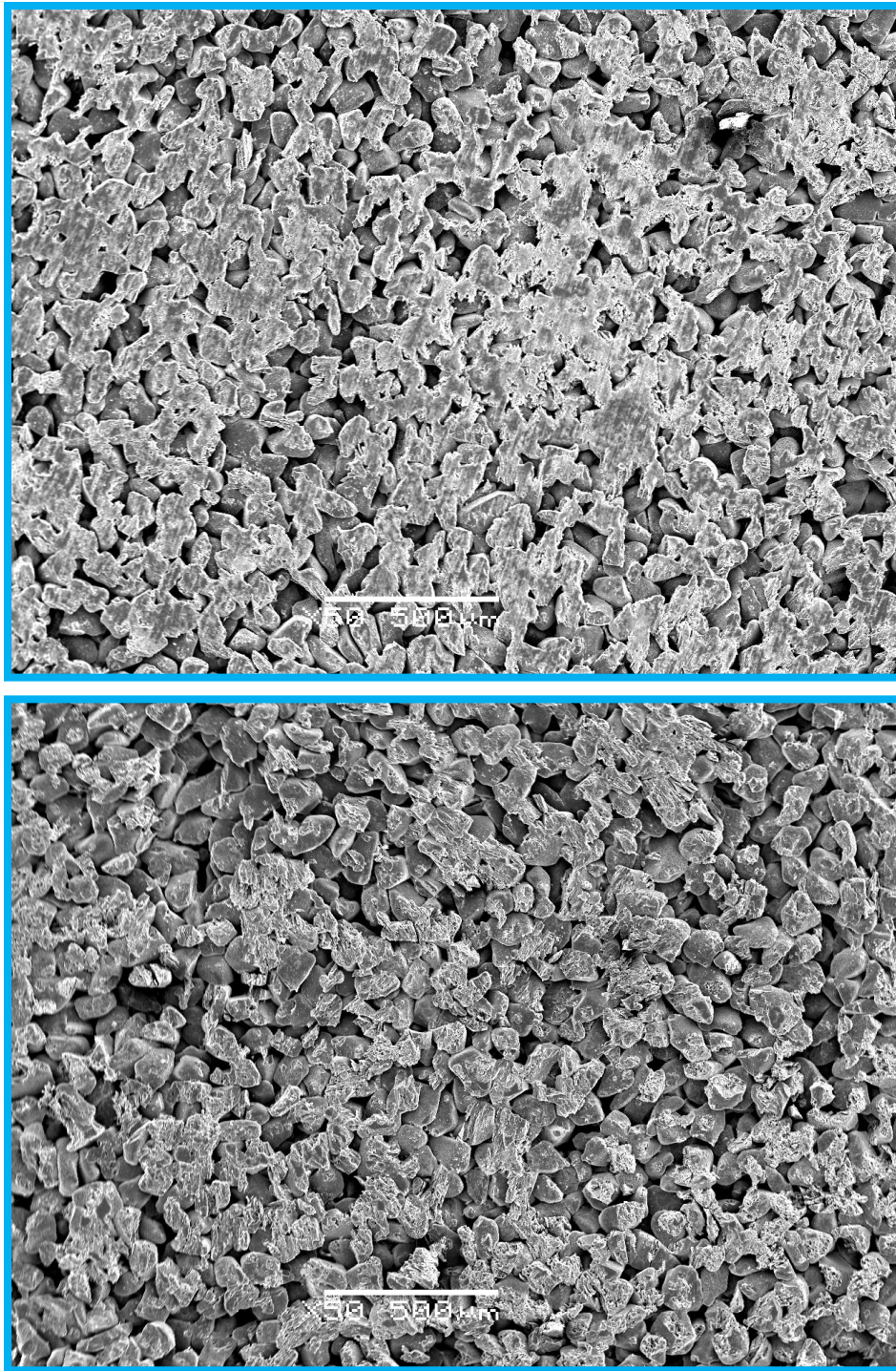
Figure 3-4: Comparing SEM images of original CPP surface (top) with machined surface (bottom) at 50X magnification level.

22
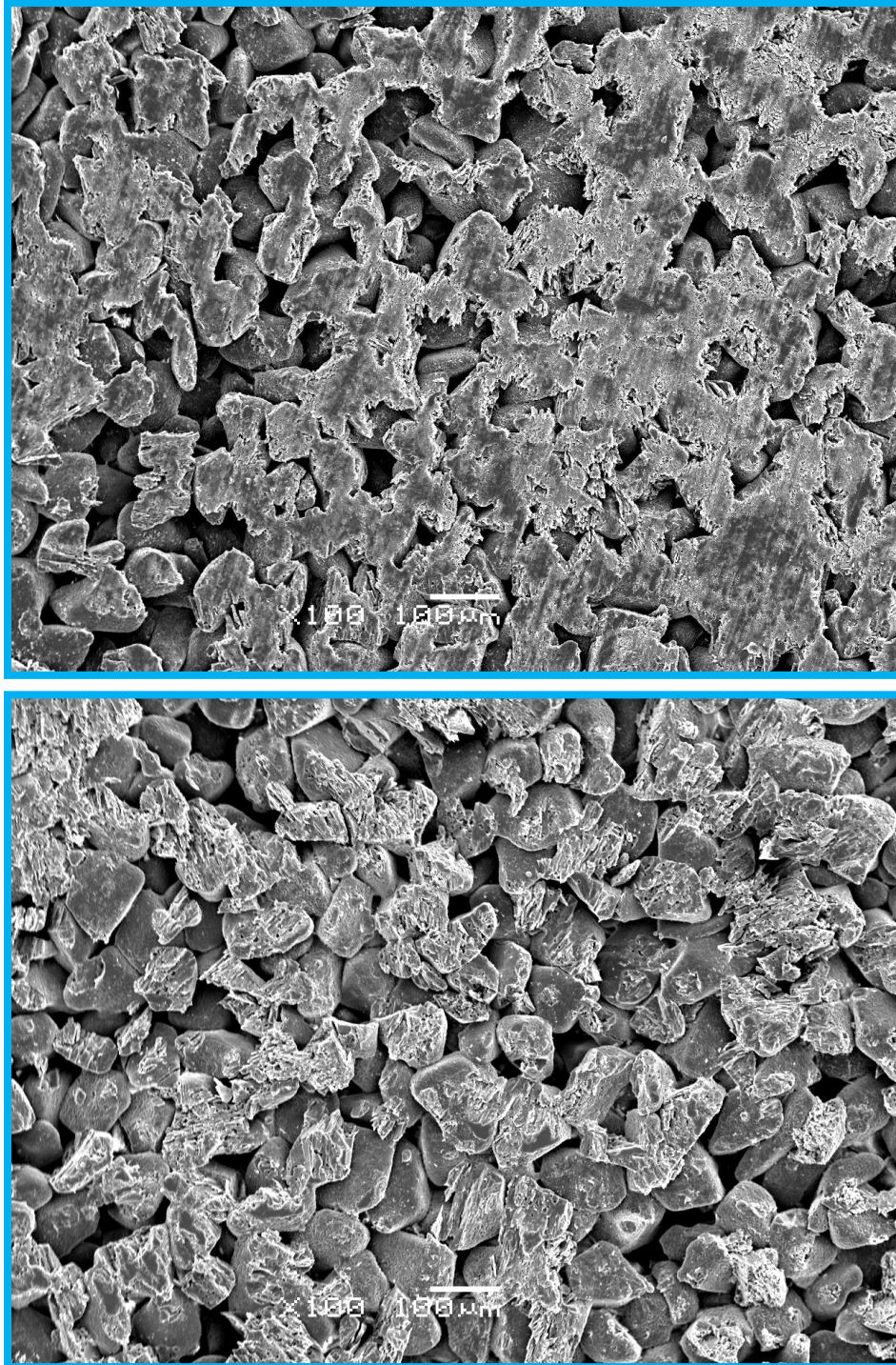
Figure 3-5: Comparing SEM images of original CPP surface (top) with machined surface (bottom) at 100X magnification level.
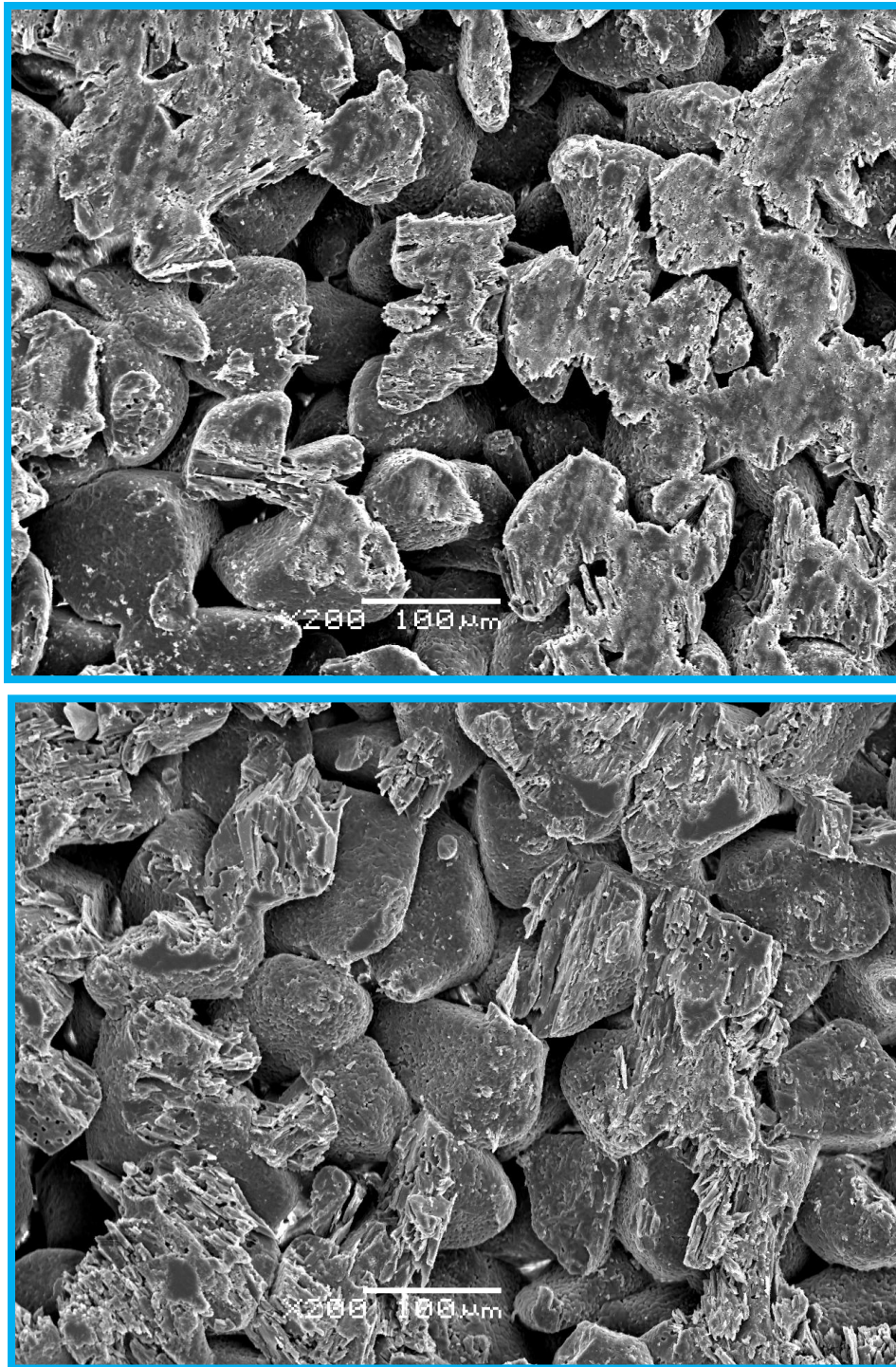
Figure 3-6: Comparing SEM images of original CPP surface (top) with machined surface (bottom) at 200X magnification level.
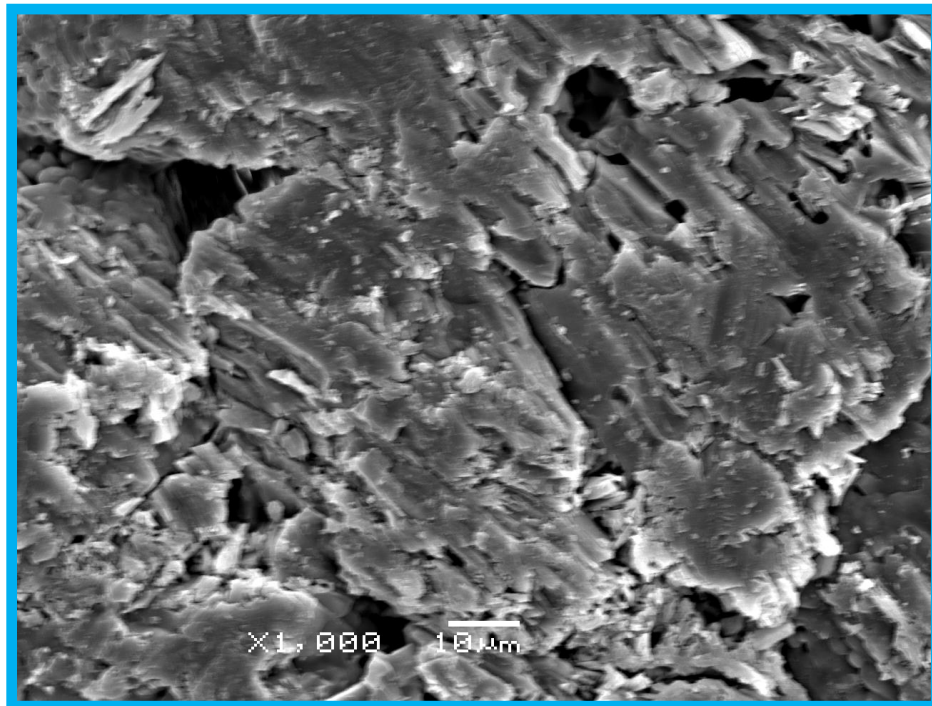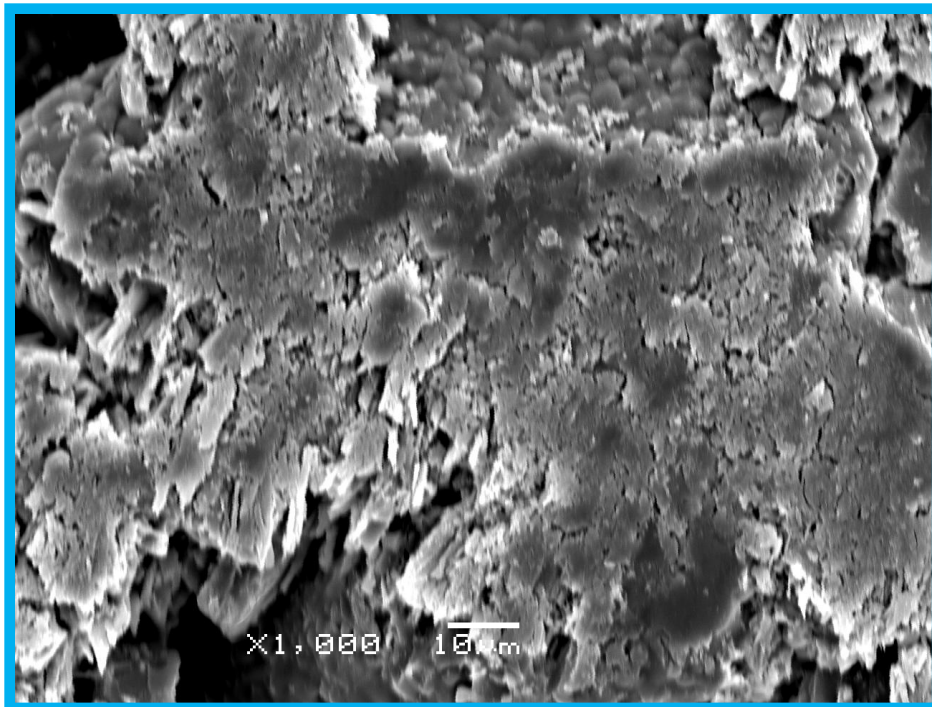
Figure 3-7: Comparing SEM images of original CPP surface (top) with machined surface (bottom) at 1000X magnification level.

3.2.3   Chipping

Chipping usually occurs where the material is weakest and the forces are the highest. This means that should there be material defects such as cracks and cavities, then it is possible that, due to the brittle nature of CPP, a chunk of the material may break off and chipping may occur. Chipping is usually small in size and happens at the corners or edges of the block, since these areas are the weakest. A chipped corner or edge represents a deviation from the desired implant geometry; hence necessary precautions must be taken in order to avoid this undesirable phenomenon.

Prevention of chipping can be accomplished by lowering the tool size, which in the author's experience, has a great impact on chipping. Also, reducing the spindle rotational speed and feed rate is helpful. How the material was sintered and prevention of defects such as cracks and incomplete sintering processes in certain areas will definitely benefit the machining process and prevent cracking and chipping and could possibly lead to higher feed rates and thus, higher productivity. However, reducing the tool size, feed, and speed result in a compromise in the productivity of the machining process. The optimal range of cutting speed was found to be from 50 to 150mm/min and 1500 to 2500rev/min, up-milling and a depth of cuts of a maximum of 3mm using the tool described in Table 3-2. This translates into a tangential cutting speed of around 100 to 350mm/sec at the specified feed rates. Using these conditions, a set of cutting experiments were performed and edges were checked against chipping. The results were satisfactory. SEM images relating to these tests are followed:
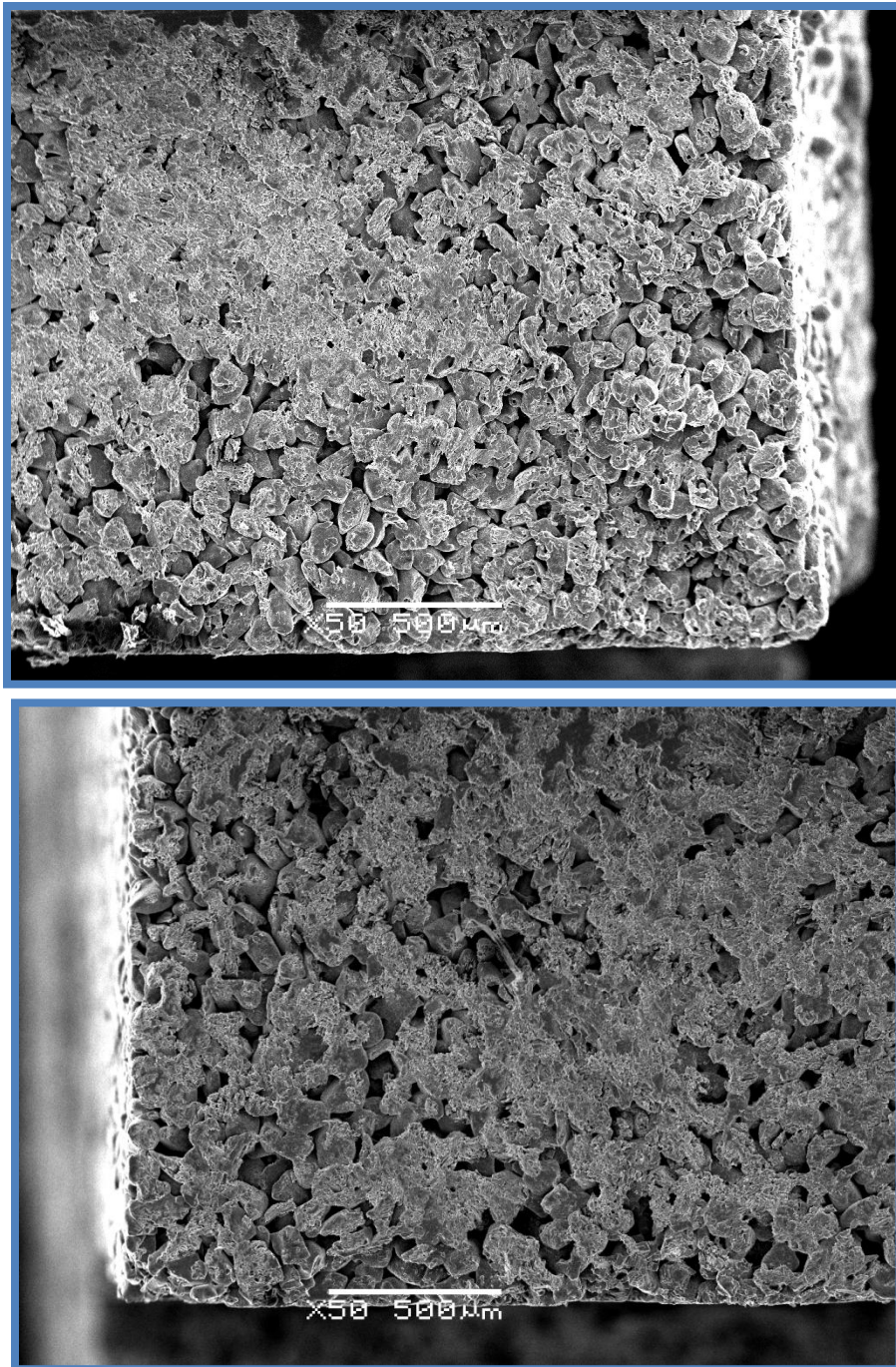
Figure 3-8: SEM images of the surface of a machined CPP, using the tool described in Table 3-2, with 1500rev/min spindle rotational speed and 50mm/min feed rate.
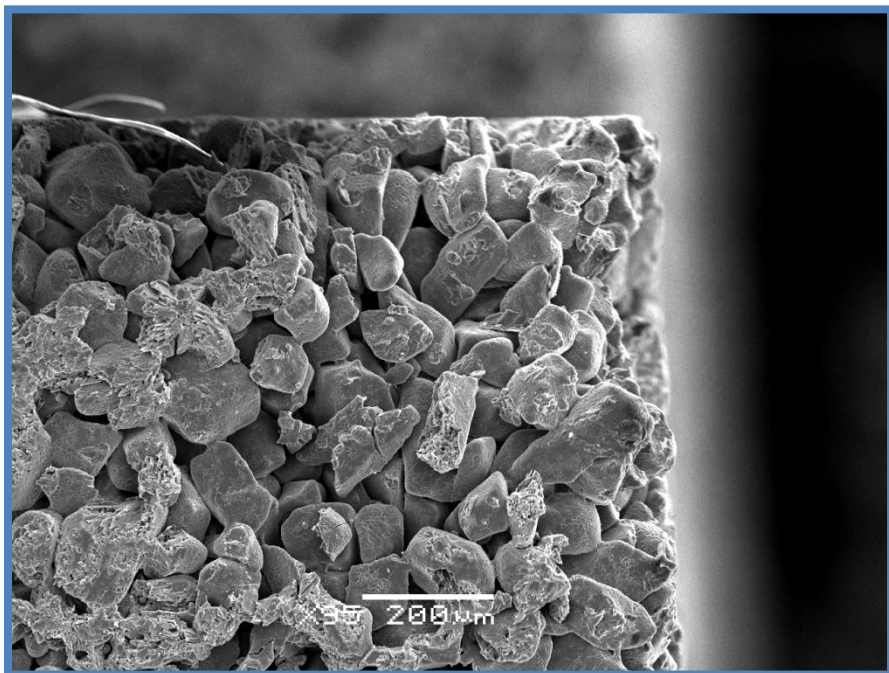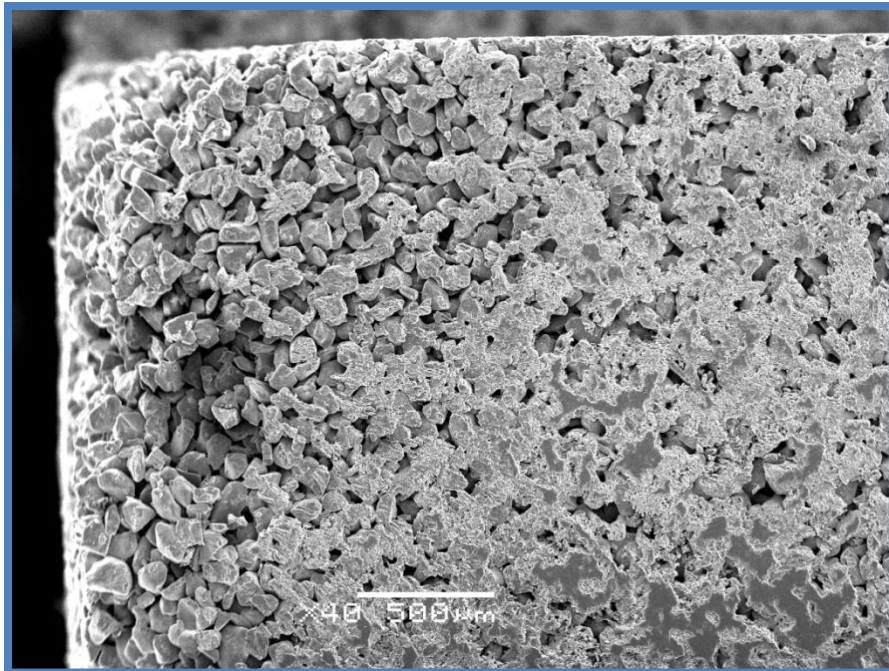
Figure 3-9: SEM images of the corner edges of a machined CPP surface, using the tool described in Table 3-2, with 2500rev/min spindle rotational speed and 50mm/min feed rate. Note that edges are acceptable, but some chipping is visible.

The 2500rev/min spindle speed is where chipping starts to appear (315mm/sec cutting speed for tool in Table 3-2, with 50mm/min feedrate). It is suggested to keep the rotational speed below this value. Also, any feeds above 0.750mm/tooth is not recommended due to excessive forces and possibility of chipping and breakage of CPP.

3.2.4　Very High Rotational Speeds and Glossiness

Using the 3/32" diameter flat endmill shown in Table 3-2, a set of experiments were conducted on a CPP block and straight cuts of 1mm depth of cut and half-immersion were performed at a very high tool rotational speed of 12000rev/min and a feed of 50mm/min to investigate how CPP would react to such high cutting speeds. Aside from frequent destructive chipping, the material showed an interesting behaviour of glossiness in which the surface porosity was lost and the material was covered by a rather smooth clear glossy surface. Although it is not yet known exactly why this occurred, it is believed that heat generated from this high speed machining process has contributed to the melting of CPP particles, and the tool's movement has pushed down this melted material into the porous surface. Subsequent cooling of the material has generated the glossy surface finish. Figure 3-10 is an SEM image of this blocked CPP surface:
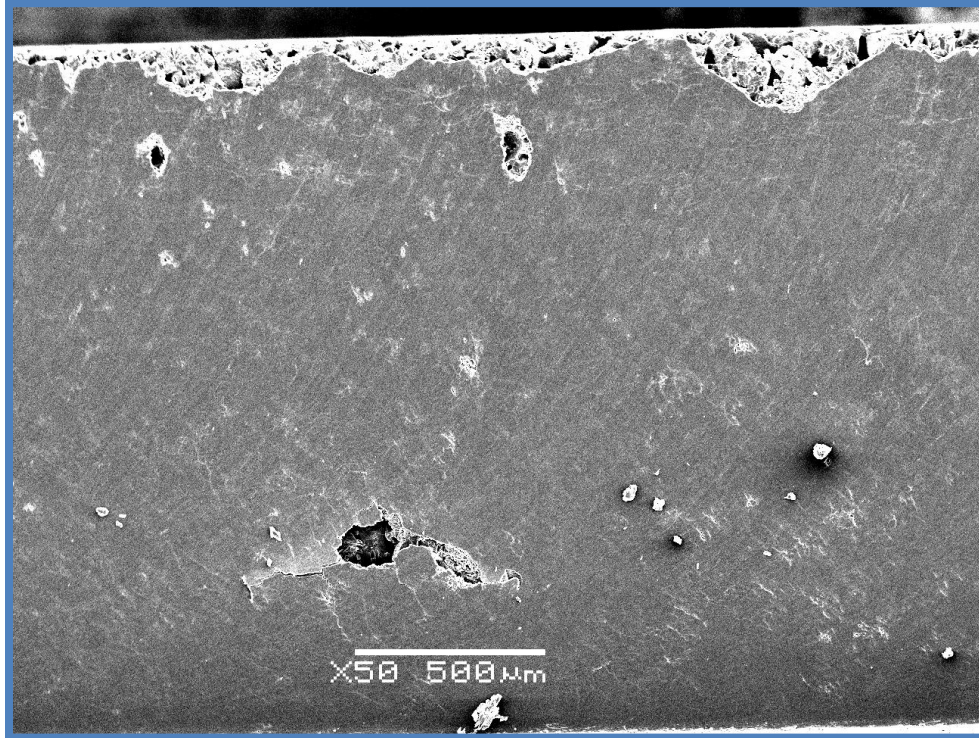
Figure 3-10: 12000rev/min, 50mm/min up-milling CPP surface finish image, showing absolute loss of surface porosity and very bad chipping at the edge along the cut. The tool cuts are also visible on the surface.

Such high speeds are not to be used during CPP machining operations due to loss of surface porosity and extreme chipping, which would make the CPP implant unusable for its biomedical purpose.

3.3   Milling Cutting Mechanics

There are many different milling operations conducted with different mills such as face milling, slot milling, shoulder milling, plunge milling, ramp milling and ball endmilling. All milling operations plus some other cutting operations such as turning and drilling can all be modeled using orthogonal or oblique cutting mechanics. With most common

cutting operations being three-dimensional, a simple case of two dimensional cutting operation will be introduced here. Figure 3-11 depicts the process of material removed by a cutting edge in an orthogonal manner in which the cutting edge is perpendicular to the direction of relative tool-workpiece motion.
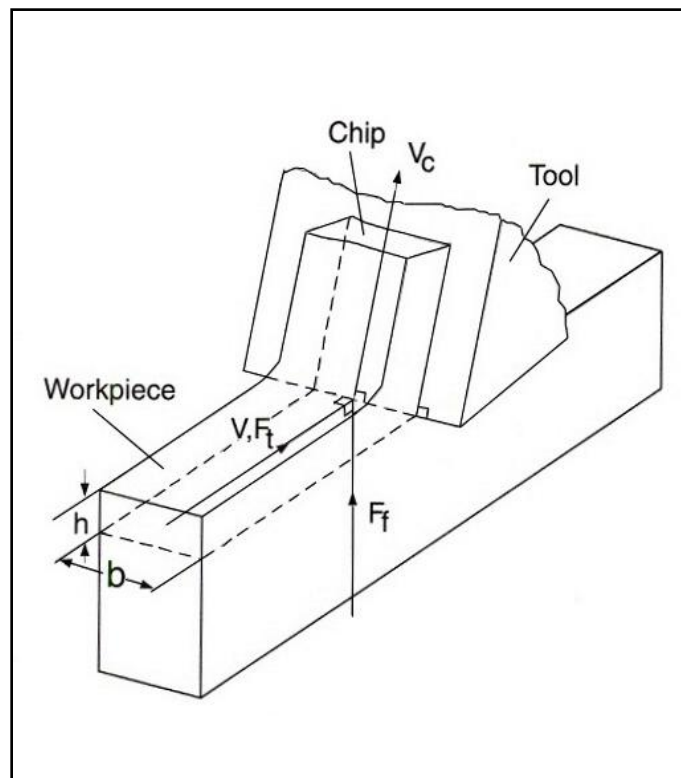
Figure 3-11: Orthogonal cutting [33].

The cutting forces are exerted in the direction of velocity and uncut chip thickness, which are called tangential (F_t) and feed forces (F_f). However, should the cutting process be oblique rather than orthogonal, a third force component resulting from the inclination angle (i) exists which acts in the radial direction (F_r), as shown in Figure 3-12.
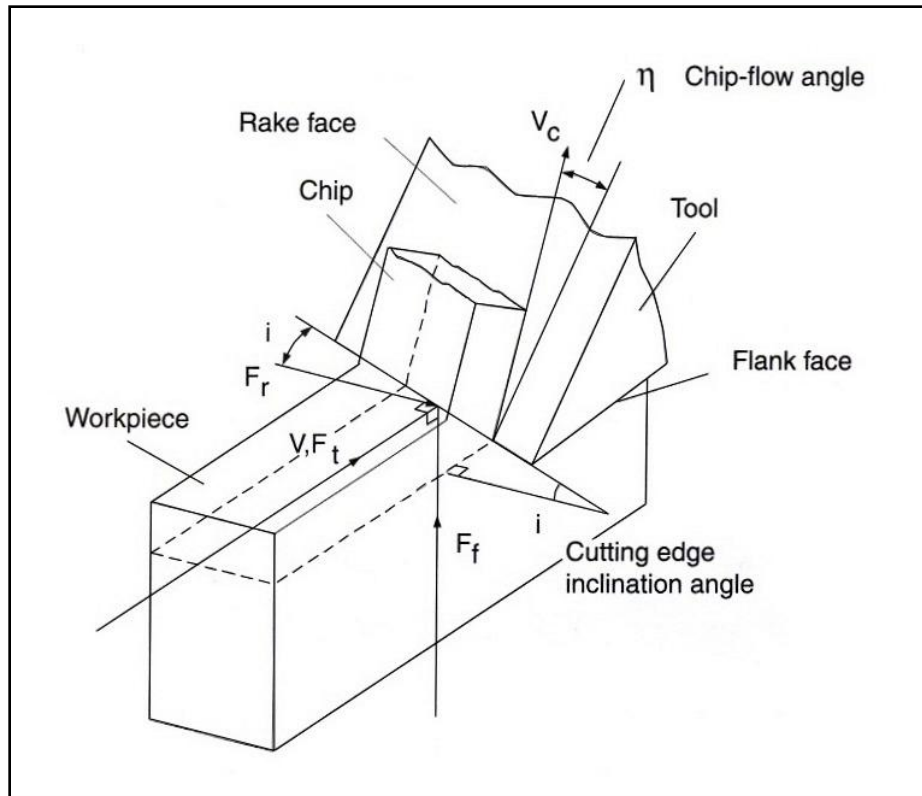
Figure 3-12: Oblique cutting [33].

The added complexity from the oblique cutting model usually results in a different approach, which involves use of kinematics and geometrical transformation of the orthogonal cutting model to reach a general cutting model [49]. The mechanistic cutting model is more practical compared to other more analytical or computational approaches. This method, first introduced by Kline and DeVor [50][51] and then further refined by Feng and Su for ball endmilling operations [52], uses a linear cutting force model that has only the cutting coefficients as the unknowns, represented by Budak [49] as shown later in Equation (3.2).

3.4 Identifying the Milling Force Coefficients for CPP

In this section the theoretical background of the cutting force prediction model is explained. Focus will be mainly on milling as a cutting process, since this was the main machining method used for the manufacturing and shaping of the implant. The milling operation is a periodic cutting process in which the cutting edge engages with the material through the rotational movement of the tool in the machine's spindle and simultaneous feed of the workpiece into this tool. During this process, depending on the tool geometry, the number of teeth on the cutter and the pitch angles, material is removed from the workpiece in a non-uniform yet periodic manner. The periodic nature of this cutting method raises concern on the vibration of the cutter machine and the workpiece, and the possibility of resonance and chatter during cutting. To model the force generation mechanism, the kinematics and dynamics of how the tool and workpiece interact are derived for one tool rotation period. The same dynamics can be used in every other period since this is a periodic operation. Figure 3-13 presents a schematic view of the milling process with some geometric labelling for mathematical derivation purposes.
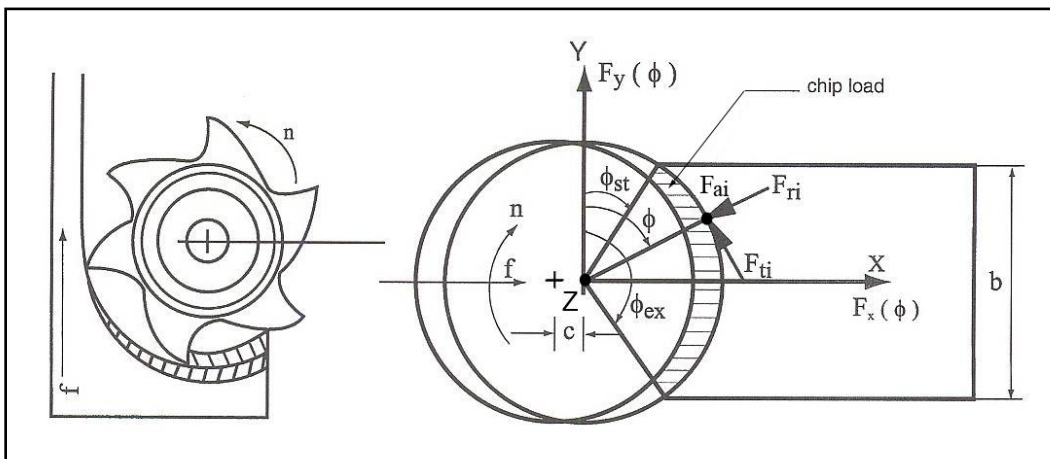
Figure 3-13: Schematic of a milling tool engaged in cutting (left) with labelling of important geometrical parameters (right) [33].

33

The instantaneous chip load or in other words, chip thickness h, can be approximately modeled as a sinusoidal function of the instantaneous immersion as shown below:

$$h\ (\emptyset) = \ c\sin(\emptyset) \tag{3.1}$$

Above, c is the feed per cutting tooth in units of [mm/rev-tooth] and $\emptyset$ is the instantaneous angular immersion of this cutting tooth in degrees. Note that depending on the number of teeth on the cutter, there could be more than one tooth engaged in cutting at every instant. Also, note that Figure 3-13 is only a 2D representation of the milling process, and depending on the helix angle and the shape of the milling cutter, there might be different tooth engagements and therefore different chip loads in different depths.

There are three major forces acting on the cutter, and therefore the workpiece, being the Tangential force ($F_t(\emptyset)$), Radial force ($F_r(\phi)$), and the axial force ($F_a(\phi)$) in which they are expressed as a function of ϕ. These forces can be calculated by a linear function that includes the effects of the uncut chip area ($ah(\phi)$) and the edge contact length (a) as:

$$\left.\begin{aligned}
F_t(\phi) &= K_{tc}ah(\phi) + \ K_{te}a, \\
F_r(\phi) &= K_{rc}ah(\phi) + \ K_{re}a, \\
F_a(\phi) &= K_{ac}ah(\phi) + \ K_{ae}a,
\end{aligned}\right\} \tag{3.2}$$

Above, K_{tc}, K_{rc},and K_{ac} are the cutting force coefficients that are constant values and are contributed by the shearing effect of the tangential, radial, and axial directions, respectively. The K_{te}, K_{re}, and K_{ae} values are also constant and are the contribution of the edge forces. The later three constants are also known as edge constants. The cutting force coefficients are either evaluated mechanically from milling tests or using the classical orthogonal to oblique cutting transformation. They also may be sometimes expressed as a nonlinear function of the instantaneous or mean chip load h_a [33], which can be calculated as:

$$h_a = \frac{\int_{\phi_{st}}^{\phi_{ex}} c \sin(\phi)\, d\phi}{\phi_{ex} - \phi_{st}} = -c \frac{\cos \phi_{ex} - \cos \phi_{st}}{\phi_{ex} - \phi_{st}} \qquad (3.3)$$

Naming D as the milling cutter diameter, then the torque on the spindle T_c will be calculated as:

$$T_c = F_t \cdot \frac{D}{2} \qquad (3.4)$$

Horizontal (i.e., feed or in the x axis), normal (i.e., y axis), and axial (i.e., z axis) components of the forces acting on the tool are derived from the equilibrium of the forces acting on the cutter and workpiece as shown in Figure 3-13:

$$
\begin{aligned}
F_x(\phi) &= -F_t \cos(\phi) - F_r \sin(\phi) \\
F_y(\phi) &= +F_t \sin(\phi) - F_r \cos(\phi) \\
F_z(\phi) &= +F_a
\end{aligned}
\qquad (3.5)
$$

However, looking at Equation (3.5), it is noted that these forces are only available when the tooth is in contact with the workpiece, that is:

$$F_x(\phi), F_y(\phi), F_z(\phi) \neq 0 \qquad when\ \phi_{st} \leq \phi \leq \phi_{ex} \qquad (3.6)$$

in which ϕ_{st} and ϕ_{ex} are the entry and exit angles of the tooth, as shown in Figure 3-13. One other important note is that in cutters with many teeth, there may be multiple teeth engaged in cutting simultaneously, which in that case the resulting forces from each tooth must be taken into consideration and then the resulting sum of these forces has to be calculated as shown below in Equation (3.7).

$$F_x = \sum_{j=1}^{N} F_{xj}(\phi_j)$$

$$F_y = \sum_{j=1}^{N} F_{yj}(\phi_j) \tag{3.7}$$

$$F_z = \sum_{j=1}^{N} F_{zj}(\phi_j)$$

Above, j represents each cutter tooth and the resulting force will either be calculated for x, y, and z directions using Equation (3.5) if the tooth is engaged in cutting, or a value of zero is substituted when a particular tooth is not engaged in milling.

With the above introduction to the mechanics of milling, the above two dimensional model can be superimposed to a three dimensional representation of the cutting forces acting on a mill by repeating the above procedure for a finite number of heights for the depth of cut a, in which there are no other cutting forces afterwards (Figure 3-14).
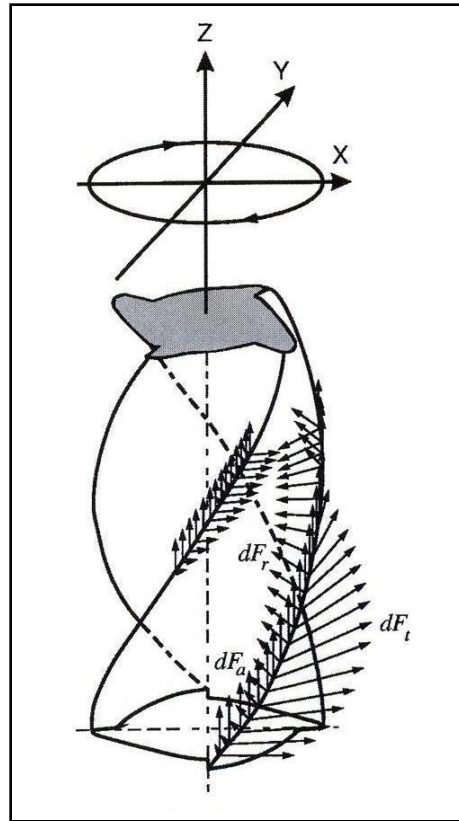
Figure 3-14: Three dimensional endmilling representation with a finite number of sections showing the incremental calculated forces in each section [33].

This is a computational process, and can be programmed in software to predict the forces at each immersion angle ϕ and at each height z of the tool, and then to generate a plot of the resulting forces in the x, y and z axis directions [33]. This model can be used both in simulating the cutting forces, as well as in identifying the cutting force coefficients ($K_{tc}, K_{rc}, K_{ac}, K_{te}, K_{re}, K_{ae}$) from experimental machining data.

To simulate the cutting forces, either available commercial software such as CutPro®(7.0, Manufacturing Automation Laboratories Inc., Vancouver, BC, Canada) can be used, or a program can be written to generate the final results. In this thesis, the cutting coefficients have been identified manually using Microsoft Excel and flat endmilling forces have been predicted using CutPro®. Ball endmilling forces, which require more elaborate computations, have been predicted using CutPro® as well.

37

Modelling the cutting forces using an analytical approach, rather than a numerical one, will result in shorter calculation times and elimination of numerical errors resulting from numerical integration. When the kinematics of the milling process is taken into account, it is feasible to derive semi-analytical terms for the endmilling process [53]. Assuming that the endmill has a helix angle of β, diameter of D, N teeth, and a constant axial depth of cut equal to a, and that the immersion is calculated clockwise from the normal y direction, then the elemental forces acting on the cutter teeth can be divided into tangential $(dF_{t,j})$, radial $(dF_{r,j})$, and axial $(dF_{a,j})$ components that change at each moment with respect to the elemental height dz (Figure 3-14). Therefore, they can be expressed as functions of ϕ and height z as follows:

$$
\begin{aligned}
dF_{t,j}(\phi, z) &= \left[K_{tc} h_j\left(\phi_j(z)\right) + K_{te} \right] dz \\
dF_{r,j}(\phi, z) &= \left[K_{rc} h_j\left(\phi_j(z)\right) + K_{re} \right] dz \\
dF_{a,j}(\phi, z) &= \left[K_{ac} h_j\left(\phi_j(z)\right) + K_{ae} \right] dz
\end{aligned}
\tag{3.8}
$$

Above, the chip thickness is specified as:

$$
h_j(\phi, z) = c \sin \phi_j(z)
\tag{3.9}
$$

The same way it was shown in Equation (3.5), the tangential, radial, and axial components are resolved to feed(x), normal(y), and axial(z) directions using the following trigonometric transformations (i.e. projection):

$$dF_{x,j}\left(\phi_j(z)\right) = -dF_{t,j}\cos\phi_j(z) - dF_{r,j}\sin\phi_j(z)$$

$$dF_{y,j}\left(\phi_j(z)\right) = +dF_{t,j}\sin\phi_j(z) - dF_{r,j}\cos\phi_j(z) \qquad (3.10)$$

$$dF_{z,j}\left(\phi_j(z)\right) = +dF_{a,j}$$

By substituting Equations (3.8) and (3.9) into Equation (3.10), the resulting differential force equations are found to be:

$$dF_{x,j}\left(\phi_j(z)\right) = \left\{\frac{c}{2}\left[-K_{tc}\sin 2\phi_j(z) - K_{rc}\left(1 - \cos 2\phi_j(z)\right)\right]\right.$$
$$\left. + \left[-K_{te}\cos\phi_j(z) - K_{re}\sin\phi_j(z)\right]\right\}dz$$

$$dF_{y,j}\left(\phi_j(z)\right) = \left\{\frac{c}{2}\left[K_{tc}\left(1 - \cos 2\phi_j(z)\right) - K_{rc}\sin 2\phi_j(z)\right]\right. \qquad (3.11)$$
$$\left. + \left[K_{te}\sin\phi_j(z) - K_{re}\cos\phi_j(z)\right]\right\}dz$$

$$dF_{z,j}\left(\phi_j(z)\right) = \left[K_{ac}c\sin\phi_j(z) + K_{ae}\right]dz$$

The above differential equations can be analytically integrated along the in-cut portion of the flute j in order to obtain the summed cutting forces acting on the tool and the workpiece.

$$F_x\big(\phi(z)\big) = \int_{z_{j,1}}^{z_{j,2}} dF_x\left(\phi_j(z)\right)dz$$

$$F_y\big(\phi(z)\big) = \int_{z_{j,1}}^{z_{j,2}} dF_y\left(\phi_j(z)\right)dz \qquad (3.12)$$

$$F_z\big(\phi(z)\big) = \int_{z_{j,1}}^{z_{j,2}} dF_z\left(\phi_j(z)\right)dz$$

In which $z_{j,1}\left(\phi_j(z)\right)$ and $z_{j,2}\left(\phi_j(z)\right)$ are the lower and upper limits on the axial engagement limits in the cutting portion of the flute j. Assuming that the bottom end of one of the cutter teeth is considered to be the immersion angle ϕ, the remaining flutes are angled as $\phi_j(0) = \phi + j\phi_p$, with $j = 0, 1, 2 \dots (N-1)$. Therefore, at an axial depth of cut z the lag angle can be modeled as $\psi = k_\beta z$, where $k_\beta = \left(\frac{2\tan\beta}{D}\right)$. Thus the immersion angle for flute j at depth of cut of z is as shown in Equation (3.13). Also, Figure 3-15 shows the values β and ϕ_p on the tool teeth.
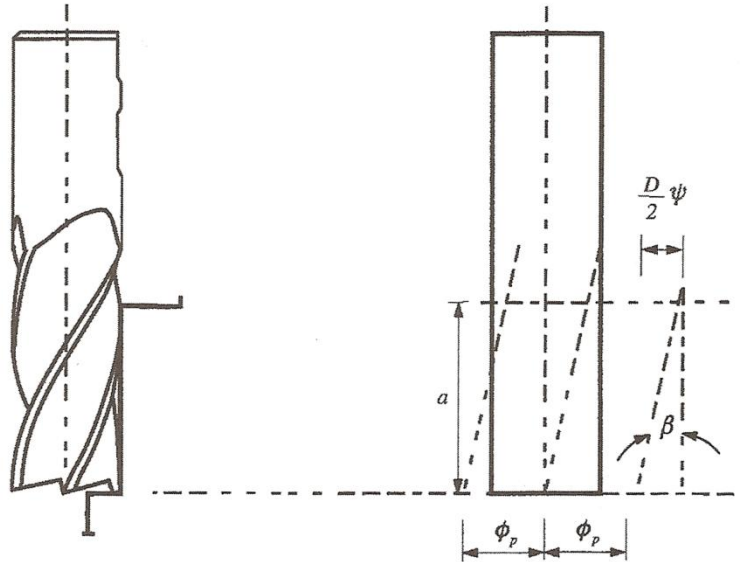
Figure 3-15: Cutter geometry variable definitions [33]

$$\phi_j(z) = \phi + j\phi_p - k_\beta z \tag{3.13}$$

Now, by carrying out the integrations in Equation (3.12), the following will result:

$$F_{x,j}\left(\boldsymbol{\phi}_j(\boldsymbol{z})\right) = \left\{\frac{c}{4k_\beta}\left[-K_{tc}\cos 2\phi_j(z)\right.\right.$$

$$+ K_{rc}\left[2\phi_j(z) - \sin 2\phi_j(z)\right]\right]$$

$$\left.+ \frac{1}{k_\beta}\left[K_{te}\sin\phi_j(z) - K_{re}\cos\phi_j(z)\right]\right\}_{z_{j,1}\left(\phi_j(z)\right)}^{z_{j,2}\left(\phi_j(z)\right)}$$

$$F_{y,j}\left(\boldsymbol{\phi}_j(\boldsymbol{z})\right) = \left\{\frac{-c}{4k_\beta}\left[+K_{tc}\left(2\phi_j(z) - \sin 2\phi_j(z)\right)\right.\right.$$

$$+ K_{rc}\cos 2\phi_j(z)\right]$$

$$\left.+ \frac{1}{k_\beta}\left[K_{te}\cos\phi_j(z) + K_{re}\sin\phi_j(z)\right]\right\}_{z_{j,1}\left(\phi_j(z)\right)}^{z_{j,2}\left(\phi_j(z)\right)}$$

$$F_{z,j}\left(\boldsymbol{\phi}_j(\boldsymbol{z})\right) = \frac{1}{k_\beta}\left[K_{ac}c\cos\phi_j(z) - K_{ae}\phi_j(z)\right]_{z_{j,1}\left(\phi_j(z)\right)}^{z_{j,2}\left(\phi_j(z)\right)}$$

(3.14)

The cutting forces are then calculated by summing up all the contributing forces from all teeth to derive the instantaneous forces on the cutter at immersion ϕ:

$$F_x(\phi) = \sum_{j=0}^{N-1} F_{x_j}$$

$$F_y(\phi) = \sum_{j=0}^{N-1} F_{y_j}$$

(3.15)

$$F_z(\phi) = \sum_{j=0}^{N-1} F_{z_j}$$

And the resultant total force acting on the tool at any instant can be calculated as:

$$F(\phi) = \sqrt{F_x(\phi)^2 + F_y(\phi)^2 + F_z(\phi)^2} \qquad\qquad (3.16)$$

The above semi-analytical expressions can be programmed in software and executed, as it was done for the numerical method presented before. The above method is used in some CAM packages that predict and simulate cutting forces and other phenomena that are linked to cutting forces such as chatter vibration and surface finish. More information can be found in related literature [33][54].

3.5   Mechanistic Modeling of Cutting Forces

In this section, the mathematical background of mechanistic modeling will be introduced, and then this method will be used in identifying the cutting force coefficients for CPP. This will be achieved by capturing experimental forces using a dynamometer to identify the coefficients, and comparing experimental and simulated forces in order to validate the mechanistic model under various machining conditions.

The cutting coefficients for a specific material will need to be determined to enable the use of force prediction equations. One way of determining these coefficients would be to have multiple cutting tests for every different scenario and then evaluate the coefficients for each particular case, and substitute their values in the equations. However, there are a variety of milling tools with different geometries available in the market, and if these tests are to be conducted for each specific case, then many time consuming tests would need to be performed and large data bases generated.

However, the milling tools can be calibrated using a quick method known as mechanistic modelling [49]. In this method, a set of milling experiments are conducted at different feed rates with constant immersion and axial depth of cuts that are close to what the actual machining process will be. By capturing the forces acting on the part using a

dynamometer, average forces per cutting tooth can be calculated. Also, the influence of disturbances, such as run out and ambient noise, on the measurement instruments can be minimized by averaging the forces over a longer period of time (i.e. over many spindle revolutions). Experimentally computed average force magnitudes are then equated to the same value which is derived analytically and this result in a set of expressions that has the cutting coefficients as the only unknown variables.

The mechanistic equations are first derived analytically. Since the total material removed per tooth period is constant for each tooth with or without a helix angle, the average cutting forces can be calculated independently of the helix angle. This facilitates the calculations and results in the same final value as compared to when the helix angle effect is included in the calculations. Replacing $d_z = a$, $\phi_j(z) = \phi$, and $k_\beta = 0$ in Equation (3.11) and integrating over one full tool revolution and dividing by the pitch angle ($\phi_p = \frac{2\pi}{N}$) will result in the average milling forces per tooth period acting on the tool in each axis direction.

$$\bar{F}_x = \frac{1}{\phi_p} \int_{\phi_{st}}^{\phi_{ex}} F_x(\phi) d\phi$$

$$\bar{F}_y = \frac{1}{\phi_p} \int_{\phi_{st}}^{\phi_{ex}} F_y(\phi) d\phi \tag{3.17}$$

$$\bar{F}_z = \frac{1}{\phi_p} \int_{\phi_{st}}^{\phi_{ex}} F_z(\phi) d\phi$$

As stated before, the integration is only done within the immersion zone of $\phi_{st} \leq \phi \leq \phi_{ex}$, since in the other areas the force is zero and it will not affect the outcome of the integral. Performing integrals in Equation (3.17) results in:

$$\bar{F}_x = \left\{ \frac{Nac}{8\pi} \left[K_{tc} \cos 2\phi - K_{rc} [2\phi - \sin 2\phi] \right] \right.$$

$$\left. + \frac{Na}{2\pi} \left[-K_{te} \sin \phi + K_{re} \cos \phi \right] \right\}_{\phi_{st}}^{\phi_{ex}}$$

$$\bar{F}_y = \left\{ \frac{Nac}{8\pi} \left[K_{tc} (2\phi - \sin 2\phi) + K_{rc} \cos 2\phi \right] \right. \tag{3.18}$$

$$\left. - \frac{Na}{2\pi} \left[+K_{te} \cos \phi + K_{re} \sin \phi \right] \right\}_{\phi_{st}}^{\phi_{ex}}$$

$$\bar{F}_z = \frac{Na}{2\pi} \left[-K_{ac}c \cos \phi + K_{ae}\phi \right]_{\phi_{st}}^{\phi_{ex}}$$

It is most convenient to perform the milling tests in full immersion; therefore the entry ϕ_{st} and exit ϕ_{ex} angles will be replaced by 0 and π correspondingly. Simplifying Equation (3.18) with this assumption results in:

$$\bar{F}_x = -\frac{Na}{4} K_{rc}c - \frac{Na}{\pi} K_{re}$$

$$\bar{F}_y = +\frac{Na}{4} K_{tc}c + \frac{Na}{\pi} K_{te} \tag{3.19}$$

$$\bar{F}_z = +\frac{Na}{\pi} K_{ac}c + \frac{Na}{2} K_{ae}$$

To express the cutting forces as a linear function of feed rate (c) and an offset contributed by the edge forces, it is assumed that the following equations are valid:

$$\bar{F}_x = \overline{F_{xc}}c + \overline{F_{xe}}$$

$$\bar{F}_y = \overline{F_{yc}}c + \overline{F_{ye}} \tag{3.20}$$

$$\bar{F}_z = \overline{F_{zc}}c + \overline{F_{ze}}$$

44

Therefore all that is required after this stage is to use linear regression to fit a line on the data that has been captured from the experiments from the plot with the x axis being the feed rate parameter (c) and the y axis the average force value (F), This will result in the values of $\overline{F_{xc}}, \overline{F_{xe}}, \overline{F_{yc}}, \overline{F_{ye}}, \overline{F_{zc}}$ and $\overline{F_{ze}}$ to be determined. Substituting these values in Equation (3.20) and then equating these set of equations with the set of Equations (3.19) will result in explicit analytical relations that calculate the cutting coefficients as shown below in the final set of equations for the mechanistic model:

$$
\begin{aligned}
K_{tc} &= \frac{4\overline{F_{yc}}}{Na} & K_{te} &= \frac{\pi\overline{F_{ye}}}{Na} \\
K_{rc} &= \frac{-4\overline{F_{xc}}}{Na} & K_{re} &= \frac{-\pi\overline{F_{xe}}}{Na} \\
K_{ac} &= \frac{\pi\overline{F_{zc}}}{Na} & K_{ae} &= \frac{2\overline{F_{ze}}}{Na}
\end{aligned}
\tag{3.21}
$$

The above method and equations have been put to use to determine the set of values in Equations (3.8) through (3.16) for CPP, which will be used in planning machining operations conducted on this material.

3.5.1 Experimental Determination of Cutting Coefficients for CPP

To establish the cutting coefficients for CPP, cutting tests are required to determine the average forces as the first step. For this reason, equipment such as a dynamometer, charge amplifier, oscilloscope, and a computer with a data acquisition card and software were used. It is of outmost importance to be sure that all equipment is configured and set up correctly before conducting the tests, so that the resulting figures are correct. A previous study done in determining the cutting coefficients [6] had shown significantly

changing values over changing layers of CPP in the cutting force estimates. The author then concluded that the CPP has a very non-homogeneous structure when delivered as a block and that the cutting coefficients vary greatly from one layer to an adjacent one.

Therefore, it is suggested that the whole experimental setup and configurations and all other involved instruments and methods be validated by performing the exact procedure on a common engineering material such as Aluminum and then these results be compared with established values in engineering literature. Should the resulting cutting forces be fairly close to the established figures in engineering literature, then it may be concluded that the experimental setup and the calculation methods are correct. Hence, experiments on CPP can be conducted with confidence.

The experiments were conducted using a machining force measurement dynamometer, built by Kistler®(model 9255B 3-component Stationary Dynamometer). Below are the main technical specifications and a picture of this dynamometer:

Table 3-3: Technical Specifications for Kistler © 9225 stationary table dynamometer

Spec.	Parameter	Unit	Value
Measuring Range	F_x, F_y	kN	± 20
	F_z		$-10\dots 40$
Sensitivity	F_x, F_y	$\dfrac{pC}{N}$	~ -8
	F_z		~ -3.7
Natural Frequency	f_{nx}, f_{ny}	kHz	~ 2
	f_{nz}		~ 3.3
Operating Temperature Range		$^\circ C$	$0\dots 70$
Mass		kg	52

A flat endmill was selected for the experiments. The same tool was used in both the pilot aluminum cutting test and the final CPP tests. A 70% density CPP block with a 50-150micron particle sized at 41mm x 30mm x 28mm dimensions was used. The tool shown in Table 3-4 can make 8 cuts per layer as shown below in Figure 3-16 on this CPP block.

Table 3-4: Tool used in the mechanistic model cutting experiments

2 Flute Stub. Length Carbide Endmill – Inch				
Cutting Diameter	Shank Diameter	Flute Length	Overall Length	Code No.
3/16" (4.76mm)	3/16" (.76mm)	5/16" (7.9mm)	2" (50.8mm)	101-228
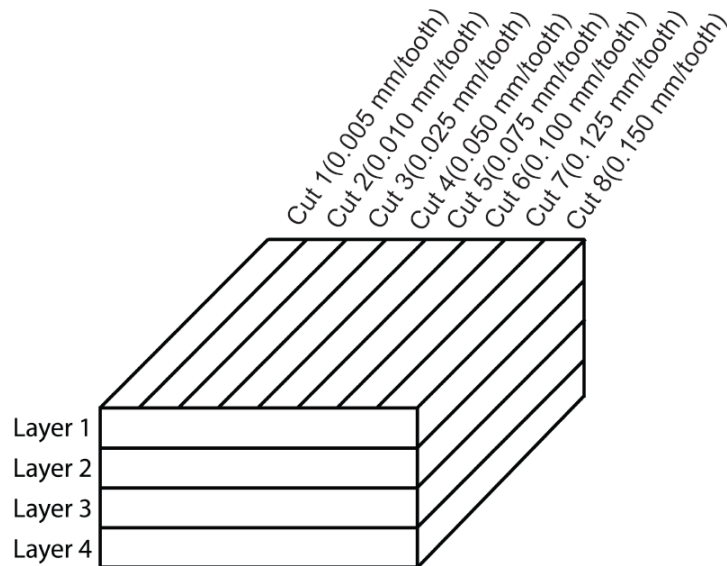
Figure 3-16: Cutting layers and feeds performed on the CPP block

One important aspect of this study is to see if the material's machining characteristics change from one layer to the other. In other words, if the cutting coefficients change as the tool cuts deeper into the workpiece material. If so, it can then be concluded that CPP, in its current sintered form, is not a perfectly homogenous material. The previous study [6] had shown that this seemed to be the case.

The following method was tested first on Aluminum and the resulting cutting coefficients matched closely to what was found in the literature. Therefore, it is expected that the determined cutting coefficients for CPP are correct and this will be verified by

comparing the simulated and experimental cutting forces, both for flat endmilling conditions used in identifying the parameters, as well as ball endmilling, which will be the main finishing operation used in producing the biphasic implants. Should the predicted cutting forces for ball endmilling match what is captured from the dynamometer, then it can be concluded that the cutting coefficients are fairly close in representing the machining characteristics of CPP.

3.5.2   Experimental Setup

A 70% density block with a 50-150micron particle size with 41mm x 30mm x 28mm dimensions was prepared at University of Toronto and delivered to the Precision Controls Laboratory at the University of Waterloo. The dynamometer detailed in Table 3-3 was mounted on the 3-axis CNC machine OKK MCV-410 manufactured by OKK located at the Computer Integrated Manufacturing Laboratory (CIMLab) at the University of Waterloo. The dynamometer was connected to the appropriate charge amplifier supplied by Kistler® and the output from the charge amplifier was sent to both a digital oscilloscope (54621D 2+16 Channel, 60MHz Mixed-Signal Oscilloscope, Agilent Technologies, Santa Clara, Ca, USA) as well as a Data Acquisition Card (NI DAQCard – 6062E, National Instruments, Austin TX 78759-3504, USA). The measurements obtained through the NI DAQCard were processed using CutPro®, which was set to capture the forces with no filtering at a frequency of 10kHz. These two data capturing instruments provided additional checking abilities and warned of problems in data capturing should they read different values. Figure 3-17 shows the experimental setup schematically. The CPP sample block was milled on all sides on a manual milling machine to bring it to an exact prismatic shape, in order to ensure the flatness of all sides. This was essential for the accuracy of the force measurements.
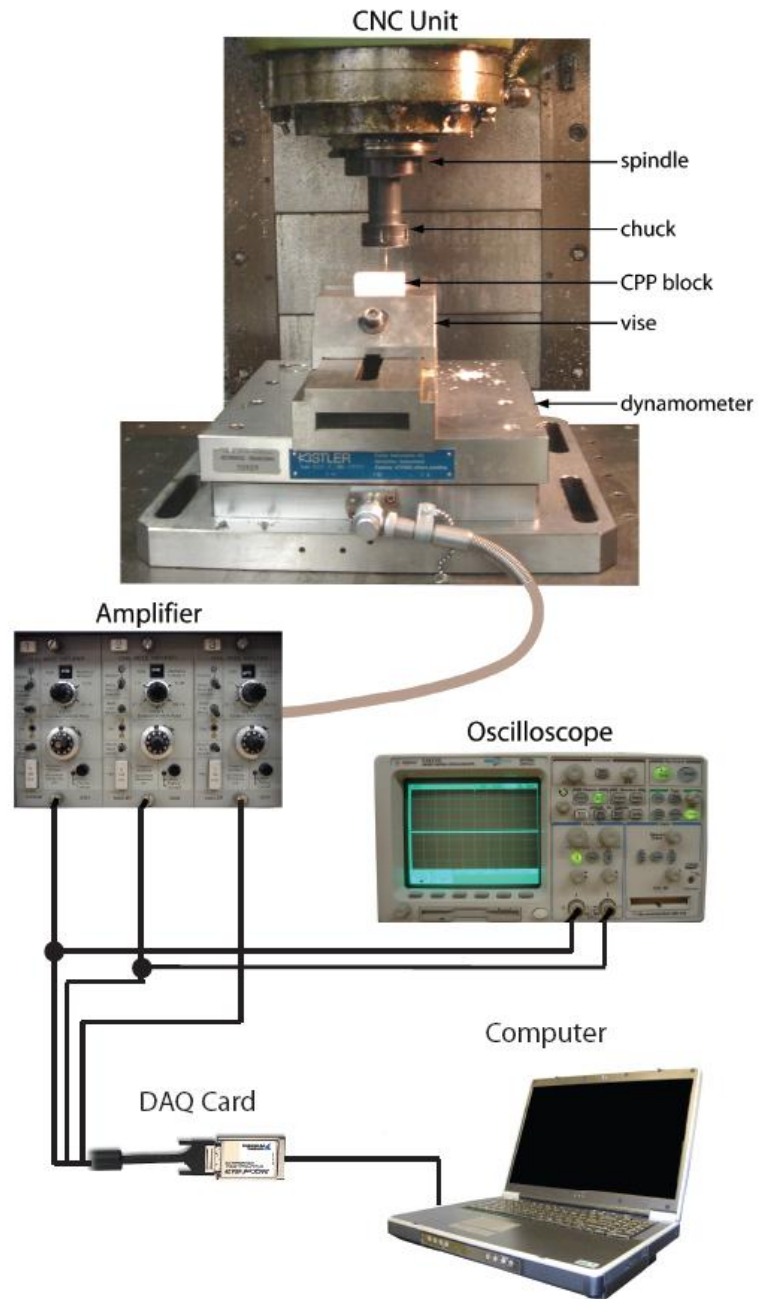
Figure 3-17: Experimental setup

3.5.3 Experimental Data and Identified Coefficients

The cutting coefficients were identified separately for three different layers of 1, 2, and 4 as shown in Figure 3-16, while ball endmilling cutting tests were performed on layer 3 for cutting force model verification. Ball endmilling is extensively used in producing the final freeform surfaces on the implant geometry. For layer 1, a cutting depth of 1.5mm was selected and the other two layers were chosen to be 2.5mm deep. The increase in the depth of cut was with the intention of getting higher z axis force readings, as it will be seen later on, determination of the z axis cutting coefficients was not possible due to very small forces in that direction. In all tests the spindle rotation velocity was held constant at 1500rev/min, which was observed from qualitative tests to result in acceptable surface porosity. The data was captured at 10kHz and for 13 seconds. Note that some higher cutting speeds were beyond what CPP could handle and resulted in chipping and breakage rather than machining. The forces captured in these cutting tests by the dynamometer were not consistent machining forces and therefore the average forces for these data sets are not reported here.

In the first set of machining tests, the depth of cut was 1.5mm. Below is a snapshot of the machining forces captured directly from the dynamometer at a feed rate of 0.01mm/tooth (Figure 3-18).
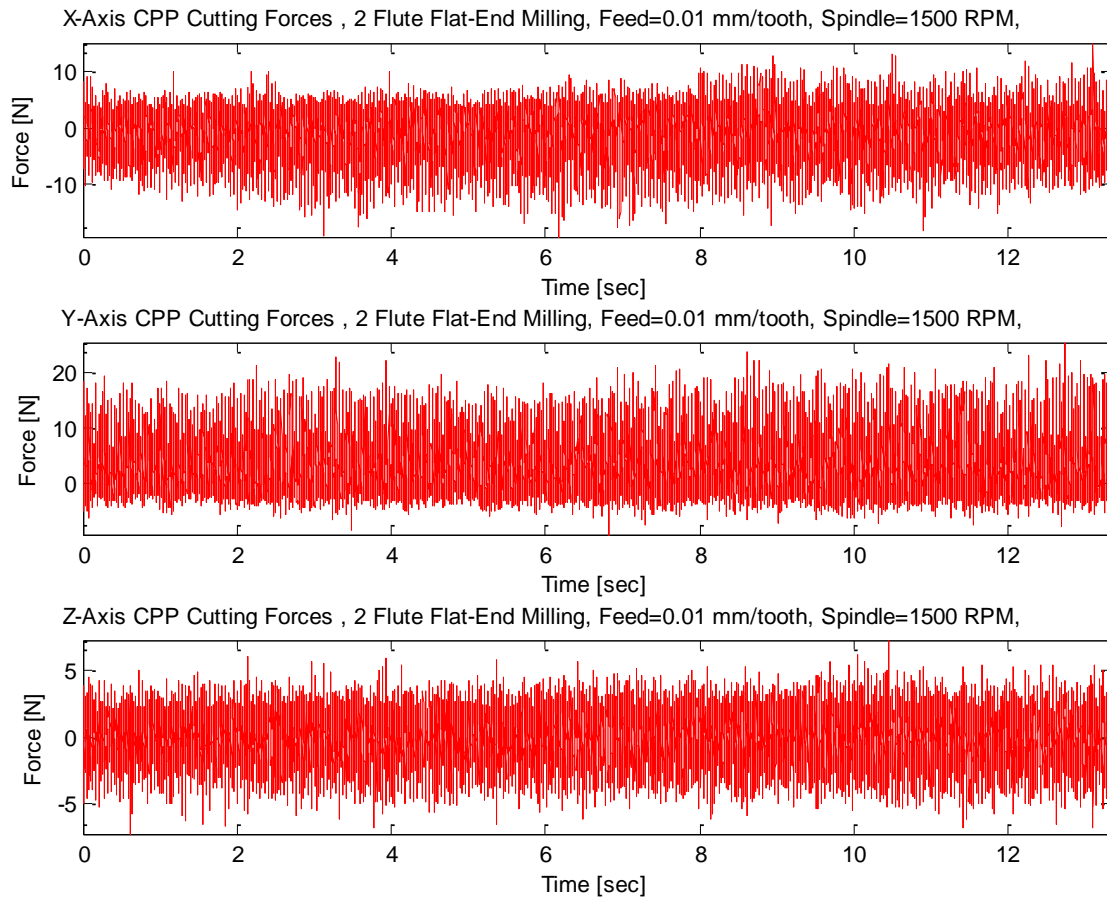
Figure 3-18: Raw cutting forces captured from the dynamometer at 0.01mm/tooth feedrate, 1500rev/min spindle speed and 1.5mm depth of cut.

As it can be observed, the forces are uniform in magnitude and chatter vibrations do not occur.

The tests show that at lower feed rates, the forces are uniform with time and at higher feed rates, they show inconsistency in magnitudes that could possibly be due to chatter vibrations. Therefore, the cutting force coefficient identification and surface machining planning was conducted at lower feed regions. Modelling the vibration characteristics of

the tool and workpiece could predict chatter cases. However, this was kept outside the focus of this thesis, and a rigid tool and workpiece was assumed in the simulations.

Referring back to Equation (3.21), it is required to average the cutting forces over a certain period of time (usually nearly a second of cutting). The numerical values of this averaging is included in Appendix A, and from that table, the following figures are composed in which the cutting coefficients are then derived from. If the cutting coefficients are to be calculated for each layer separately, that is, the change of material properties in different layers is investigated, then there will be different sets of cutting coefficients for CPP. Each set represents the layer at which the material was cut. Figure 3-19 shows the average forces for layer 2, while Figure 3-20 represents the average forces for layer 4 and displays cutting coefficients for CPP derived from tests conducted on layer 2. Data from Layer 1 was not used, as the higher force magnitudes generated in machining Layers 2 and 4 resulted in more reliable estimation of cutting force coefficients.
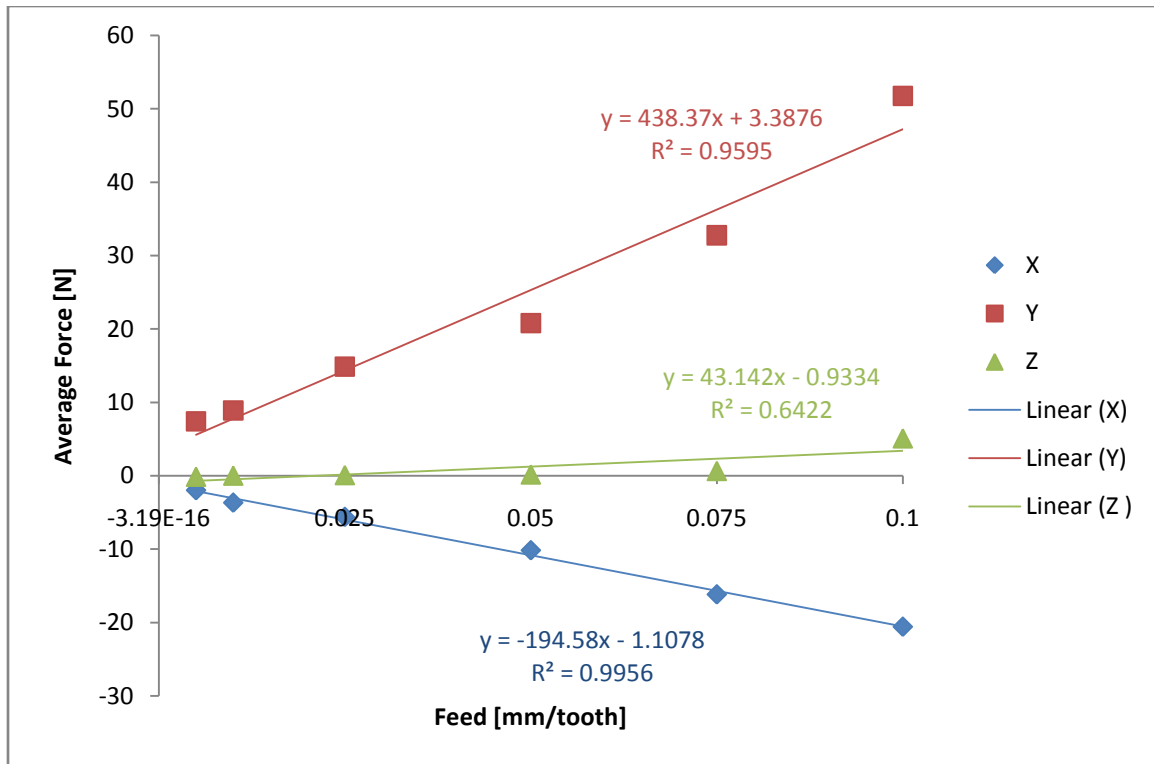
Figure 3-19: Average forces and linear regression for results from cutting tests on layer 2

Table 3-5: Average cutting coefficients for layer 2 (test results shown in Figure 3-19).

$K_{te}\left[\dfrac{N}{mm}\right] = 2.128$	$K_{tc}\left[\dfrac{N}{mm^2}\right] = 350.693$
$K_{re}\left[\dfrac{N}{mm}\right] = 0.696$	$K_{rc}\left[\dfrac{N}{mm^2}\right] = 155.66$
$K_{ae}\left[\dfrac{N}{mm}\right] = 0.373$	$K_{ac}\left[\dfrac{N}{mm^2}\right] = -27.106$

And for Layer 4, the results are found to be:
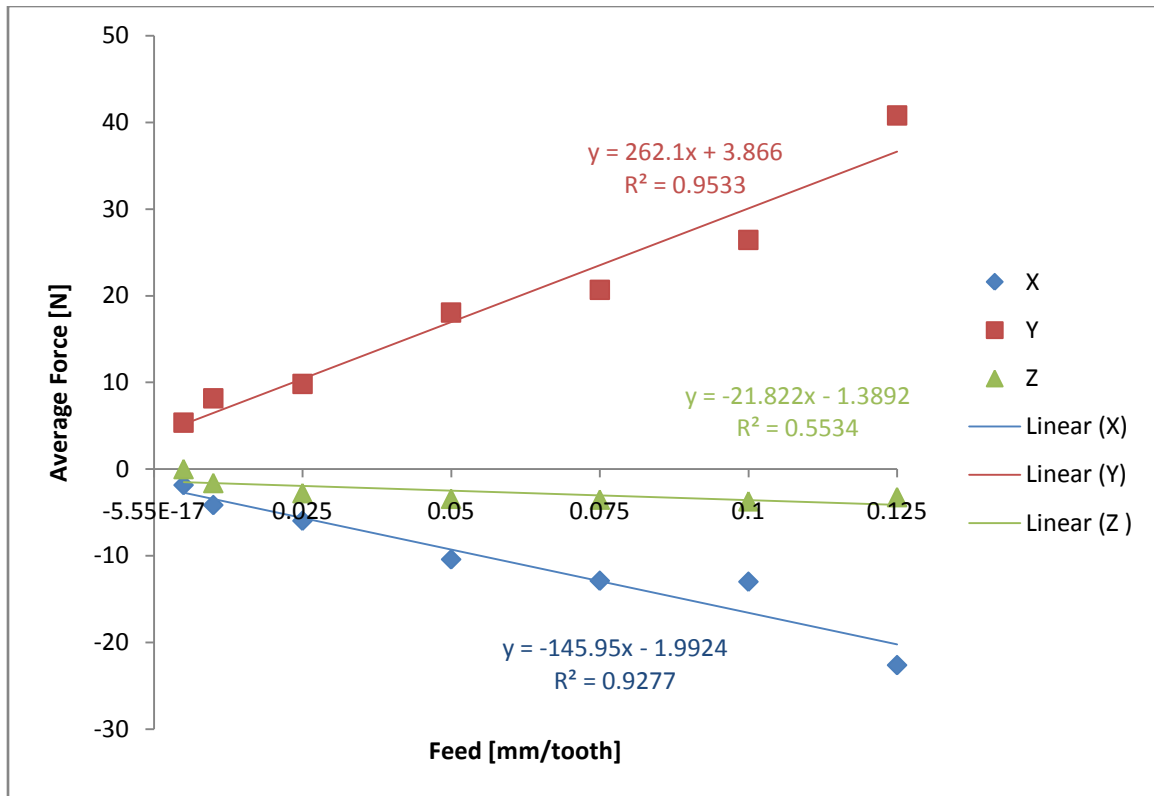
Figure 3-20: Average forces and linear regression for results from cutting tests on layer 4

Table 3-6: Average cutting coefficients resulting from layer 4 test results shown in Figure 3-20

$K_{te}\left[\dfrac{N}{mm}\right] = 2.024$	$K_{tc}\left[\dfrac{N}{mm^2}\right] = 211.057$
$K_{re}\left[\dfrac{N}{mm}\right] = 0.882$	$K_{rc}\left[\dfrac{N}{mm^2}\right] = 118.016$
$K_{ae}\left[\dfrac{N}{mm}\right] = 0.545$	$K_{ac}\left[\dfrac{N}{mm^2}\right] = 13.751$

In order to present an average set of cutting coefficients that represent the material's properties in general, the above two charts are superimposed on each other and another linear regression is performed. The final cutting coefficients for the 70% density, 50-150 micron particle size CPP block that the tests were conducted on are reported here, as shown in Figure 3-21 and Table 3-7.
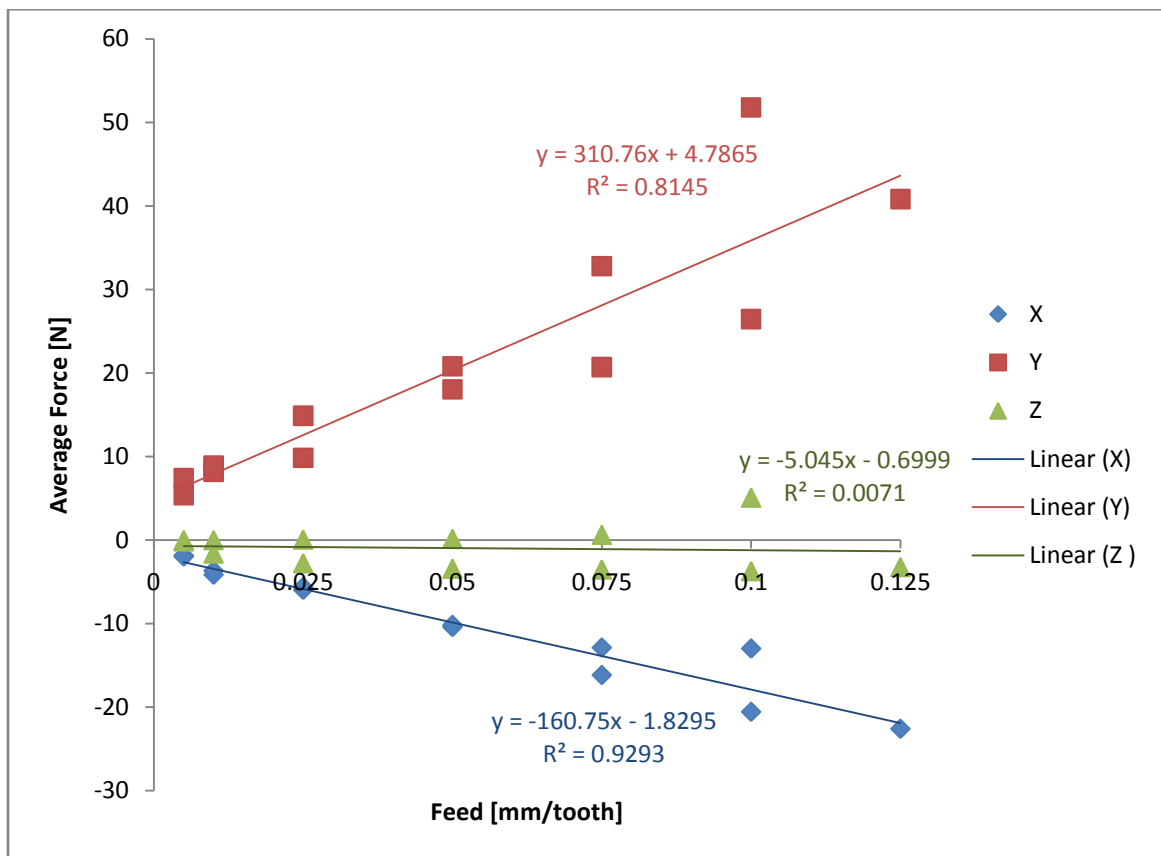
Figure 3-21: Average forces and linear regression for results from cutting tests on layers 2 and 4 combined

$K_{te} \left[\dfrac{N}{mm} \right] = 3.155$	$K_{tc} \left[\dfrac{N}{mm^2} \right] = 225.887$
$K_{re} \left[\dfrac{N}{mm} \right] = 0.896$	$K_{rc} \left[\dfrac{N}{mm^2} \right] = 134.161$
$K_{ae} \left[\dfrac{N}{mm} \right] = 0.161$	$K_{ac} \left[\dfrac{N}{mm^2} \right] = 12.72$

Table 3-7: Average cutting coefficients resulting from combined layers 4 and 2 test results shown in Figure 3-21

Considering the above figures and tables, it can be seen that the linear model fits each separate layer well, but shows variation in coefficients from layer to layer. This indicates that CPP's mechanistic properties change with depth, that is, the material is not homogeneous. Results from earlier studies confirm this property of the material as well [6].

To see how well this model predicts the cutting forces captured from the dynamometer, the milling cutting forces were simulated in all three axes, and then overlaid on respective experimentally recorded force profiles using the same flat endmill tool. Since the model is essentially derived from fitting these measurements, it was expected that a close match between the simulated and measured cutting forces would be observed. The more important verification for the model comes in the next section, where the cutting forces will be predicted for a spherical endmilling operation, which was not used in calibrating the cutting force coefficients.

If the cutting forces are presented without any filtering, then ambient noise and influence of mechanical vibrations from surrounding machinery and the machining process itself will appear in the force measurements. However, to demonstrate that the filtering method used here does not impede the accuracy of the comparative results, both the filtered and raw data are included on the same graph, as well as the simulated forces from the CPP mechanistic model. The filter used is a second order Butterworth filter with

57

a cut-off frequency of 250Hz. The following figures are for results derived from cutting of the second layer and the cutting coefficients values used are from Table 3-2.

Figure 3-22: Simulated and experimental data for 3/16″ diameter, 2-flute flat endmill at 1500rev/min and 0.005mm/tooth feed, full immersion. From top to bottom, the plots refer to x, y and z axes respectively.

Figure 3-23: Simulated and experimental data for 3/16″ diameter, 2-flute flat endmill at 1500rev/min and 0.01mm/tooth feed, full immersion. From top to bottom, the plots refer to x, y and z axes respectively.
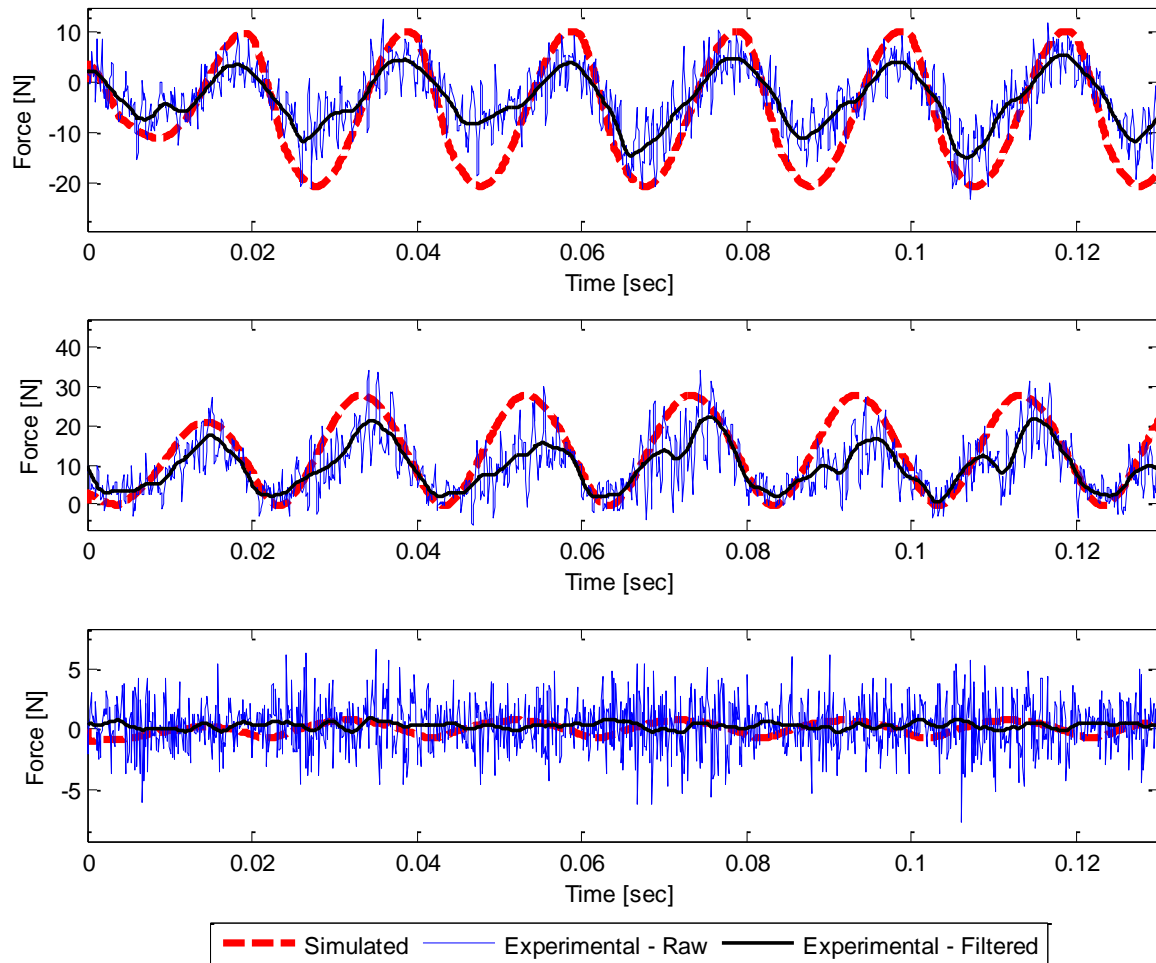
Figure 3-24: Simulated and experimental data for 3/16″ diameter, 2-flute flat endmill at 1500rev/min and 0.025mm/tooth feed, full immersion. From top to bottom, the plots refer to *x*, *y* and *z* axes respectively.
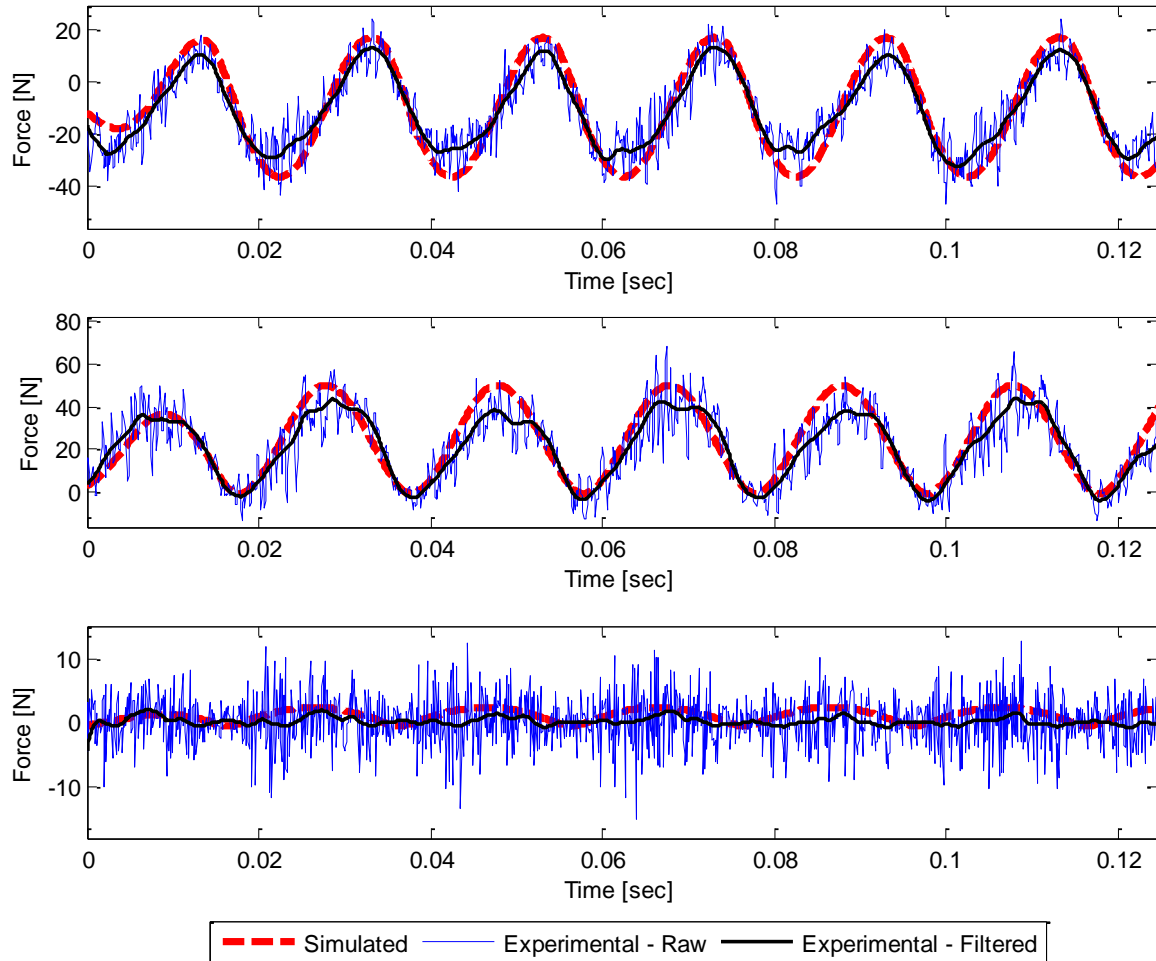
Figure 3-25: Simulated and experimental data for 3/16″ diameter, 2-flute flat endmill at 1500rev/min and 0.050mm/tooth feed, full immersion. From top to bottom, the plots refer to x, y and z axes respectively.
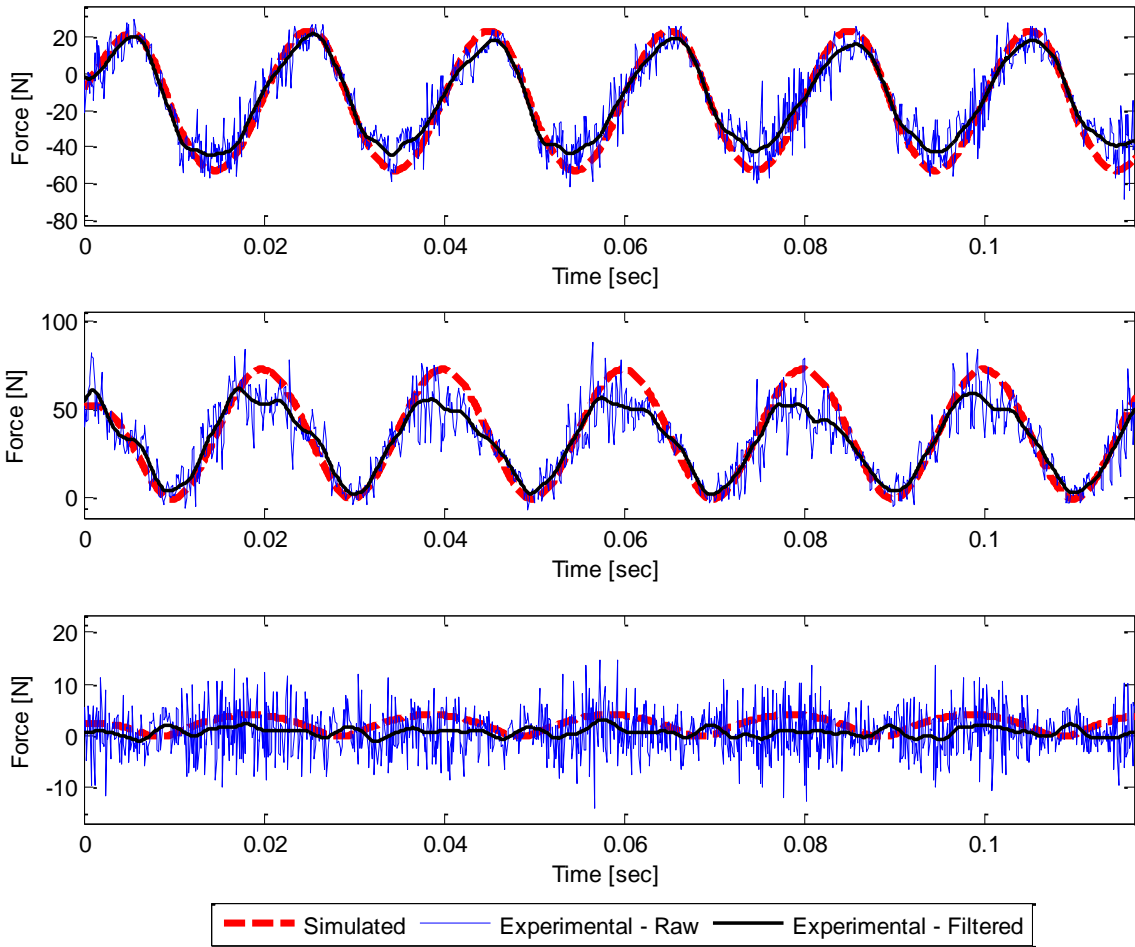
Figure 3-26: Simulated and experimental data for 3/16″ diameter, 2-flute flat endmill at 1500rev/min and 0.075mm/tooth feed, full immersion. From top to bottom, the plots refer to *x*, *y* and *z* axes respectively.
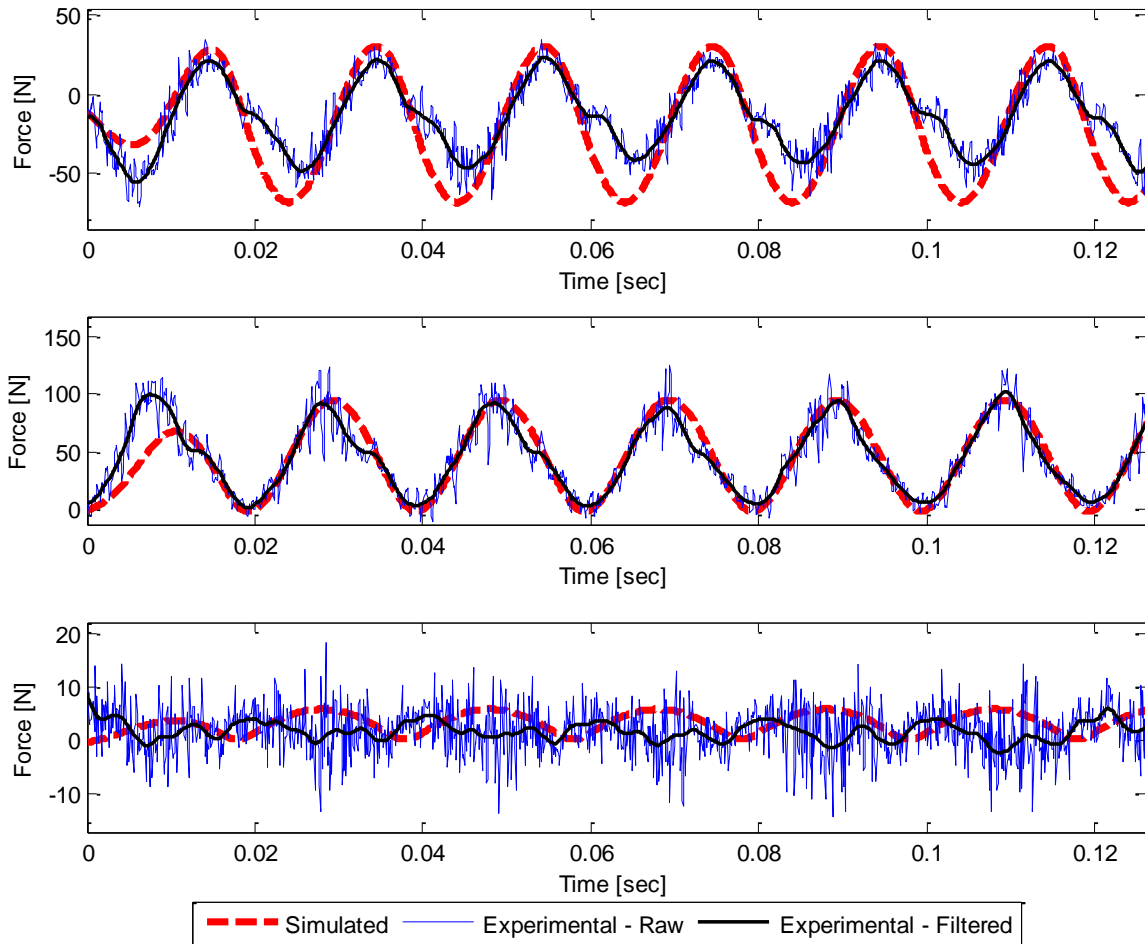
Figure 3-27: Simulated and experimental data for $3/16''$ diameter, 2-flute flat endmill at 1500rev/min and 0.1mm/tooth feed, full immersion. From top to bottom, the plots refer to x, y and z axes respectively.

As it can be observed from the above figures, the simulated and experimental data match reasonably close, especially in the feed (x) and mostly in the normal (y) directions. The magnitude of forces registered in the axial (z) direction is too small to be distinguished from noise. This noise may be a result of tool or workpiece vibration, electromagnetic noise from the environment affecting the measuring instruments or other factors such as tool dullness.

63

One important observation during these tests was that when forces in either the x or y axis were above the 45 Newtons range, chipping and breakage started to occur. In other words, rather than CPP being machined, material was removed due to breakage of material and therefore, at all times, the forces must be held below 45 Newtons.

3.6   Cutting Force Model Validation

In order to validate the model from the previous section, predicted cutting forces for a different milling operation, namely spherical endmilling, were compared to experimental readings. In the flat endmilling results, reported in the previous section, the model was "made" to fit the recorded forces and the cutting coefficients were calculated to make these two plots match. To fully validate the model, the cutting forces for a milling operation were predicted with a different tool, i.e. a spherical endmill using the CPP mechanistic model against data captured from experiments conducted with the exact same tool and conditions. Again, these two results are overlaid and checked to see if the model is able to predict these cutting forces.

The following tool was used in performing the cutting tests:

2 Flute Stub. Length Carbide Endmill – Inch				
Cutting Diameter	Shank Diameter	Flute Length	Overall Length	Code No.
3/16" (4.76mm)	3/16 (4.76mm)	5/16 (7.9mm)	2 (50.8mm)	101-247

Table 3-8: Tool used in the mechanistic model verification cutting experiments [48]

The cutting conditions were kept the same, which represented the optimal conditions that resulted in acceptable surface porosity, without causing chipping. The cuts used were full-immersion at 2.5mm axial depth of cut with the spindle speed of 1500rev/min. The feed rates range from 0.005 up to 0.125mm/tooth. The setup is the same as shown in Figure 3-17, and the results are shown below. The simulation used the cutting coefficient values described in Table 3-7. Due to the geometrical complexity of ball endmilling, the simulation algorithm available in CutPro® was used.
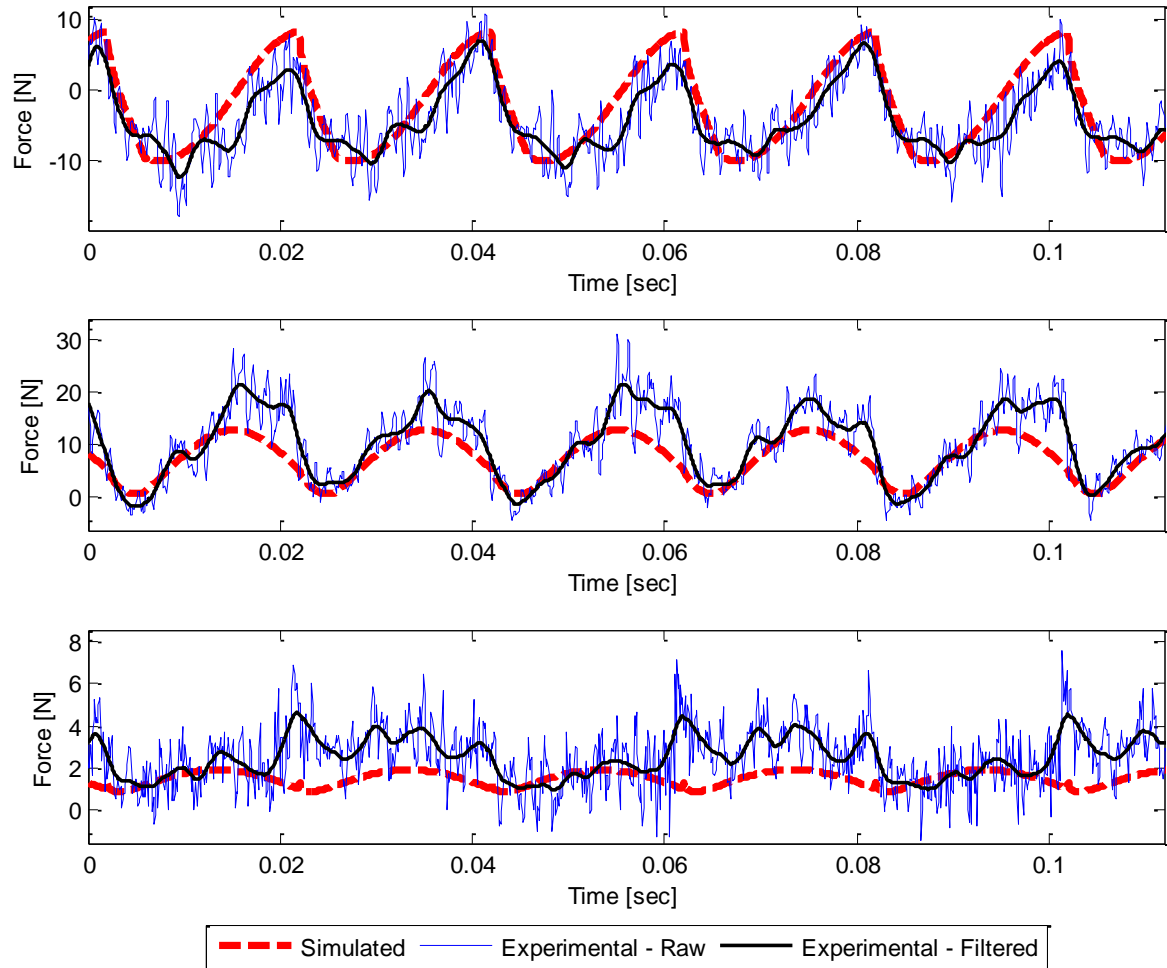
Figure 3-28: Simulated (CutPro) and experimental data for 3/16″ diameter, 2-flute spherical endmill at 1500rev/min and 0.005mm/tooth feed, full immersion. From top to bottom, the plots refer to x, y and z axes respectively.
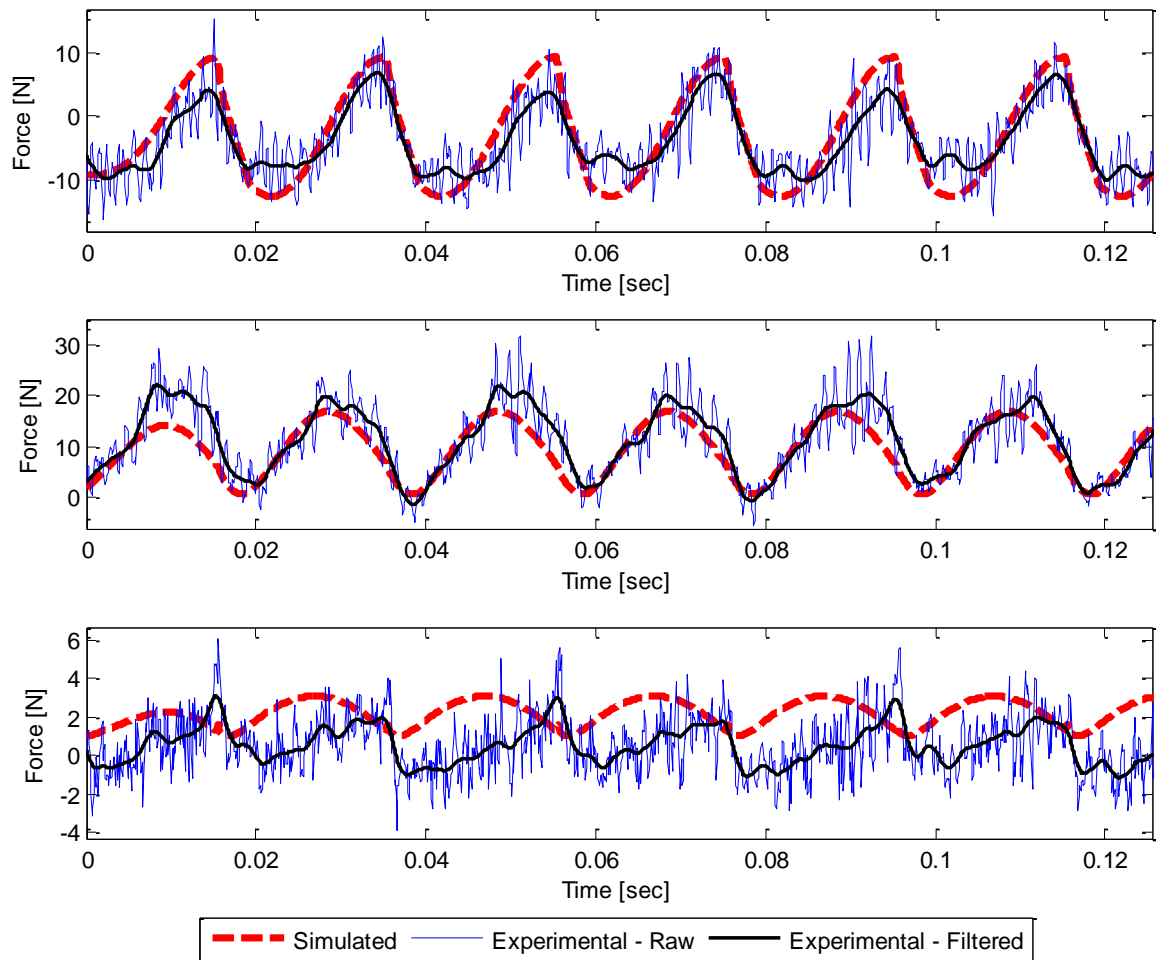
Figure 3-29: Simulated (CutPro) and experimental data for 3/16″ diameter, 2-flute spherical endmill at 1500rev/min and 0.01mm/tooth feed, full immersion. From top to bottom, the plots refer to x, y and z axes respectively.
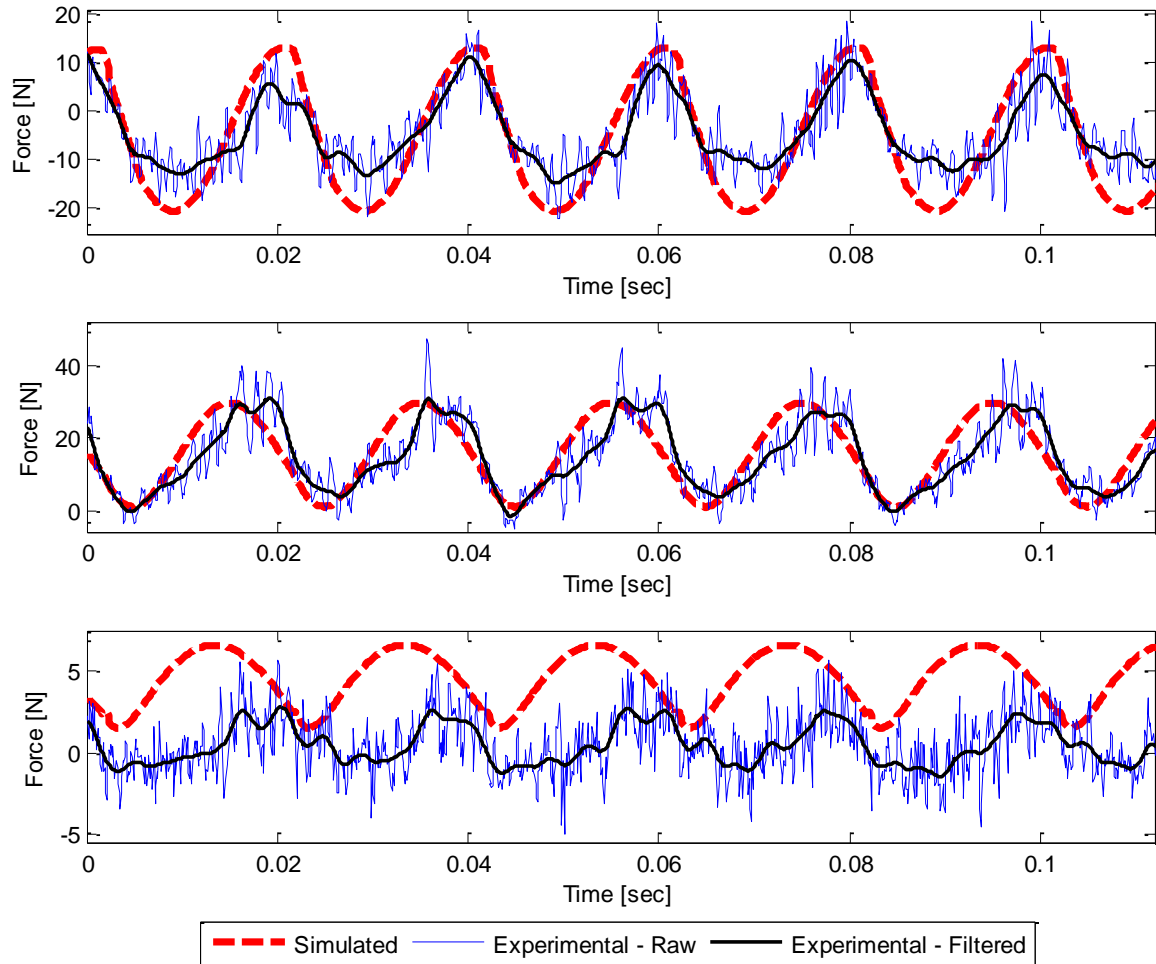
Figure 3-30: Simulated (CutPro) and experimental data for 3/16″ diameter, 2-flute spherical endmill at 1500rev/min and 0.025mm/tooth feed, full immersion. From top to bottom, the plots refer to x, y and z axes respectively.
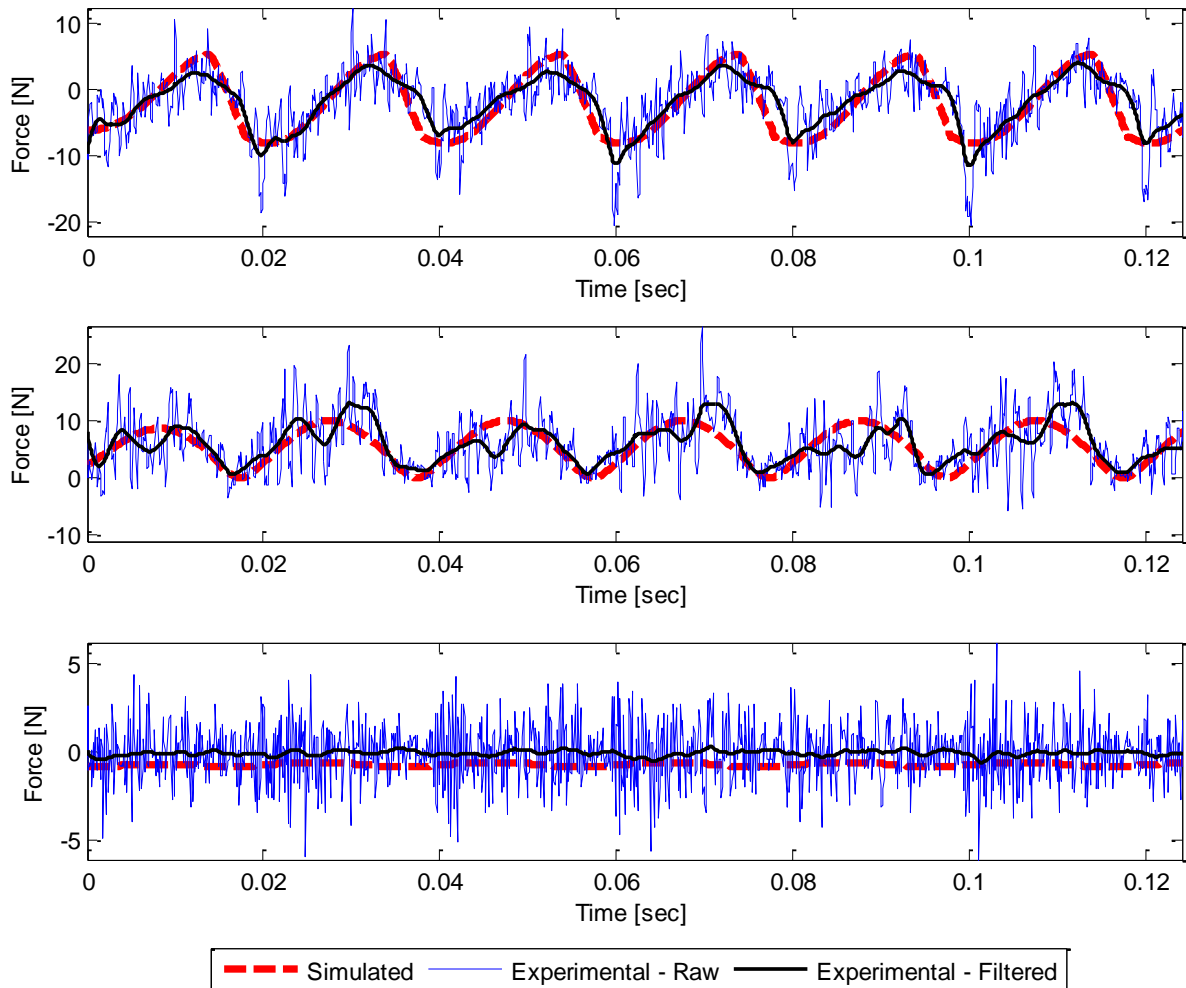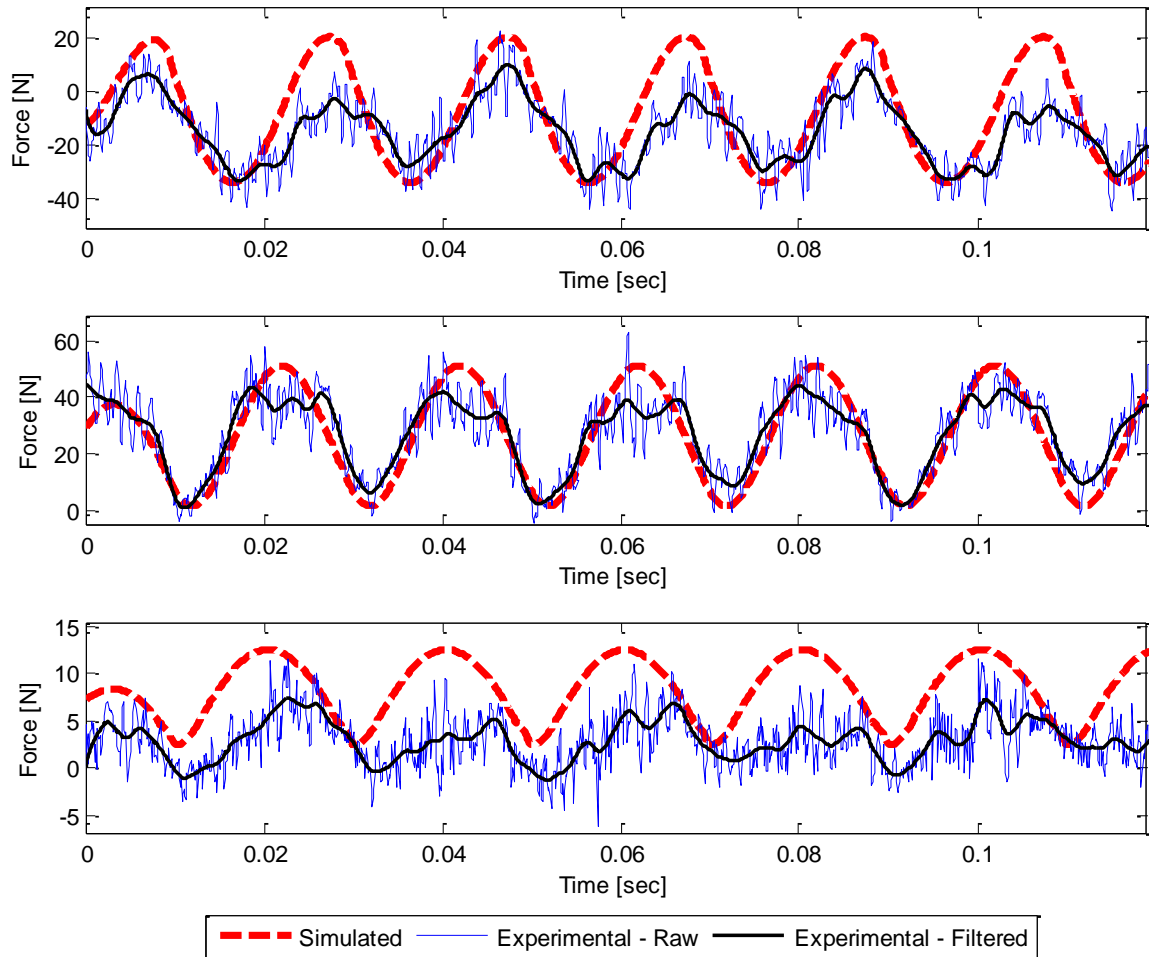
Figure 3-31: Simulated (CutPro) and experimental data for 3/16" diameter, 2-flute spherical endmill at 1500rev/min and 0.050mm/tooth feed, full immersion. From top to bottom, the plots refer to x, y and z axes respectively.
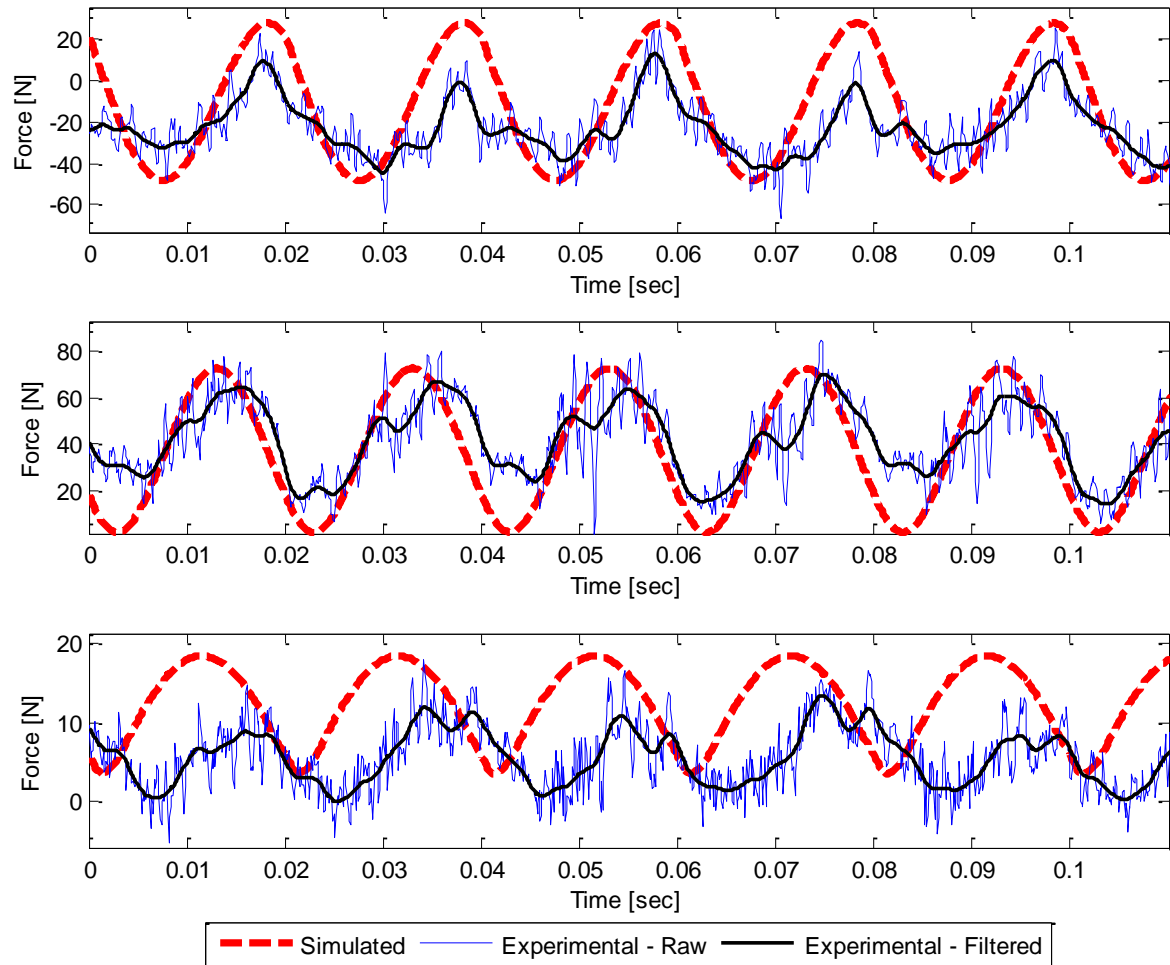
Figure 3-32: Simulated (CutPro) and experimental data for 3/16″ diameter, 2-flute spherical endmill at 1500rev/min and 0.075mm/tooth feed, full immersion. From top to bottom, the plots refer to x, y and z axes respectively.
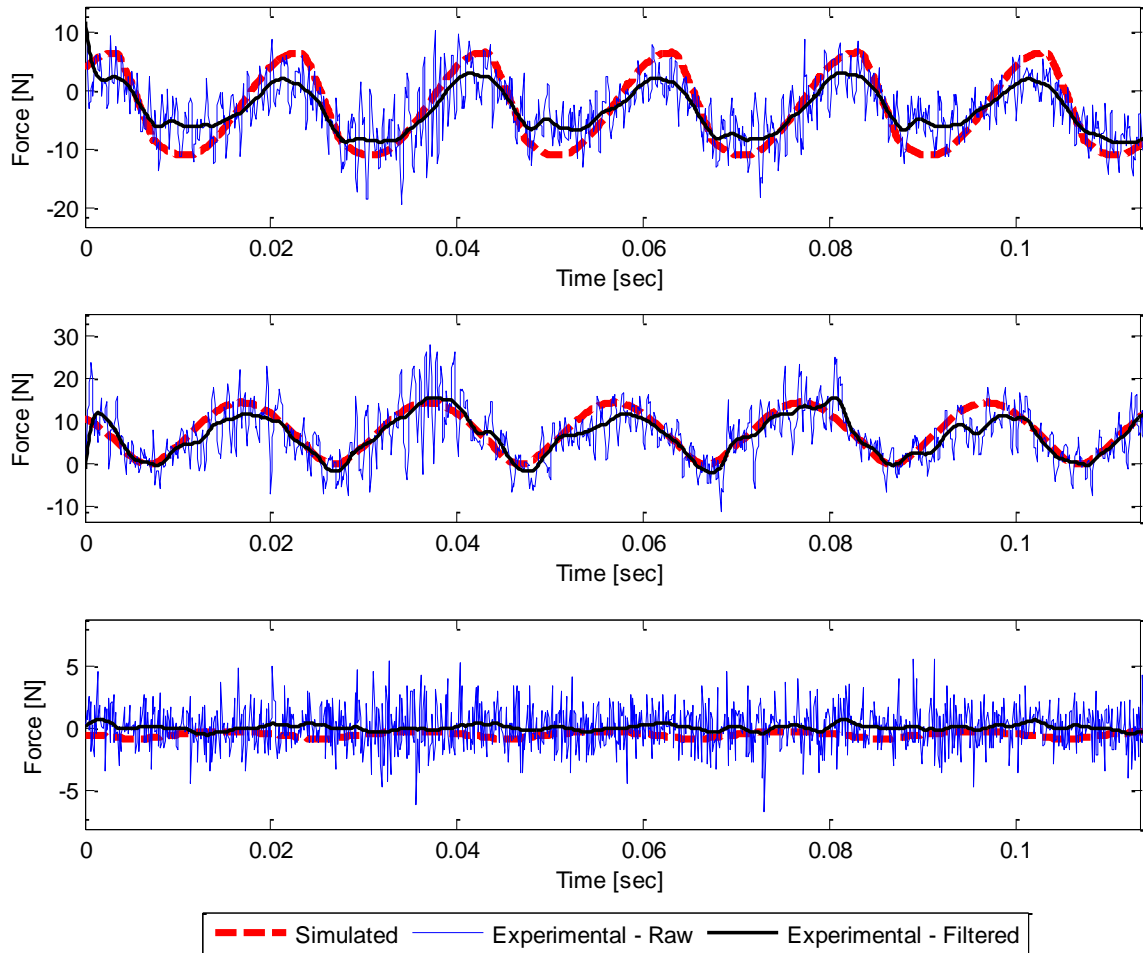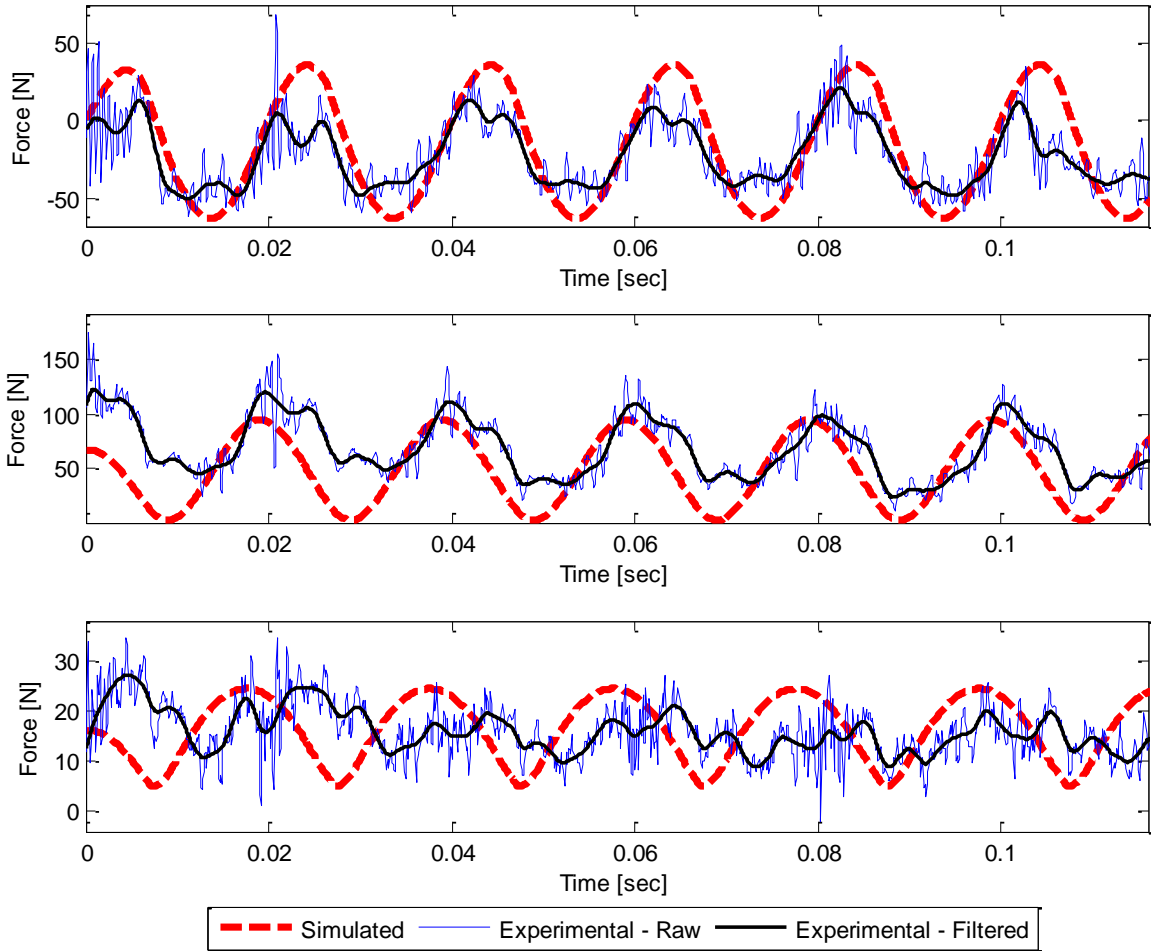
Figure 3-33: Simulated (CutPro) and experimental data for 3/16″ diameter, 2-flute spherical endmill at 1500rev/min and 0.1mm/tooth feed, full immersion. From top to bottom, the plots refer to x, y and z axes respectively.

71

By taking a closer look at the figures above, it is observed that force predictions are satisfactory when feed rates are kept low, i.e. below 0.050mm/tooth. However, as the forces increase with increasing feed rates, tool deflection and vibration become more prominent factors and simulation results start deviating from experimental observations. Although the general trend of the cutting forces are captured and force magnitude predictions are within acceptable ranges, they are not as good as what was observed for flat endmill experiments discussed earlier in section 3.5. This however, is not an issue since as it was demonstrated in section 3.2, the cutting speeds should be kept below 0.1mm/tooth to prevent chipping and breakage. This is since the forces should be kept below a maximum of 45 Newtons.

The z axis force predictions and values are fairly small and there seems to be significant presence of noise in these experimental measurements. This could be one reason why the z axis force predictions are not as accurate as the other two axes.

3.7   Optimal Feed and Rotational Speed

By taking into account factors that were discussed in this chapter such as machining forces (section 3.4), chipping (section 3.2.3), and surface porosity (section 3.2.2), it is concluded that the following are the optimal conditions for CPP machining.

The tool diameter is to be kept small, the operations should all be up-milling and the rotational speed is to be set at 1500rev/min with feed to be maximum 0.100mm/flute (i.e. 350mm/sec tangential cutting velocity for tool in Table 3-2) while air cooling is running to evacuate the CPP particles from clogging up the grooves of the cutter. The depth of cut should be kept to a maximum of 3mm and although full immersion cutting is acceptable, cutting is to be limited to half or less immersion. The maximum force acting in the x or y axis should be kept below 45 Newtons to prevent chipping and breakage.

3.8   Conclusion

In this chapter, using an SEM and subsequent qualitative measurements, optimal cutting conditions that resulted in minimum chipping and maximum porosity were determined and presented, which will be used in planning the multi-axis machining operation presented in Chapter 4.

The underlying theory of metal cutting mechanics was presented, followed by a procedure already established in literature for identifying cutting coefficients in metals, which was used in this study for CPP. In this method, a force measurement setup was used and cutting experiments were conducted on a block of CPP. The captured forces, which were consistent and did not contain chatter vibrations, were used in identifying the cutting force coefficients.

The cutting force coefficients were determined for the 70% dense, 50-150 micron CPP, which will be used as the biphasic implant construct. The resulting mechanistic model was verified by comparing the simulated forces with experimental data for both flat and spherical endmilling. It was concluded that the mechanistic model is sufficiently reliable for predicting the cutting forces and can be used as a process planning tool in developing the necessary surface machining operations.

Chapter 4

Computer Aided Manufacturing (CAM) Toolpath Generation and Multi-Axis Machining of the Implant

4.1   Introduction

Both Computer Aided Design (CAD) and Computer Aided Manufacturing (CAM) are part of the wider area of technology of Computer Aided Engineering (CAE). By taking advantage of many aspects of CAD, CAM software introduces the power of computers and streamline manufacturing processes [55]. In definition, CAM refers to the application of computerized technology to the manufacturing or production processes [56]. Blanchard describes CAM as consisting of activities such as Process Planning, Numerical Control (NC), Robotics and Production Management [56]. In manufacturing the bone implant, each distinct part of the manufacturing process must be looked at in detail. As an overview, each step of this process is described briefly below. Detailed investigation of each step will be described in upcoming sections.

4.1.1   CAD Model of the Implant

The first step in the manufacturing process is to generate the implant's shape in CAD software. This model is of outmost importance since the final product is designed in this stage and any error in this part of design will propagate to the final product. The development of this CAD model was mainly done at Ryerson University's department of mechanical and industrial engineering. Dudi and Papini [57] designed the substrate by extracting data from Computer Axial Tomography (CAT) images, which were derived from multiple scans of a sheep's knee as shown in Figure 4-1.
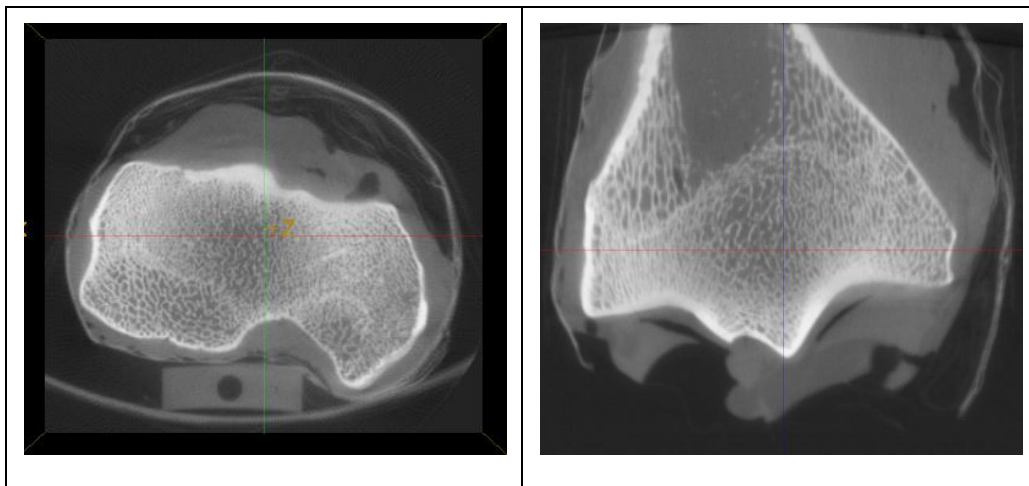
Figure 4-1: Computer Axial Tomography (CAT) images of a tibial plateau from different angles [6]
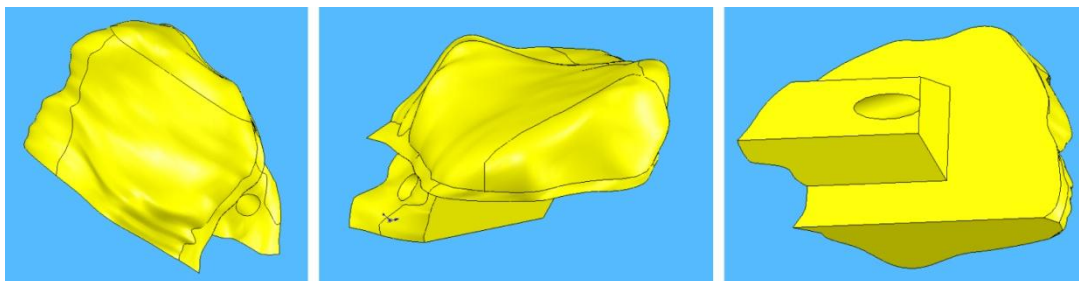
Figure 4-2: Earlier substrate design by Dudi and Papini (2007) [57]

The substrate's shape and overall design is influenced by three major factors: i) patient specific design of the complex freeform surface on the top, which results in a favourable mechanical environment for cartilage layer growth and resistance against static and dynamic loads, ii) a hole in which a biodegradable screw or pin can attach the implant to the host, and iii) simulation of stresses and strains on the implant using Finite Element Analysis (FEA). Modifications to the above design were later introduced at Ryerson University and the most recent CAD model was obtained as shown in Figure 4-3.

The goal was set to manufacture the latest version of the implant design as shown in Figure 4-3. The CAD model is designed in SolidWorks © (SolidWorks Corp., Concord, MA, USA) environment and is available as a single part file format know as .SLDPRT. It is worth noting here that the hole feature can be removed for Multi-Axis machining purposes and then a drilling process will be generating the final required through-hole. A snapshot of the implant with the hole removed is included in Figure 4-4. Note that the surface extends all the way to cover where the hole is to be drilled.
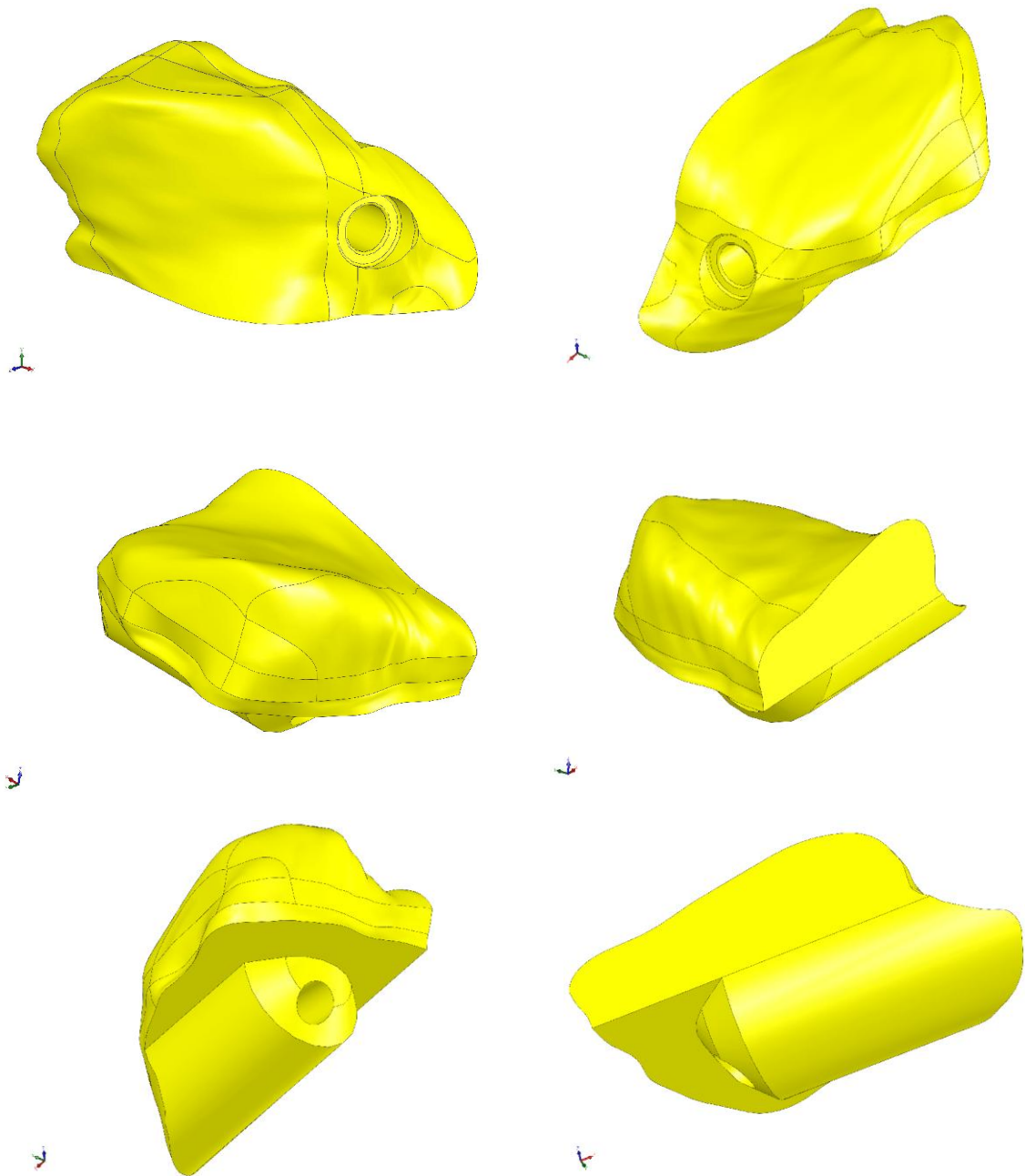
Figure 4-3: Latest Implant Design by Papini (2007)
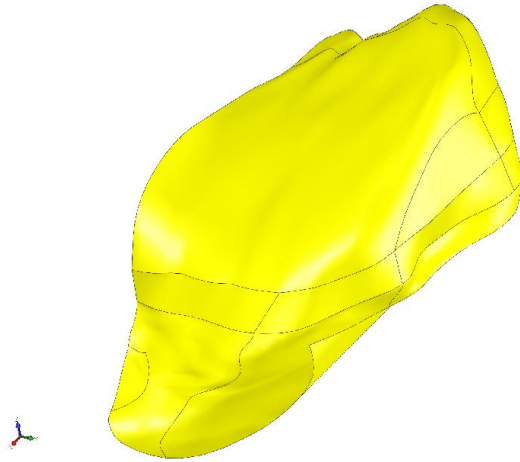
Figure 4-4: Final implant with the "through hole" feature removed (Design by Papini 2007)

4.1.2 CAM Software and Multi-Axis Toolpath Generation

Due to the complexity of the freeform surfaces and the arbitrary spatial hole to be drilled, manual machining methods is not an option. Shifting attention to Computer Numerical Controlled (CNC) machining processes, a choice must be made on how many degrees of freedom are required to machine this implant. As the number of degrees of freedom on a machine is increased, more complex parts may be machined and less number of setups is required. However, programming a multi-axis toolpath is far more complex, time consuming, and introduces much more risk of collision and thus machine damage and possible operator injuries when compared to 2.5 or 3 axis toolpaths. The following table gives a qualitative comparison of different machining options, compiled from author's experience.

	Machining Method				
	2.5 Axis	3 Axis	4 Axis	3+2 Axis (see below)	Full 5-Axis
Ability to Machine Complex Surfaces	Very Limited	Limited	Moderate	Extensive	Extensive
Can Machine Parts with Overlapping Sections	No	No	Some Scenarios	Yes	Yes
Relative Time Required to Program	Very Short	Short	Moderate	Very Long	Long
Relative Risk of Collision	Very Low	Low	Moderate	High	Very High
CAM Post Processor Availability	Abundant	Abundant	Moderate	Low	Low
Relative Cost of Machine	Low	Low	Moderate	High	Very High

Table 4-1: Qualitative comparison of different milling methods

For more information on post-processor availability, refer to section 4.1.4.

3+2 Axis milling is defined when the x, y and z axes are simultaneously movable but the fourth and fifth axes act as stationary indexing axes. For instance, if the machine has a trunnion (i.e. tilt + rotary) table that enables the fourth and fifth axis movement, then this table can only be positioned when other axes, i.e. x, y and z are stationary and not moving. From the above discussion, it is evident that any full five-axis machine can be programmed to be a 3+2 axis machine.

In order to choose the best available machining option, the following steps are taken to reach a decision. First, the options that are by nature unable to machine the implant are eliminated. This eliminates any machine with less than 5 axes, as some sections of the implant have overlapping features and would be impossible to reach with a machine that has less than 5 axes. Also, since the possibility of producing this part using CAD/CAM implementation is currently being investigated, simultaneous full five-axis method is chosen rather than the 3+2 axis option. Although the 3+2 axis method has prospects of introducing higher productivity and less machining time, this option was removed to enable use of the more complex machining abilities of the full five-axis machining method. The objective here is to first show this manufacturing method is possible, and then to optimize it.

Considering what was discussed above, the milling toolpaths must be designed using CAM software that has the ability to generate multi-axis movements. Considering the complex nature of this implant, features such as collision check and final product simulation are a necessity. The CAM software used here was developed by CNC Software, Inc. (671 Old Post Road, Tolland CT, 06084 USA) known as MasterCAM® and a Post-Processor was developed with collaboration with In-House Solutions Co. (240, Holiday Inn Drive, Unit A, Cambridge, Ontario, Canada, N3C 3X4). More Information on the software and the developed post processor is available in Section 4.2.

4.1.3 Deckel Maho Gildemeister (DMG) 80 P hi-dyn CNC Universal Machining Center

The Deckel Maho Gildemeister (DMG) 80 P hi-dyn machine is a universal milling machine with the performance and construction of machining centers [58]. The machine is located at the University of Waterloo's Computer Integrated Manufacturing Laboratory (CIMLab) and is shown in Figure 4-5.

Figure 4-5: The DMG 80 P hi-dyn machine located at CIMLab with all 5 axis designated

The machine is a full five axis machine with rotary-swivel Numerically Controlled (NC) trunnion table, and the ability to change between horizontal and vertical machining positions using an innovative universal swivel milling head as shown in Figure 4-6.
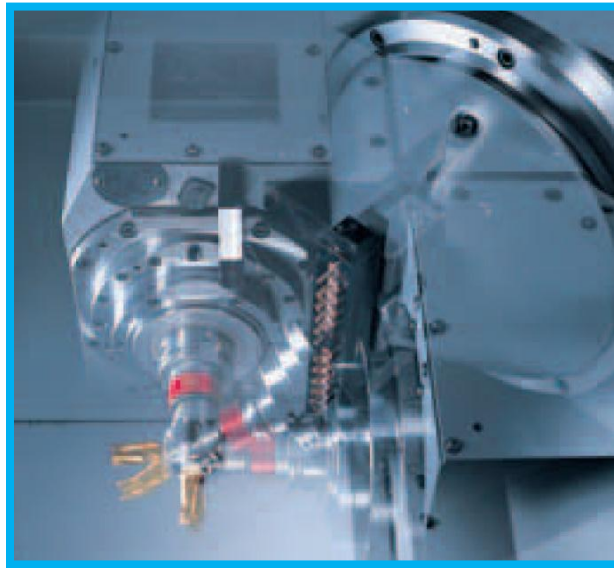
Figure 4-6: Universal swivel milling head that can take multiple positions. In this case, horizontal and vertical positions [58]

This machine enables machining of the implant in a single setup.

4.1.4   Heidenhain TNC 426 M Controller

The DMG machine is equipped with the TNC 426 M controller from Heidenhain. The Heidenhain contouring controls are designed for use with milling, drilling, and boring machines as well as machining centers. The TNC 426 M features integral digital drive control and controls the power stages via PWM signals. The TNC 426 M offers digital control for up to 5 axes and spindle speeds up to 30000rev/min [59]. Since this controller uses a different language than the conventional G-Code language, the final machine interpretable code that the CAM software generates must be in this language. This raises the need for a post-processor that translates CAM data from the software to

this particular language. More information on the post processor development and related issues is available in Section 4.2.8.

4.2   CAM Toolpath Generation

In this section, the main focus will be on the development of toolpaths that when executed on the specific CNC machine, will generate the final required shape of the implant. The section starts with a description of the available CAM software, getting a closer look at the chosen software followed by an explanation of the importing procedure of the CAD file. This will be followed by an explanation of each operation created in the software and its application, prediction of cutting forces in that particular operation using the mechanistic model that was developed in Chapter 3, and then a final look at the simulation results and what the actual implant is expected to look like after machining. The section concludes with testing of the toolpaths on wax and then CPP, where the final implant is machined.

Figure 4-8 shows an overview of the steps taken to form a CPP block into the shape of the bone implant which will be discussed in detail later on. The goal of this thesis is to shape a block of CPP to have the form of the implant shown in Figure 4-3. This is illustrated below in Figure 4-7.
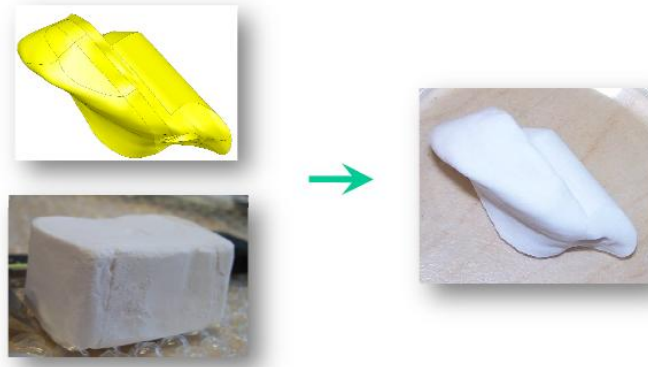
Figure 4-7: Figure showing the overall objective of this chapter. The CPP block at left of the arrow is to be shaped according to the CAD model at the left of the arrow to have the final implant shape shown at the right of the arrow.
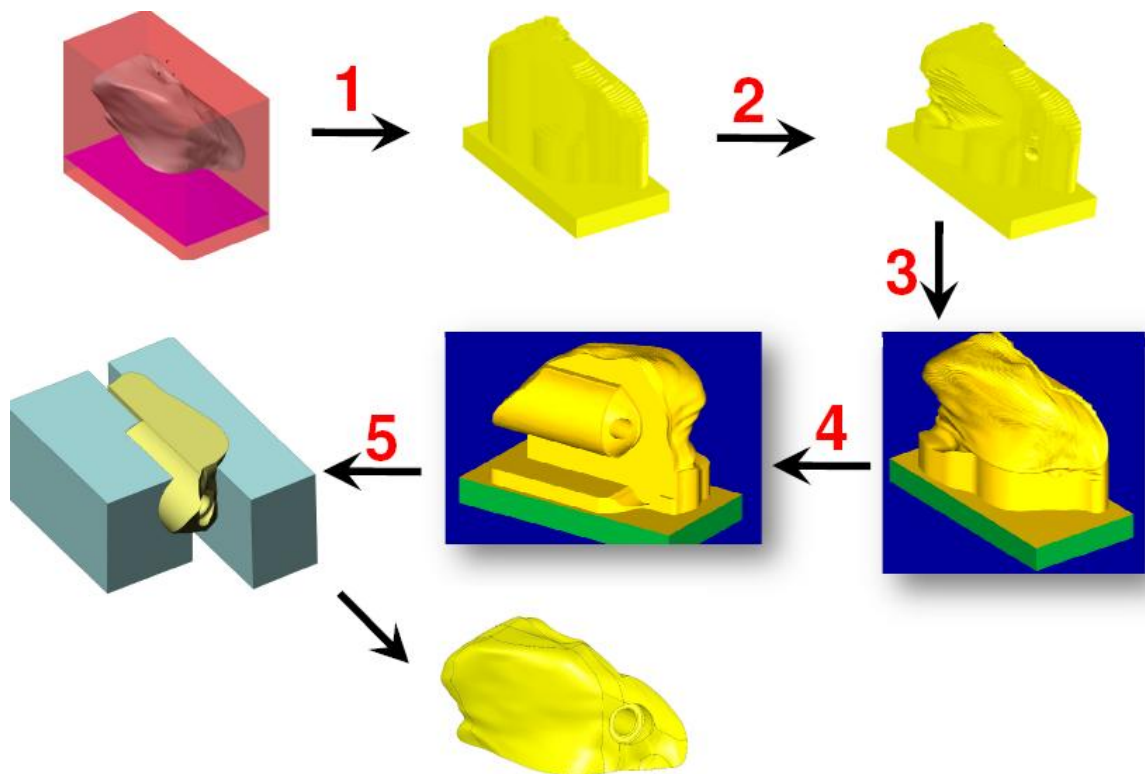
Figure 4-8: An overview of the machining process, starting with a block of CPP represented by the pink block. Step one is a three-axis rough machining process, followed by rough five-axis machining process in step two. Step three and four are finishing operations involving multi-axis milling and drilling. Step five shows the clamping of the part for final milling.

It is worthwhile to note that the described steps are only one solution to this machining problem. There are numerous setups/operations available that can be implemented to generate the final implant, possibly there may be even faster and better overall machining strategies that can produce the implant with the given specifications in shorter cycle times. The procedure presented here was developed following 1.5 years of development on the 5-axis machining operation, and the substrate was machined and delivered to the surgeons for implantation. Therefore, as stated before, the major focus of this machining trial was to show the possibility of producing this part using multi-axis CNC machining approach, and then to optimize the process as much as possible, within the framework of this thesis.

4.2.1   Commercial CAM Software

There is a wide variety of CAM software available in the market, each having certain strengths and weaknesses. One important factor in CAM software choice is the availability or ability of development of a reliable post-processor. In definition, a post processor translates the machining procedure defined by the user in the CAM software environment to a lower level language that can be interpreted and executed by the machine. The choice for CAD or CAM packages depends not only on the technical aspects of the software, but also other factors such as price and after sales support. To machine the bone implant, certain features and conditions listed below were required to enable this process. The technical requirements are:

i)   Must natively support importing SolidWorks® CAD file with format .SLDPRT

ii)   Must support full five-axis toolpath programming

iii)   Highly recommended to have collision checking ability

iv)   Highly recommended to have final part simulation feature, which will enable the simulation and examination of the final machined part in the software's environment without needing to machine a prototype

The non-technical features of the software can be identified as:

i)   Must have an affordable price

ii)   Have training programs or facilities at a reasonable cost

iii)   Be able to provide customized post-processor for the available specific machine(s)

MasterCAM © Version X2 MR1 SP1 (CNC Software Inc.) was used for the development of the toolpaths since it is already utilized at the University of Waterloo. Also, In-House Solutions Co. which is located locally provided assistance in developing a customized post-processor for the DMG machine tool.

4.2.2   Importing the Implant CAD file into MasterCAM

As stated in section 4.2.1, MasterCAM has the ability to read native SolidWorks® files. However, MasterCAM will not be able to recognize or edit any of the features that were created in SolidWorks®. In other words, MasterCAM will only translate the file to a solid object. Having stated this, it is important to i) remove the through hole feature from the model as shown in Figure 4-4 before attempting import and also ii) rotate the part such that the flat surface located on the side of the implant is facing downwards in the z axis and lying on the xy face as shown below in Figure 4-9.
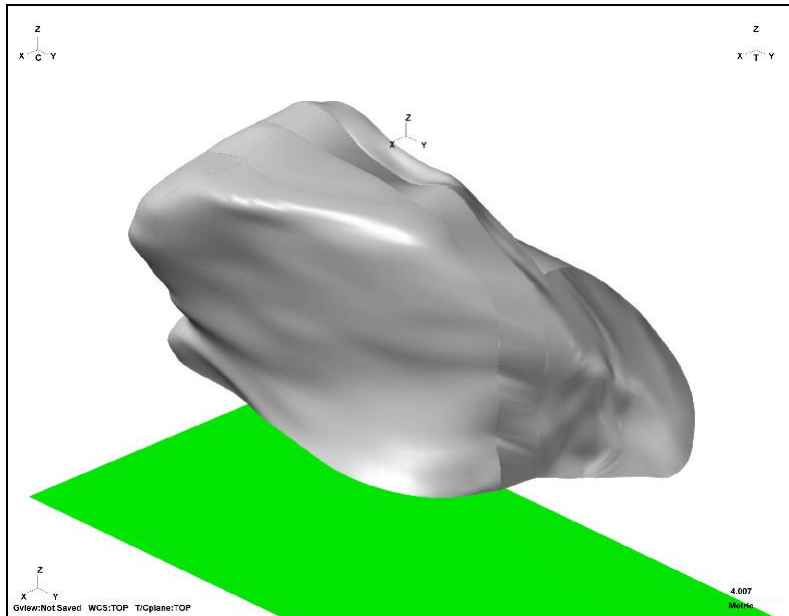
Figure 4-9: Implant CAD file with hole feature removed and rotated, imported to MasterCAM. Note the orientation of the axis.

The rationale behind removing the through hole feature is that it introduces discontinuity in the surface of the implant. This way, the full surface will be machined first and then the hole is drilled using a multi-axis drilling operation rather than milling out a hole.

4.2.3　Three-axis Roughing Operation

The first milling operation removes excess material from the block and leaves a nominal 1mm or more material for the multi surface operation to be performed afterwards. The roughing part consists of two steps in which the first step is a "Surface Rough Pocket" operation and has a step-down size of 3mm, and then a "Surface Finish Contour" operation with a step-down of 1mm. These two operations reduce the CPP block from its cubic shape to a rough shape ready for the next multi-axis step as shown below in Figure 4-10.

87
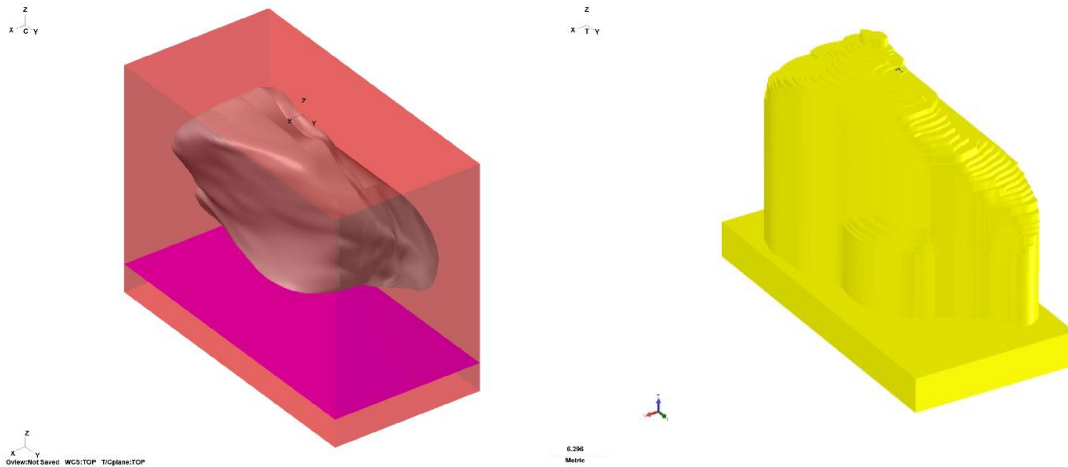
Figure 4-10: 3-Axis roughing procedure on the blank CPP block (left image, red box) and the resulting part on right.

The following tool has been used in this operation, procured from by Sowa Tool and Machine Co. Ltd. (Kitchener, Ontario, Canada, N2G 4B6) [48]:

Table 4-2: Description of tool used for the first roughing operation [48]

4 Flute X-Long Length – TiAlN Coated				
Cutting Diameter	Shank Diameter	Flute Length	Overall Length	Code No.
3/16" (4.76mm)	3/16" (4.76mm)	1-1/8" (28.5mm)	3" (76.2mm)	102-552

Using the mechanistic model developed in the previous chapter, the forces in this operation are predicted and the cutting conditions are chosen for the forces not to exceed a maximum of 50N at any time. This is because experimental results have shown that when forces exceed this amount, chipping and breakage prevails as a problem. The cutting coefficients used in these determinations are from Table 3-5.

The operation specifications are as listed below:

Table 4-3: Operation specifications for section 4.2.3

Coolant: Air Blast	Morph spiral cutting, outside to inside
Feed Rate: 75mm/sec	*Stepover distance*: 3/32" (2.38mm)
Plunge Rate: 75mm/sec	*Spindle speed:* 1500rev/min
Total Tolerance: 0.025mm	*Maximum depth of cut*: 3.0mm

The forces are predicted to be as followed:

Figure 4-11: Predicted forces in the x(top) and y(bottom) axes using the mechanistic model developed in chapter 3. Note that these forces are predicted for the operation specifications shown in Table 4-3

The three-axis operation only takes out parts in which overlap does not occur. In sections with overlap, the tool is not able to reach and remove the excess material. This has raised the need for a multi-axis roughing operation to reach those areas and complete the roughing operation.

4.2.4   Multi-Axis Roughing Operation

As stated in the previous section, the first multi-axis toolpath was a roughing operation. The reason a roughing operation is needed before machining out the final surface is that a 1mm ball endmill is used to generate the final surface. This tool has a flute length of only 3mm. Therefore, should the tool engage in cutting depths of more than 3mm at any time during the course of machining, a tool breakage will result. In other words, the tool can only cut to a maximum of its flute length. Hence, to reduce the amount of material that needs to be removed during the machining operation, a multi-axis process is developed to follow the original 3-axis roughing.

In this operation, a larger ball endmill (3/32") is used to increase the machining speed, with its ability to cut deeper to reach the 1mm pre-finish depth. A snapshot of the machining toolpath on the surface of the implant is shown below in Figure 4-12.
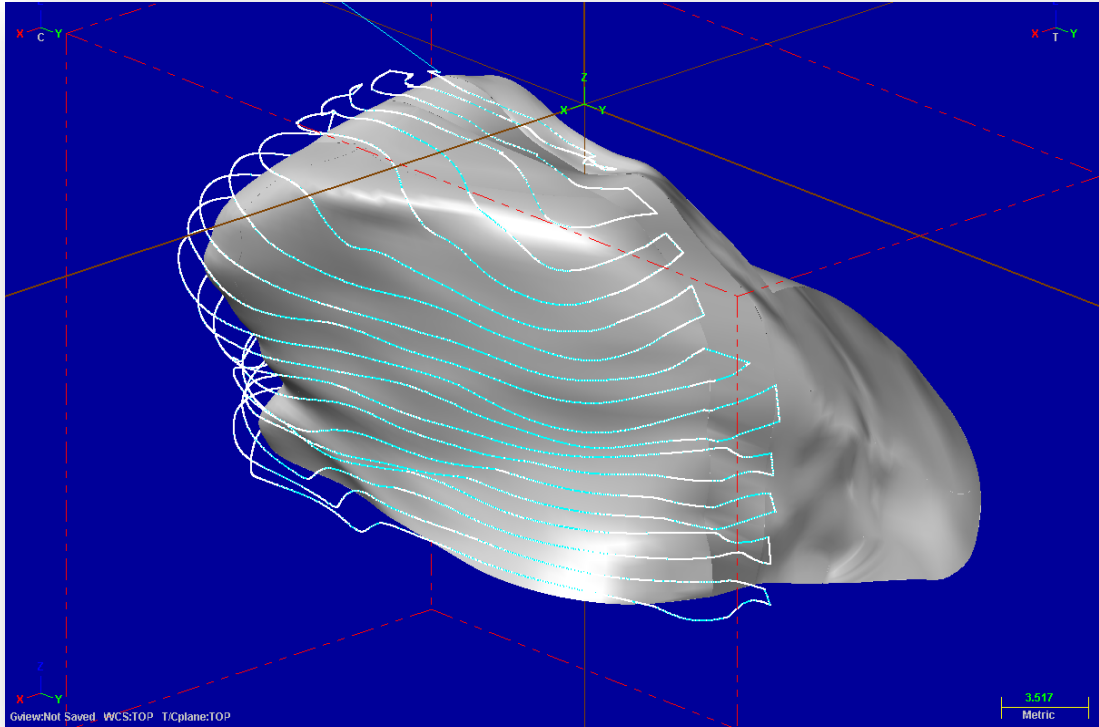
Figure 4-12: Multi-axis toolpaths generated for the roughing operation. Note that the toolpath is the white line that scans the surface of the implant.

The tool parameters are included below:

Table 4-4: Description of tool used in the roughing operation in section 4.2.4 [48]

3 Fl. Ball Nose Regular Length - Inch				
Cutting Diameter (in.)	Shank Diameter (in.)	Flute Length (in.)	Overall Length (in.)	Code No.
3/32	1/8	5/16	1-1/2	101-112

Again, using the mechanistic model developed previously, a set of cutting conditions are chosen as shown below:

Table 4-5: Operation specifications for section 4.2.4

Operation Name: 5-Axis Multi-Surface	*Coolant:* Air Blast
Feed Rate: 150mm/sec	*Immersion*: 3/32" (2.381mm) Full
Plunge Rate: 150mm/sec	*Spindle speed:* 1500rev/min
Total Tolerance: 0.07mm	*Maximum Depth of cut*: 1.0mm

And the predicted forces for this case are (using the same cutting coefficients from Table 3-5):
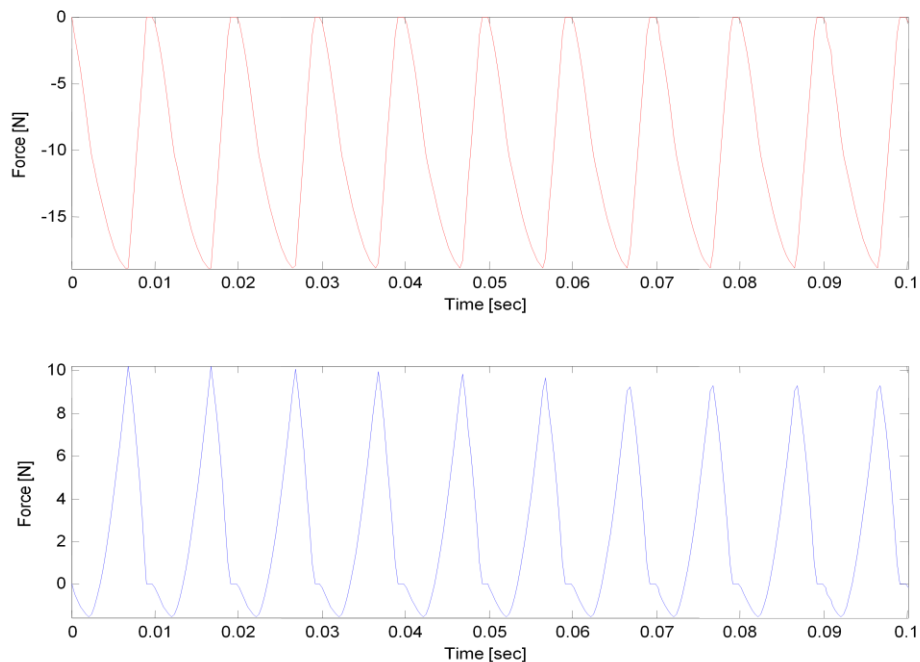

Figure 4-13: Predicted forces in the x(top) and y(bottom) axes using the mechanistic model developed in chapter 3. Note that these forces are predicted for the operation specifications shown in Table 4-5.

The part will look as followed after the roughing stage is complete.
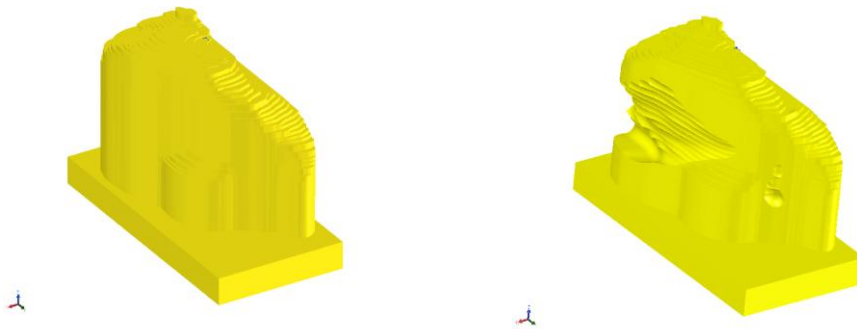
Figure 4-14: The 5-Axis roughing operation of section 4.2.4 completes the roughing stage from the previous state (left) to the final roughed part on right.

4.2.5   Multi-Axis Surface Finishing

In this section, the final shaping of the complex surface of the implant is discussed. Using a 1mm ball endmill and with small passes of just 0.25mm, the final surface of the implant was generated with the desired accuracy. Shaping of the keel part of the implant and the hole are still remaining, however, the most complex part of the machining process is completed at this point.

An important issue that must be considered here is that the DMG 80 P machine can only machine angles of 0 to +45º in the vertical position or +45 to +90º in the horizontal spindle swivel position in the simultaneous full five-axis mode. This is because the machine needs to retract and then change position from horizontal to vertical or vice versa. In order to eliminate frequent retracting movement of the machine, the machining process must be restricted on each individual surface to be either in the 0º to +45º or the +45º to +90º configuration. To do so, the restriction around the Z axis option was enabled in the software's options menu and set either to 0º to +45º or +45º to +90º. It is recommended for these values to be set to 0º to +44º or +46º to +89º to eliminate

boundary value problems that sometimes occur in the post-processing section of the process. When machining the top surfaces of the implant, 0º to +44º were used and for the side surfaces, +46º to +89º.

Taking the above notes into consideration, a 5-axis multi-surface toolpath was generated and, as shown in Figure 4-15, note the orientation of the toolpath lines, which run from top to bottom in a horizontal way.
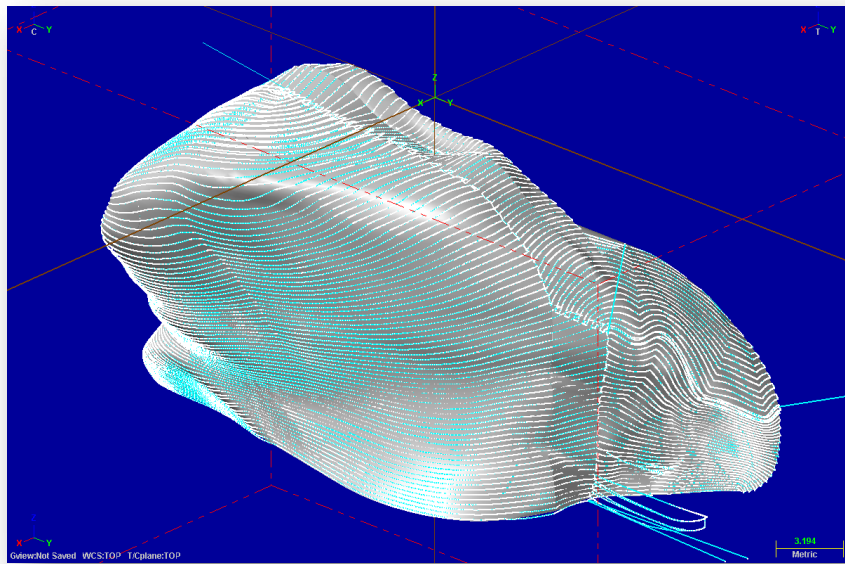
Figure 4-15: Multi-Axis toolpaths to generate the final shape of the implant surface

The tool parameters used in these operation parameters are included below:

Table 4-6: Description of tool used in the multi-axis finishing operation for section 4.2.5 [48]

3 Fl. Ball Nose Regular Length – Metric				
Cutting Diameter (mm)	Shank Diameter (mm)	Flute Length (mm)	Overall Length (mm)	Code No.
1	3	3	39	101-520

Again, the operation specifications are selected to preserve surface porosity and prevent chipping and by using the experimental results of the previous chapter and the mechanistic model developed in that chapter.

The operation specifications are as listed below:

Table 4-7: Operation specifications for section 4.2.5

Operation Name: 5-Axis Multi-Surface Surface Finish	*Coolant:* Air Blast
Feed Rate: 100mm/sec	*Immersion*: 0.25mm
Total Tolerance: 0.07mm	*Spindle speed:* 2500rev/min

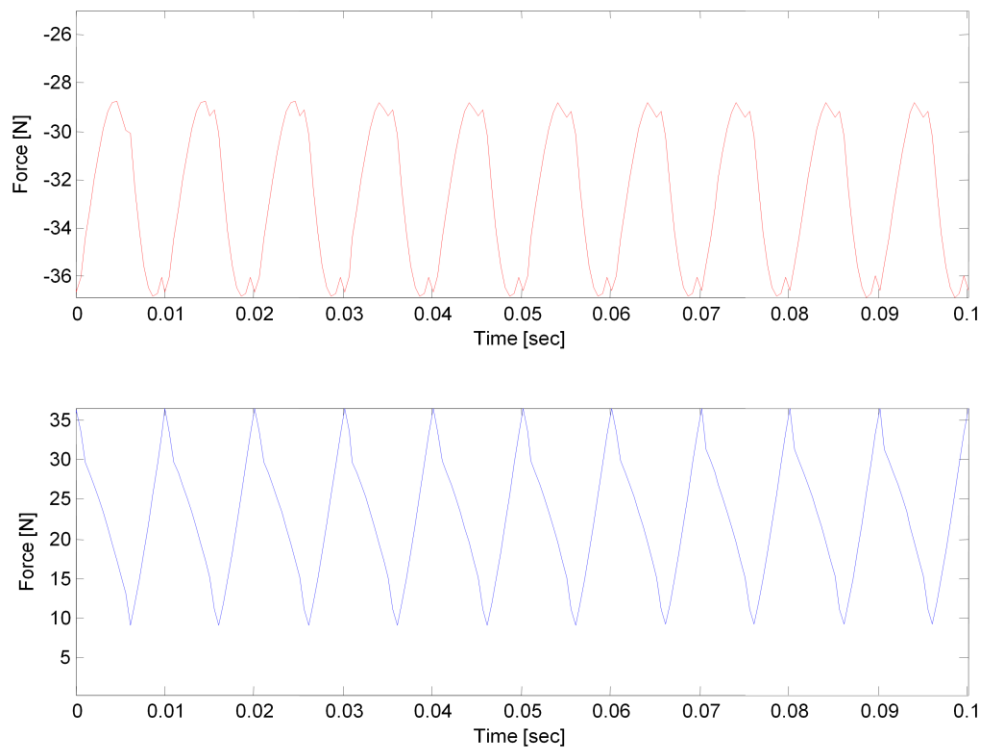The forces that are predicted are:
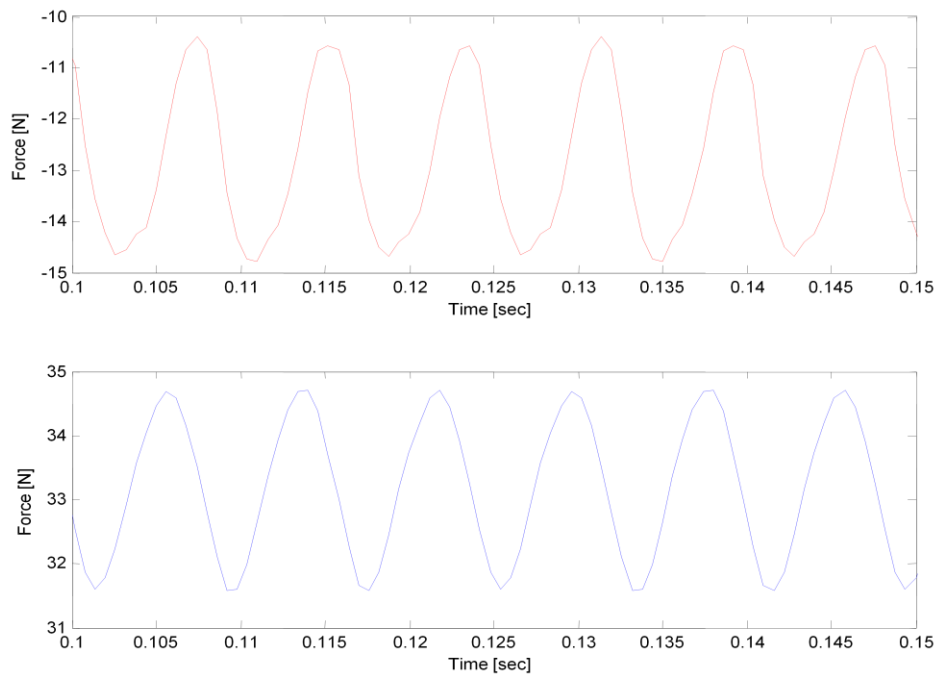
Figure 4-16: Predicted forces in the x(top) and y(bottom) axes using the mechanistic model developed in chapter 3. Note that these forces are predicted for the operation specifications shown in Table 4-7.

A snapshot of this surface finishing process is shown below:
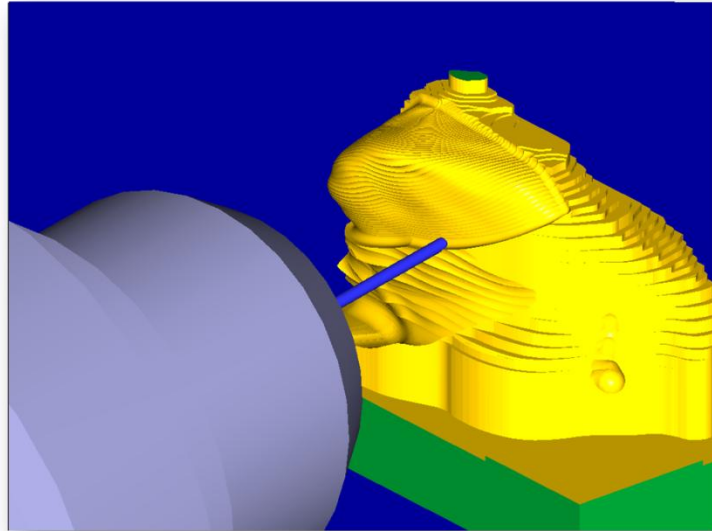
Figure 4-17: A snapshot of the surface finishing operation simulation, showing the emergence of the final surface from the rough shape of the implant.

After this stage of machining, the part will have the shape shown below:
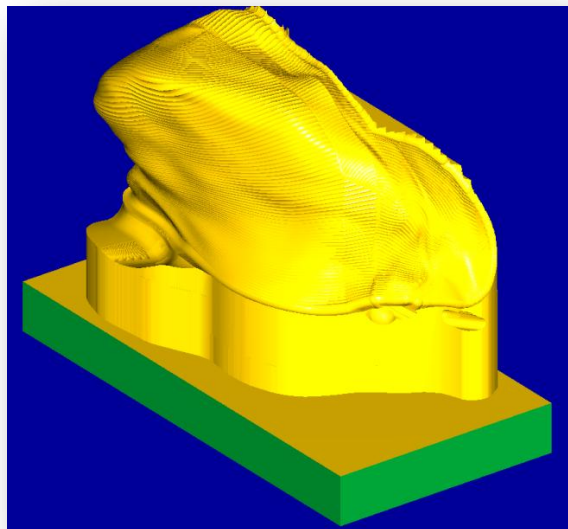
Figure 4-18: Simulated implant shape after the machining process in section 4.2.5

The machining of the remaining parts of the implant is described in the upcoming section. The remaining machining operation was mostly 3+2 axis operations and took much less time compared to the full five-axis operation that was described in this section.

4.2.6   3+2 Axis Machining and Final Drillings of the Implant

After completing the machining of the complex surfaces, the keel side of the implant was machined. The cylindrical part was machined using the same flat endmill that was used in 3-axis roughing in Section 4.2.3, in which a side milling approach is used to machine out the keel cylinder (see Table 4-2). Note that a step-down value of 2mm was used to reduce the amount of forces on the implant. The flat surface on the back also has been machined using the same tool in section 4.2.3, only this time an endmilling approach was used. Finally, the ball endmill used in the multi-axis finishing in Section 4.2.5 was used to machine where the cylindrical part which merges to the back flat surface of the bone (see Table 4-6). Below is a snapshot of the toolpaths generated to machine out the keel part of the implant. Note that the hole still needs to be drilled out in which the biodegradable screw will be inserted.
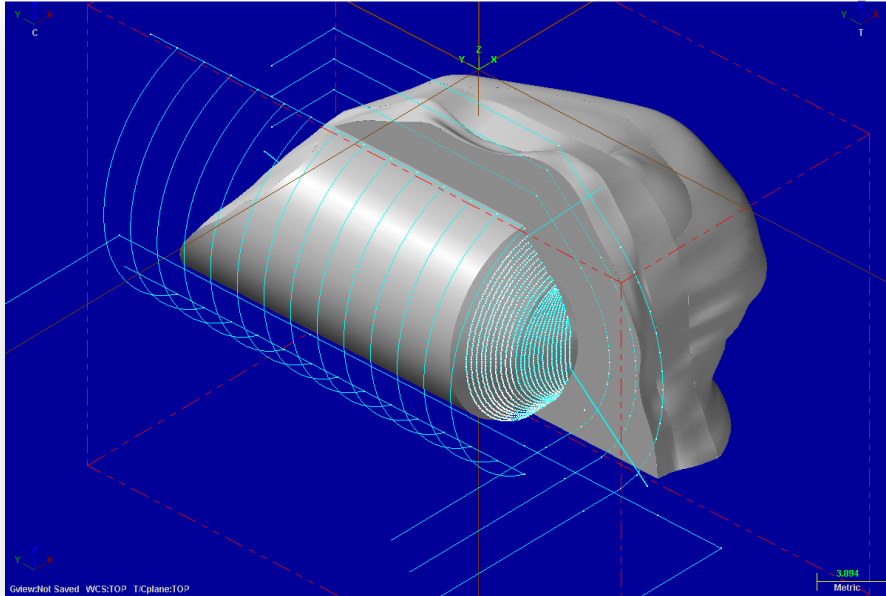
Figure 4-19: Keel section machining toolpaths for the implant.

To drill out the hole, two drills of different sizes were used, one being smaller than the other. Drilling the hole in one single operation (i.e. with one screw size) creates excessive forces that are too high and could potentially fracture the implant. Therefore, a smaller pilot hole is first drilled using the smaller drill specified in Table 4-8 and then the final hole is cut out using the drill as described in Table 4-9.

Table 4-8: Description of tool used in the first drilling operation for section 4.2.6 [48]

Metric 2mm Jobber Length Drill				
Cutting Diameter (mm)	Decimal Equivalent (in.)	Flute Length (mm)	Overall Length (mm)	H.S.S Code No.
2	0.0787	25.4	54	144-046

Table 4-9: Description of tool used in the second and final drilling operation for section 4.2.6 [48]

Metric 3.5mm Jobber Length Drill				
Cutting Diameter (mm)	Decimal Equivalent (in.)	Flute Length (mm)	Overall Length (mm)	H.S.S Code No.
3.5	0.1378	44.45	73	143-381

The operation parameters for both stages of drilling are as described below in Table 4-10. A peck drilling operation was used to evacuate CPP powder and prevent powder from either blocking the pores of CPP or accumulating inside the hole and as a result, breaking the implant from inside.

Table 4-10: Operation specifications for the final drilling process

Operation Name: Multi-Axis Peck Drilling	*Coolant:* Air Blast
Feed Rate: 75mm/sec	*Pecking Distance*: 2mm
Spindle speed: 2000rev/min	

Figure 4-20 shows a snapshot of the simulated machined keel portion of the implant.
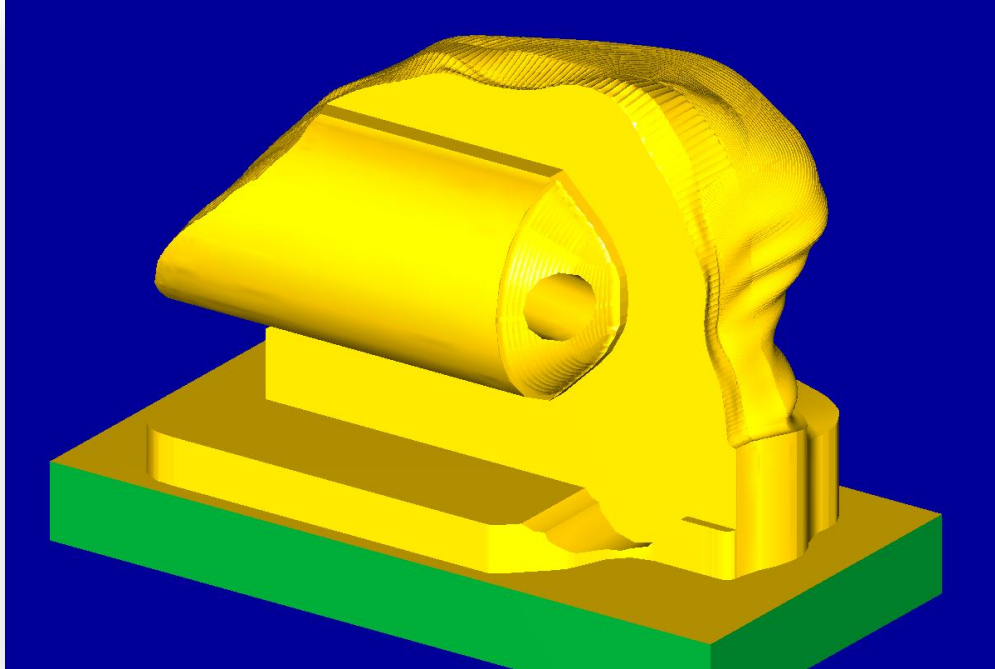
Figure 4-20: Simulated keel section of the implant after machining

4.2.7 Removing the Implant using Manual Milling

After completing the CNC, the implant was removed from the clamp. It still, however, needed to be detached from the blank it is sitting on. Although the implant design has a flat surface on the side which can be milled off using a manual or CNC milling machine, a manual milling approach is recommended as it is a simple face milling operation.

To perform this operation, the implant was clamped again only this time there were no flat surfaces to clamp but rather complex freeform surfaces. In order to clamp a part with complex 3-dimensional surfaces on the side, a block was developed which had one flat side to sit on the vice and the other side was the negative mould of the implant. This secured the implant in the clamp and enabled milling of the exposed side.

The clamp was made of two pieces, one grabbing the side with the freeform surface and the other piece holding the keel side of the implant. To generate the reverse molding surfaces of these implants, a Boolean operation was used in CAD software and the implant was subtracted from a block of material, resulting in a surface that exactly fit the implant's machined surface.

The clamp was machined from prototyping wax, which is easy to machine and also provides a degree of force and vibration damping due to its softer nature. Since wax is quite soft and might penetrate into the porous surface of the implant when it comes in contact with CPP, the implant was wrapped in Teflon tape to prevent any clogging and transfer of wax into this material. The implant was then cleaned afterwards using an ultrasonic cleaner to remove any contamination that might have entered the implant during the machining process.

The first piece of the clamp was generated in SolidWorks®, imported to MasterCAM® and the resulting part is as shown below in Figure 4-21.
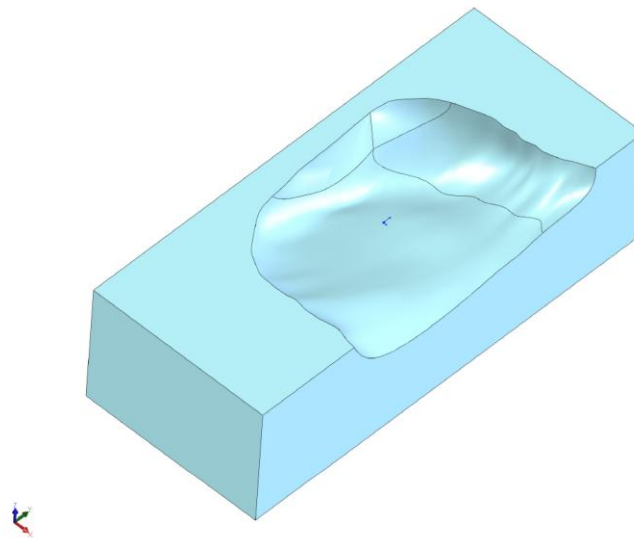
Figure 4-21: The first piece of the clamp for section 4.2.7, showing the surface where it will come in contact with the implant's freeform surface.

A multi-axis machining approach was required to machine this part of the clamp. As stated before, the toolpaths were designed using CAM software and the clamp was machined on the DMG multi-axis CNC machine.

The second part of the clamp was more simple and fit on the keel of the implant, as shown below in Figure 4-22.
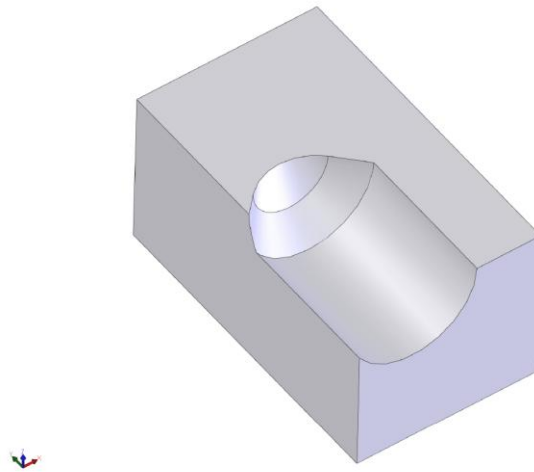
Figure 4-22: The second piece of the clamp for section 4.2.7, showing the surface where it will come in contact with the implant's keel side.

In order to visualize how the clamp parts come in contact with the implant, an exploded view of the clamp-part assembly, followed by a final clamped figure, is shown below.
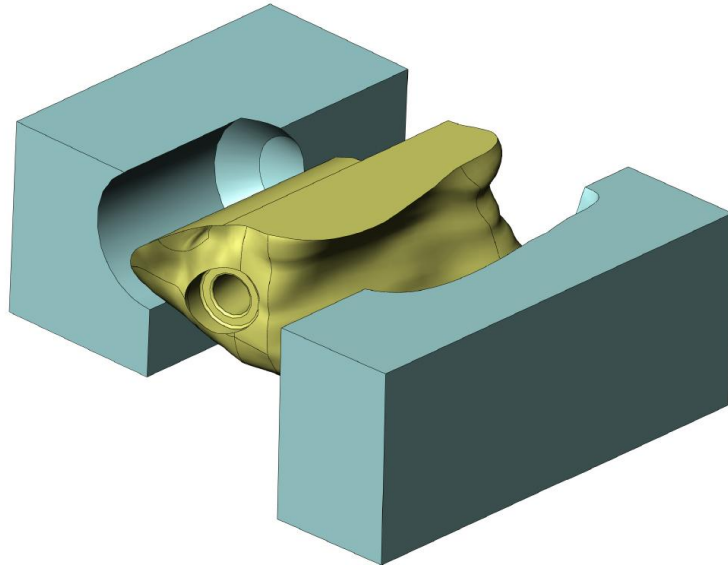
Figure 4-23: An exploded view of the final clamping of the implant, showing the implant in the center and the clamps on the sides.
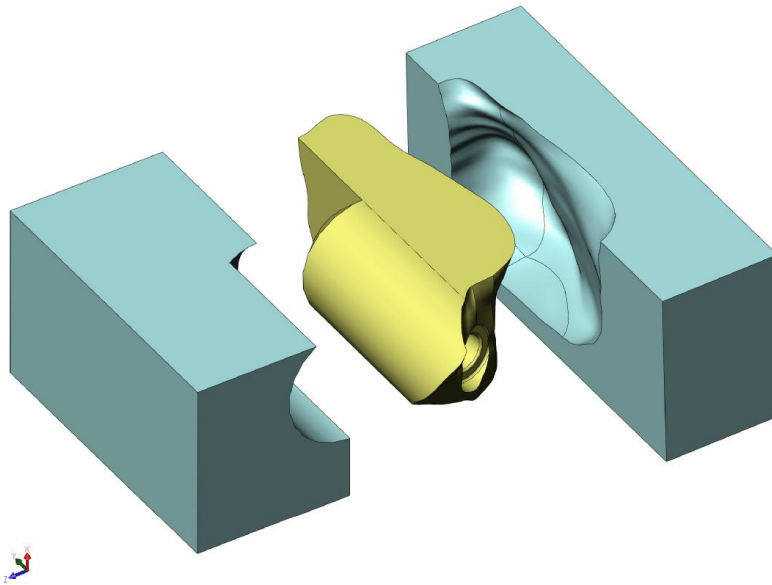
Figure 4-24: An exploded view of the final clamping of the implant from a different angle, showing the implant in the center and the clamps on the sides.

When assembled in the clamped position, the whole assembly is as shown below in Figure 4-24 and Figure 4-25.
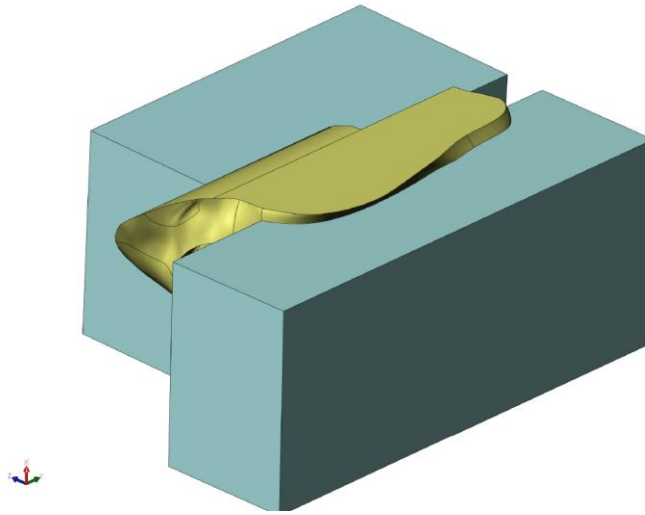
Figure 4-25: Final assembly of the part-implant clamping, showing the flat surfaces that will come in contact with the vice's clamping jaws.
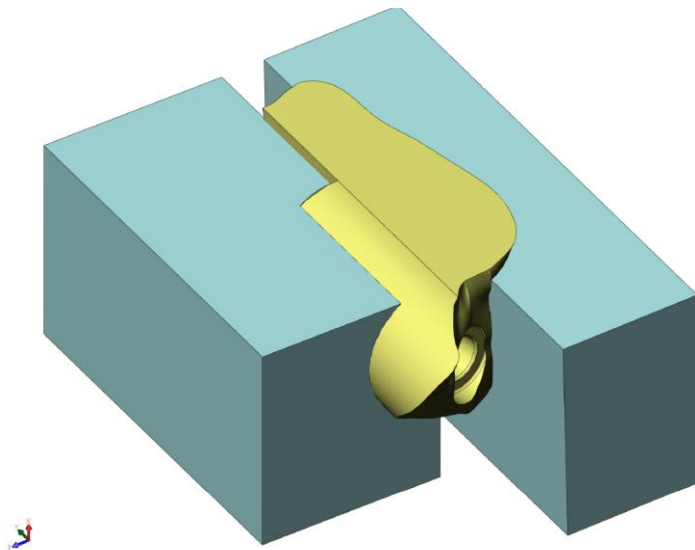
Figure 4-26: Final assembly of the part-implant clamping from a different angle, showing the flat surfaces that will come in contact with the vice's clamping jaws.

4.2.8   Post-Processing

Once the toolpath design was complete, the toolpaths were translated into machine interpretable code. It is important to check any generated code from a CAM program manually before executing the code on the machine. Any error in the generated code originating from the source (such as bugs in the CAM software or the post-processor translation) could cause catastrophic incidents on the machine, leading to machine damage or even operator injury and death.

The most commonly used controller language is a language called G-Code, which is widely used in most controllers developed in North-America. However, the TNC controller uses a different language. For more information on the specific commands and what each command does, the reader is referred to reference [59]. The toolpaths described in this section were then translated and a machine interpretable file was generated. The file had a size of 7 Mb and almost 160,000 lines.

4.2.9   DMG 80 P hi-dyn Universal Milling Machine

As explained in section 4.1.3, the Deckel Maho Gildemeister (DMG) 80 P hi-dyn machine is a 5-axis universal milling machine with a trunnion table mounted on the y axis[58]. Equipped with a swivel spindle head and a TNC 426 M controller from Heidenhain, this machine is capable of milling complex 3-dimensional surfaces, including the implant that requires full five axis machining. A picture from the machine as mounted in the Computer Integrated Manufacturing Laboratory (CIMLab) at the University of Waterloo (Waterloo, Ontario, Canada) is shown in Figure 4-5. This machine was used to manufacture the final implant. For more information on this machine and its technical specifications, refer to Appendix 2.

4.2.10 Part Setup

Multi-axis toolpaths usually have a higher risk of collision between the moving parts which can result in property damage and/or personal injury. Thus, the CPP block must be located further away from the table and clamping device to prevent collision. This was done using LePage (Henkel Consumer Goods of Canada, Inc., OakVille, Ontario, Canada, L6M 3E3) 12 Epoxy Glue to attach the base of the CPP block to the top of a long and sturdy aluminum column. This Column was then clamped vertically to introduce space between the clamp and the spindle and provide enough distance in between to enable safe machining. The aluminum rod had dimensions of 20x35x200mm.

After completing the multi-axis part of the machining, the block was detached from the aluminum base by sawing the implant's base using a band saw. Using the wax clamps that were machined before (section 4.2.7), the implant was clamped on a manual milling machine and the residue material was milled out to create the flat surface on the implant's side.

This process was first tested on a column of wax before an attempt to machine the actual implant. A wax prototype of the implant is also helpful to check the toolpaths for collision and errors on wax which is a safe and inexpensive method of checking the toolpaths. Also, as it will be discussed in more detail in section 4.2.11, this prototype was placed under an optical microscope to verify and inspect the toolpath's marks and surface finish. During the machining process, a Renishaw MP10 (Renishaw plc, GL12 8JR, UK) touch probe was used to set the datum and therefore increase accuracy. Ideally, machined parts should be validated against the actual CAD model using a coordinate measuring machine (CMM). This however, was not performed here since such machine was not available at time.

4.2.11 Implant Wax Prototype

The actual machining was first done on a wax prototype to verify the machining process. Subsequently, the wax prototype was put under an optical microscope and the following images were captured:
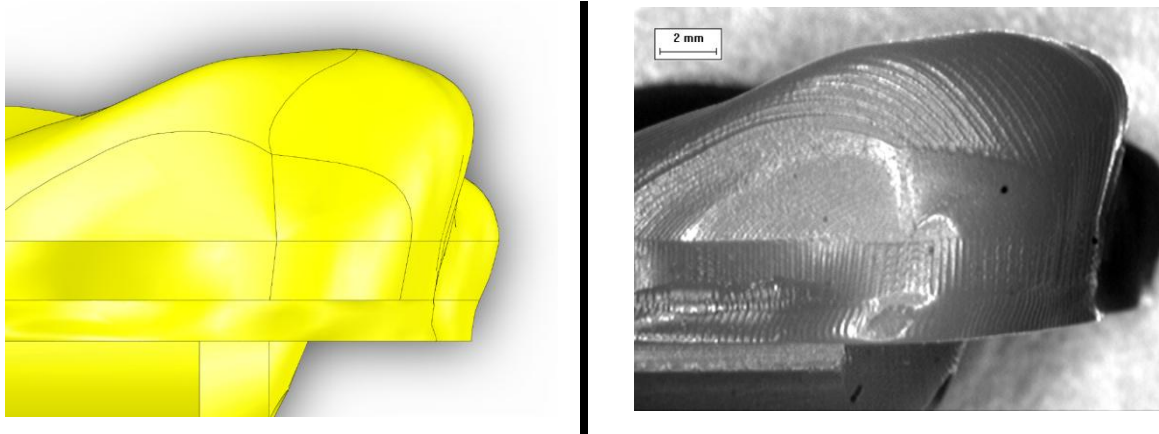
Figure 4-27: CAD and machined comparison of the top surface of the implant, where on left is the CAD model and on right is the machined substrate prototype from wax. Note that the multi-axis toolpaths are visible on the surface of the wax. The machined surface closely replicates the implant design, as it can be seen in the above figure.
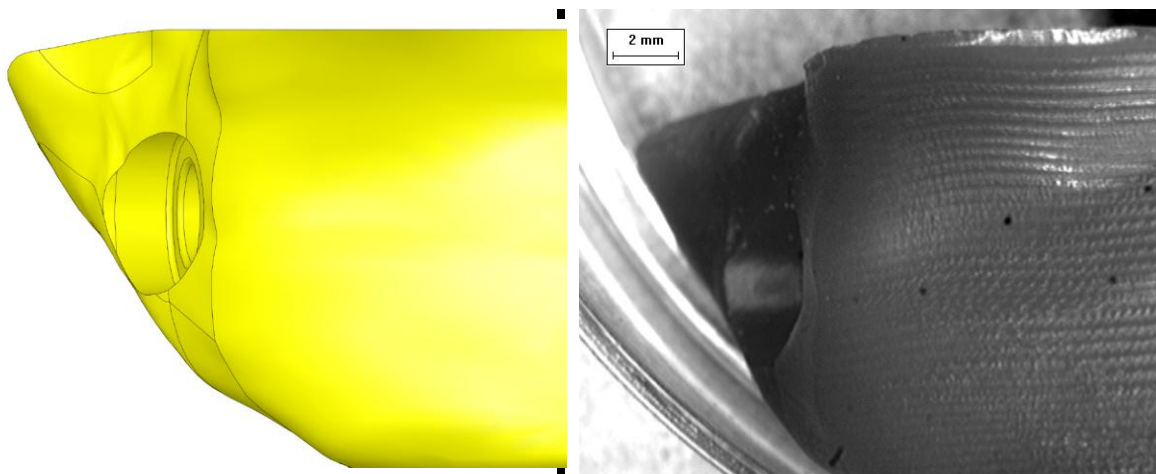
Figure 4-28: CAD and machined comparison of the side-front surface of the implant, where on left is the CAD model and on right is the machined substrate prototype from wax.
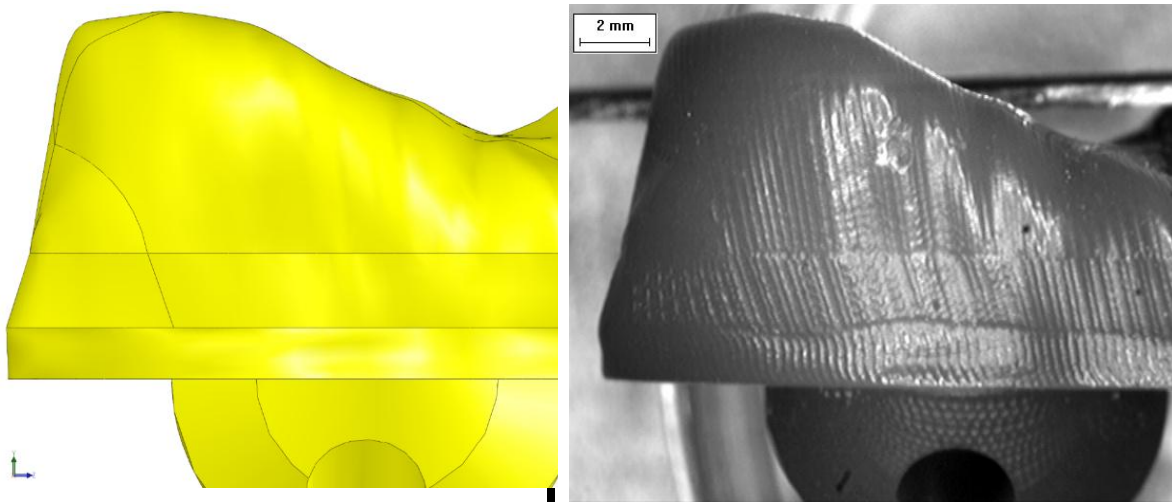
Figure 4-29: CAD and machined comparison of the back surface of the implant, where on left is the CAD model and on right is the machined substrate prototype from wax.

The above figures show that there is an absolutely satisfying correlation between the prototype implant and the CAD model developed previously. This enables proceeding to the final implant machining from CPP, which is to be presented in the next section.

4.2.12 Machined CPP Implant

After setting up the CPP block on the machine as described in section 4.2.10, the machine executable codes are uploaded to the CNC controller and executed for the machining to take place. The machining operation took from 3 to 5 hours in each case depending on the quality of the sintered CPP block, since, low quality blocks with cracks and cavities required lower feed rates and thus longer machining time to prevent chipping and breakage. The feedrates were manually reduced on the fly, by obtaining visual feedback at different phases of the machining process. If cracks or chipping was observed, particularly in low density blocks, feedrate was reduced. Otherwise, the programmed feeds and speeds were used. The final implant was machined and then cleaned using ultrasonic cleaning protocol of pure ethanol alcohol with 3 x 15min cleaning. After each

15 minute cleaning interval the solution is changed and the ethanol is replaced. Figure 4-30 shows the final implant compared with the original CAD model.
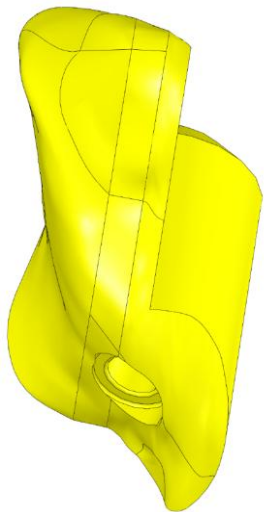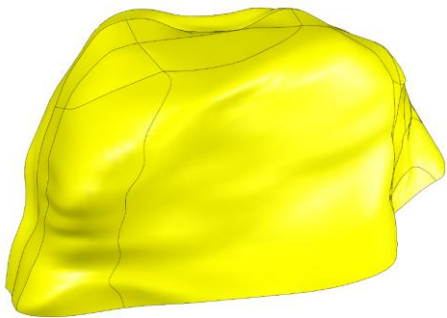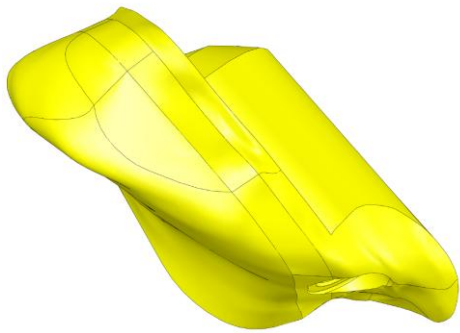
Figure 4-30: Final CPP Implant comparative figures from different angles, showing the CAD model on the left and the machined part on the right. Note that surface quality is acceptable and chipping is kept low and is not significant.

The above figure shows that the resulting machined implant closely resembles the intended CAD model. An optical microscope was used again to verify the surface quality and detect any possible fractures or significant chippings that may make this substrate unsuitable for surgical implantation.
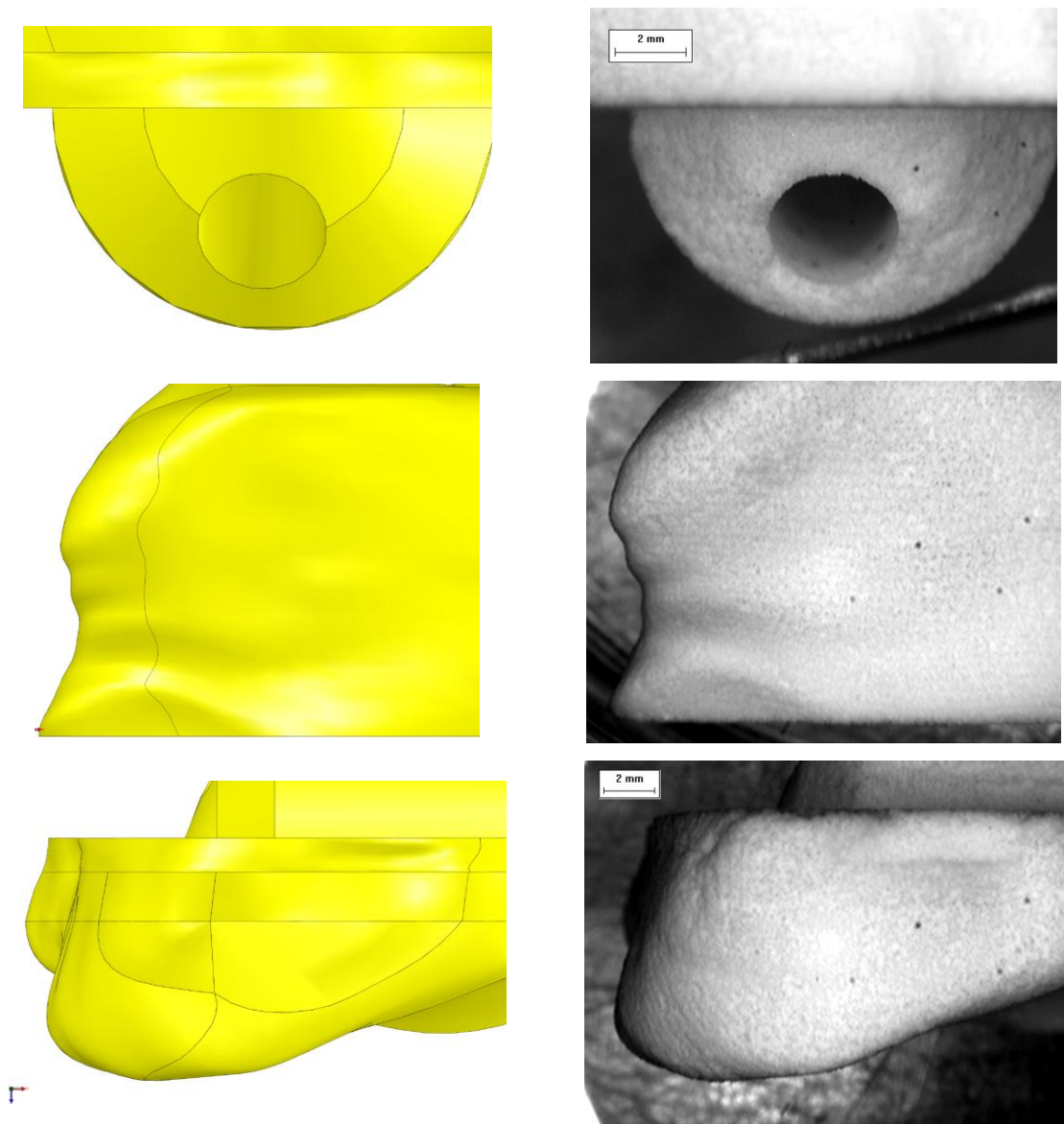
Figure 4-31: Optical microscope comparative images of the CPP implant on the right, compared with the CAD model on the left. Very good correlation between the two is seen from this qualitative comparison.

As it can be observed from the figures presented in this chapter, the machining process was successful and the implant shaped from CPP closely matches the CAD model from CT scan data. Actual measurement using a Coordinate Measuring Machine (CMM) would provide further validation on the accuracy achieved using the developed

CNC machining protocol, which is planned for continuation studies after this thesis. In overall, it can be stated that a manufacturing method for this implant has been successfully developed and validated.

4.2.13   Conclusion

This chapter started with a brief introduction to CAD and CAM, followed by presentation of the implant CAD model developed at Ryerson University. Some insight to CAM software and different milling machines was provided followed by a more detailed look at the proposed software and machine with which the implant was shaped.

Considering the requirements for the toolpath design, the universal multi-axis machine and some of its characteristics were introduced as well as some notes on part setup and safety. The machining process and the toolpaths were developed considering both the geometry of the implant as well as the cutting process model identified in Chapter 3. The developed machining method was first tested on prototyping wax, which proved successful. After this trial, the same machining procedure was performed on CPP and the final implant was successfully manufactured. The implant was again checked for chipping and surface quality using an optical microscope. The results were highly acceptable. The implant was delivered to the partner team at University of Toronto for implantation into sheep at University of Guelph.

Chapter 5

Final Results, Future Work and Conclusions

This thesis has studied the viability of using CNC machining techniques to shape biologically compliant constructs out of Calcium Polyphosphate substrate, for use in tissue engineered biomedical implants. After introducing the concept of implants for synovial joint defect repair and statement of thesis goals, Chapter 2 has provided a review of available literature related to different implant material, and specifically CPP, as well as a look at the background literature on orthogonal cutting and oblique cutting. A mechanistic model was then successfully developed and verified for CPP, and found the cutting coefficients to be as followed for a 70% density, 50-150 micron block of CPP based on the averaged cutting coefficients:

Table 5-1: Final cutting coefficients for 70%, 50-150 micron CPP

$K_{te}\left[\dfrac{N}{mm}\right] = 3.155$	$K_{tc}\left[\dfrac{N}{mm^2}\right] = 225.887$
$K_{re}\left[\dfrac{N}{mm}\right] = 0.896$	$K_{rc}\left[\dfrac{N}{mm^2}\right] = 134.161$
$K_{ae}\left[\dfrac{N}{mm}\right] = 0.161$	$K_{ac}\left[\dfrac{N}{mm^2}\right] = 12.72$

This model was verified by first simulating the cutting forces in the x, y, and z axes for a flat endmilling operation, and it was observed that the predicted forces matched the actual captured forces with the dynamometer fairly close. This verification was then extended to a ball endmilling cutting force comparison which also confirmed that the model was sufficient in predicting the cutting forces. It was also observed that the cutting forces in the z axis were very small and mostly buried in noise. Using SEM imaging, various cutting conditions with different feed rates and spindle rotational speeds were investigated for surface porosity quality and chipping presence. It was concluded that smaller diameter mills with diameters around 2mm to a maximum of 4mm, small depth of cuts to a maximum of 3mm, and half immersion is highly preferred to prevent chipping. The spindle rotational speed is to be kept at 1500rev/min to a maximum of 2500rev/min where chipping starts to happen. The cutting speed (tangential velocity of the teeth) is to be kept between 100 to 350mm/sec. The forces acting on the x or y axis at anytime should be kept below 45Newtons. It was also concluded that in high feed rates where the forces are high, tool vibration and static deflection play an important role and should be considered and modeled in future work. It was observed that at very high spindle speeds such as 12000rev/min, CPP reacts with absolute loss of surface porosity, resulting in an unwanted glossy surface.

In Chapter 4, the knowledge gained from the previous section in optimal cutting conditions and force predictions were put into use in multi-axis toolpath planning. By introducing the intended CAD design of the implant, this model was imported to the CAM software and then the machining toolpath was designed that would shape a block of CPP to the desired implant shape. In the first three cutting stages, a bulk amount of material is removed to roughly machine out the implant's shape. This is followed by multi-axis cutting toolpaths that generate the implant's surface. The drilling operation concludes machining of the five sides of the implant, while the last side remains. To machine the last side of the implant, two wax molds were machined and used to clamp the implant from both sides while the final side was being milled on a manual milling

machine. This step could also have been realized on the CNC machine. In planning all of the toolpaths, the spindle speeds and milling direction were chosen to retain porosity, while the immersion and feed conditions were chosen to keep the maximum cutting forces below the limit of chipping, which was observed at 45 Newtons. The toolpaths were tested on a block of wax, and the resulting wax prototype was investigated against the actual CAD model by an optical microscope. The same toolpaths were then executed on a block of CPP that was mounted on a column of aluminum which extended the position of the block away from the trunnion surface, thus reducing the risk of collision. The resulting CPP implant was compared with the CAD model using an optical microscope which showed that the actual machined sample and CAD model were practically identical. If further validation is required, as CMM can be used. Areas of future development are the inclusion of tool and material vibrations in the mechanistic model for better accuracy in the cutting force predictions. The use of 3+2 axis machining rather than full 5-axis machining can increase productivity and reduce machining time drastically. Also, if a close yet rough version of the implant can be generated using rapid prototyping methods, then the roughing stages of the machining plan can be trimmed, enabling greater productivity to be achieved and this will also reduce the amount of powder wasted in the machining process.

Recently, machining of polymer impregnated CPP has also been studied, which was not reported in this thesis. Polymer impregnation has allowed up to 3 times higher feed speeds to be achieved, promising at least 3-fold improvement in the productivity of the process. This is because the polymer adds damping to the CPP structure, allowing higher machining forces to be withstood without resulting in unwanted damage to the implant. Further studies to enhance the machinability characteristics of CPP through polymer impregnation are under investigation at the Precision Controls Laboratory at the University of Waterloo, in collaboration with researchers from University of Toronto.

References

[1]   Hjelle, K., Solheim, E., Strand, T., Muri, R. and Brittberg, M., (2002), "Articular Cartilage Defects in 1,000 Knee Arthroscopies", Arthroscopy: The Journal of Arthroscopic & Related Surgery", Vol. 18, Issue 7, Sep. 2002, pp. 730-734.

[2]   Armarego, E.J.H., Brown, R.H, (1969) "The Machining of Metals", Prentice-Hall.

[3]   Chang, C.H., Kuo, T.F., Lin, C.C., Chou, C.H., Chen, K.H., Lin, F.H., and Liu H.C., (2006), "Tissue engineering-based cartilage repair with allogenous chondrocytes and gelatin-chondroitin-hyaluronan tri-copolymer scaffold: a porcine model assessed at 18, 24, and 36 weeks", *Biomater.*, Vol. 27, pp. 1876-1888.

[4]   Soderman, P., Malchau, H., Herberts, P., Zügner, R., Regnér, H., and Garellick, G., (2001), "Outcome after total hip arthroplasty. Part II. Disease-specific follow-up and the Swedish national total hip arthroplasty register", *Acta. Orthop. Scand.*, Vol. 72 No. 2, pp. 113-119.

[5]   Moore, W.R., Graves, S.E., and Bain, G.I., (2001), "Synthetic bone graft substitutes", *ANZ J. Surg.*, Vol 71, pp. 354-361.

[6]   Wei C., (2007), "Rapid Fabrication Techniques for Anatomically-Shaped Calcium Polyphosphate Substrates for Implants to Repair Osteochondral Focal Defects", *Mater's Thesis,* University of Waterloo, 200 University Ave. West, Waterloo, Ontario Canada.

[7]   Kandel, R.A., Grynpas, M., Pilliar, R., Lee, J., Wang, J., Waldman, S., Zalzal, P., and Hurtig, M., (2006), "Repair of osteochondral defects with biphasic cartilage-calcium polyphosphate constructs in a sheep model", *Biomater.*, Vol. 27, pp. 4120-4131.

[8]   Waldman, S.D., Spiteri, C.G., Grynpas, M.D., Pilliar, R.M., Hong, J., and Kandel, R.A., (2003), "Effect of biomechanical conditioning on cartilaginous tissue formation *in vitro*", *J. Bone Joint Surg. Am.*, Vol. 85-A Suppl. 2, pp. 101-105.

[9]   Tanaka, T., Komaki, H., Chazono, M., and Fujii, K., (2005), "Use of a biphasic graft constructed with chondrocytes overlying a β-tricalcium phosphate

block in the treatment of rabbit osteochondral defects", *Tissue Eng.*, Vol. 11 No. 1/2, pp.331-339.

[10]   Schaefer, D., Martin, I., Jundt, G., Seidel, J., Heberer, M., Grodzinsky, A., Bergin, I., Vunjak-Novakovic, G., and Freed, L.E., (2002), "Tissue-engineered composites for the repair of large osteochondral defects", *Arthritis Rheum.*, Vol. 46 No. 9, pp. 2524-2534.

[11]   Gao, J., Dennis, J.E., Solchaga, L.A., Goldberg, V.M., and Caplan, A.I., (2002), "Repair of osteochondral defect with tissue-engineered two-phase composite material of injectable calcium phosphate and hyaluronan sponge", *Tissue Eng.*, Vol. 8 No. 5, pp. 827-837.

[12]   Pilliar, R.M., Filiaggi, M.J., Wells, J.D., Grynpas, M.D., and Kandel R.A., (2001), "Porous calcium polyphosphate scaffolds for bone substitute applications - *in vitro* characterization", *Biomater.*, Vol. 22 No. 9, pp. 963-972.

[13]   Baksh, D. and Davies, J.E., (1998), "Three-dimensional matrices of calcium polyphosphates support bone growth *in vitro* and *in vivo*", *J. Mater. Sci.*, Vol. 9, pp. 743-748.

[14]   Qiu, K., Wan C.X., and Zhao, C.S., (2006), "Fabrication and characterization of porous calcium polyphosphates scaffolds", *J. Mater. Sci.*, Vol. 41, pp. 2429-2434.

[15]   Waldman, S.D., Grynpas, M.D., Pilliar, R.M., and Kandel, R.A., (2002), "Characterization of cartilaginous tissue formed on calcium polyphosphate substrates *in vitro*", *J. Biomed. Mater. Res.*, Vol. 62 No. 3, pp. 323-330.

[16]   Ciolfi, V.J.D., Pilliar, R., McCulloch, C., Wang, S.X., Grynpas, M.D., and Kandel, R.A., (2003), "Chondrocyte interactions with porous titanium alloy and calcium polyphosphate substrates", *Biomater.*, Vol. 24, pp. 4761-4770.

[17]   Chen, F., Mao, T., Tao, K., Chen, S., Ding, G., and Gu, X., (2002), "Bone graft in the shape of human mandibular condyle reconstruction via seeding marrow-derived osteoblasts into porous coral in a nude mice model", *J. Oral Maxillofac. Surg.*, Vol. 60, pp. 1155-1159.

[18]   Hamilton, D.J., Séguin, C.A., Wang, J., Pilliar, R.M., and Kandel R.A., (2006), "Formation of nucleus pulposus-cartilage endplate construct *in vitro*", *Biomater.*, Vol. 27 No. 3, pp. 397-405.

[19]   Ahmad, C.S, Cohen, Z.A., Levine, W.N., Ateshian, G.A., and Mow, V.C., (2001), "Biomechanical and topographic considerations for autologous osteochondral in the knee", *Am. J. Sports Med.*, Vol. 29 No. 2, pp. 201-206.

[20]   Hench, L.L. and Best, S., (2004), Ceramics, Glass, and Glass Ceramics. *Biomaterials Science: An Introduction to Materials in Medicine*. Edited by Ratner, B.D., Hoffman, A.S., Schoen, F.J., and Lemons, J.E., Elsevier Academic Press, London, pp 153-170.

[21]   Roy, T.D., Simon, J.L., Ricci, J.L., Rekow, E.D., Thompson, V.P., and Parsons, J.R., (2003), "Performance of hydroxyapatite bone repair scaffolds created via three-dimensional fabrication techniques", *J. Biomed. Mater. Res.*, Vol. 67A, pp. 1228-1237.

[22]   Erbe, E.M., Marx, J.G., Clineff, T.D., and Bellincampi, L.D., (2001), "Potential of an ultraporous β-tricalcium phosphate synthetic cancellous bone void filler and bone marrow aspirate composite graft", *Eur. Spine J.*, Vol 10 Suppl., pp. 141-146.

[23]   Eggli, P.S., Moller, W., and Schenk, R.K., (1988), "Porous hydroxyapatite and tricalcium phosphate cylinders with two different pore size ranges implanted in the cancellous bone of rabbits: A comparative histomorphometric and histologic study of bony ingrowth and implant substitution", *Clin. Orthop. Res.*, Vol. 232, pp. 127-138.

[24]   Kitsugi, T., Yamamuro, T., Nakamura, T., Kotani, S., Kokubo, T., and Takeuchi, H., (1993), "Four calcium phosphate ceramics as bone substitutes for non-weight-bearing" *Biomater.*, Vol. 14 No. 3, pp. 216-224.

[25]   Grynpas, M.D., Pilliar, R.M., Kandel, R.A., Renlund, R., and Filiaggi, M., (2003), "Porous calcium polyphosphate scaffolds for bone substitute applications - *in vivo* studies", *Biomater.*, Vol. 23 No. 9, pp. 2063-2070.

[26]   Vaccaro, A.R., (2002), "The role of the osteoconductive scaffold in synthetic bone graft", *Orthopedics*, Vol. 25 No. 5 Suppl., pp. 571-578.

[27]   Porter, N.L., Pilliar, R.M., and Grynpas, M.D., (2001), "Fabrication of porous calcium polyphosphate implants by solid freeform fabrication: A study of processing parameters and *in vitro* degradation characteristic", *J. Biomed. Mater. Res.*, Vol. 56, pp. 504-515.

[28]   de Groot, K., Klein, C.P.A.T., Wolke, J.G.C., and de Blieck-Hogervorst, J.M.A.,
           (1990), Chemistry of Calcium Phosphate Bioceramics. *CRC Handbook of
           Bioactive Ceramics: Volume II Calcium Phosphate and Hydroxyapatite
           Ceramics*. Edited by Yamamuro, T., Hench, L.L., and Wilson, J., CRC
           Press, Boca Raton.

[29]   LeGeros, R.Z., (1993), "Biodegradation and bioresorption of calcium phosphate
           ceramics", *Clin. Mater.*, Vol. 14, pp. 65-88.

[30]   van Noort, R., (2002), Dental Ceramics. *Introduction to Dental Materials*. Mosby,
           Toronto, pp. 231-246.

[31]   Waldman, S.D., Spiteri, C.G., Grynpas, M.D., Pilliar, R.M., and Kandel, R.A.,
           (2004), "Long-term intermittent compressive stimulation improves the
           composition and mechanical properties of tissue-engineered cartilage",
           Tissue Eng., Vol. 10 No. 9/10, pp. 1323-1331.

[32]   Waldman, S.D., Spiteri, C.G., Grynpas, M.D., Pilliar, R.M., and Kandel, R.A.,
           (2003), "Long-term intermittent shear deformation improves the quality of
           cartilaginous tissue formed *in vitro*", *J. Orthopaedic Res.*, Vol. 21, pp.
           590-596.

[33]   Altıntas, Y., (2000). *Manufacturing Automation: Principles of Metal Cutting and
           Machine Tool Control. Cambridge University Press*. ISBN 0521659736.

[34]   Zhang, W.-Y., Gao, H., Li, B.-Y., and Jiao, (2006), "A novel route for fabrication
           of machinable fluoramphibole glass-ceramics", *Scripta Materialia*, Vol.
           55, pp. 275-278.

[35]   Kasuga, T., Terada, M., and Nogami, M., (2001), "Machinable calcium
           pyrophosphate glass-ceramics", *J. Mater. Res.*, Vol. 16 No. 3, pp. 876-
           880.

[36]   Wang, T.H. and James, P.F., (1990), "A new machinable phosphate based glass
           ceramics", *Inst. Physics. Conf. Ser.*, Vol. 111, pp. 401-410.

[37]   Corning Inc., Professional Plastic, Macor Machining. Copyright © 2006 Corning
           Inc.
           http://www.professionalplastics/professionalplastics/content/MacorMachi
           ning.doc Date accessed: May 2007.

[38]   Mitamura Y, Hosooka K, Matsumoto T, Otaki K, Sakai K, Tanabe T, Yuta T, Mikami T., (1989), "Development of a Ceramic Heart Valve", Journal of Biomedical Applications, Sage Publications, Jul;4(1):33-55.

[39]   Filser, F., Lüthy, H., Schärer, P., and Gauckler, L., (1998), All-ceramic dental bridges by direct ceramic machining (DCM). *Materials in Medicine, Materials Day, Department of Materials*. Edited by Speidel, M.O., Uggowitzer, P.G., and vdf Hochschulverlag, A.G., ETH Zürich, Zurich, pp. 165-189.

[40]   Al-Shammery, H.A.O., Wood, D.J., Bubb, N.L., and Youngson, C.C., (2004), "Novel machinable mica based glass ceramics for dental applications", *Glass Technol.*, Vol. 45, pp. 88-90.

[41]   Hung, C.T., Lima, E.G., Mauck, R.L., Taki, E., LeRoux, M.A., Lu, H.H., Stark, R.G., Guo, X.E., and Ateshian, G.A., (2003), "Anatomically shaped osteochondral constructs for articular cartilage repair", *J. Biomechanics*, Vol. 36, pp. 1853-1864.

[42]   Engin, S., Altintas, Y., and Amara, F.B., (2000), "Mechanics of routing medium density fiberboard", *Forest Products J.*, Vol. 50 No. 9, pp. 65-69.

[43]   Shaw, M.C., "Metal Cutting Principles", (1984), Oxford University Press.

[44]   Oxley, P. L. B., "The Mechanics of Machining", (1989), Ellis Horwood Limited.

[45]   Merchant, M. E., (1945), "Mechanics of Metal Cutting Process, ii. Plasticity Conditions in Orthogonal Cutting", *Journal of Applied Physics,* vol. 16, pp. 318-324.

[46]   Lee., E. H., Shaffer, B. W., (1951), "Theory of Plasticity Applied to The Problem of Machining", Vol. 18, pp. 405-413.

[47]   Avallone, E.A.; Baumeister, T., III (1996). Marks' Standard Handbook for Mechanical Engineers (10th Edition). (pp. 13-46). McGraw-Hill. Online version available at: http://www.knovel.com/knovel2/Toc.jsp?BookID=346&VerticalID=0

[48]   Sowa Tool and Machine Co. Ltd., *Sowa Tooling Solutions, Catalogue #ST0906*, http://www.sowatool.com/catalogue/carbide_endmills.html. Date accessed: July 2007.

[49]   Budak, E., Altıntas, Y., and Armarego, E.J.A., (1996), "Prediction of milling
        force coefficients from orthogonal cutting data", *J. Manuf. Sci. Eng.*, Vol.
        118, pp. 216-224.

[50]   Kline, W.A., DeVor, R.E., and Lindberg, J.R., (1982), "The prediction of cutting
        forces in endmilling with application to cornering cuts", *Intl. J. Mach.
        Tool Des. Res.*, Vol. 1, pp. 7-22.

[51]   Kline, W.A. and DeVor, R.E., (1983), "The effect of runout on cutting geometry
        and forces in endmilling", *Intl. J. Mach. Tool Des. Res.*, Vol. 23 No. 2/3,
        pp. 123-140.

[52]   Feng, H.Y. and Su, N., (2001), "A Mechanistic Cutting Force Model for 3D Ball-
        endmilling", *J. Manuf. Sci. Eng.*, Vol. 123, pp. 23-29.

[53]   Altintas, Y., Spence, A., (1991), "Endmilling Force Algorithms for CAD
        Systems", *Annals of the CIRP*, 40(1):31-34.

[54]   Spence, A., Altintas, Y., (1994), "A Solid Modeller Based Milling Process
        Simulation and Planning System", *Trans. ASME Journal of Engineering
        Industry*, 116(1): 61-69.

[55]   Morris, Peter W.G.; Pinto, Jeffrey K. "Wiley Guide to Managing Projects", John
        Wiley & Sons., pp. 440-441 Online version available at:
        http://www.knovel.com/knovel2/Toc.jsp?BookID=1686&VerticalID=0

[56]   Blanchard, Benjamin S., " System Engineering Management (3rd Edition)",
        John Wiley & Sons., pp. 221, Online version available at:
        http://www.knovel.com/knovel2/Toc.jsp?BookID=1415&VerticalID=0

[57]   Dudi, A. and Papini, M., (2007), "Design of a Prototype Bioresorbable Tibial
        Implant in a Sheep Model", *Proc. of 21st Canadian Congress of Applied
        Mechanics (CANCAM'07)*, Toronto, ON, June 3-7.

[58]   The DMU P hi-dyn series machine brochure, DMG website, Accessed May 2007,
        http://www.gildemeister.com/home,en

[59]   HEIDENHAIN Technical Manual for TNC 426 CB/PB/M and TNC 430
        CA/PA/M, February 2001, available at http://www.heidenhain.com/

Appendices

Appendix A

Table A-1 summarizes the average magnitude of the forces in the x, y and z direction for layers 1, 3 and 4. For further information, please refer to section 3.5.3. Note that the depth of cut for layer 1 was 1.5mm while this value was 2.5mm for layers 3 and 4.

Table A-1: Average cutting forces for layers 1,2, and 4 in the x, y and z axes.

Layer	c (mm/min)	h (mm/tooth)	Measured $F_x(N)$	$F_y(N)$	$F_z(N)$
1	30	0.010	-1.087	3.254	-
1	75	0.025	-2.962	6.765	0.174
1	150	0.050	-6.276	5.259	0.357
1	225	0.075	-8.990	18.568	-0.072
1	300	0.100	-13.737	23.903	-0.242
1	450	0.150	-17.536	26.207	0.819
2	15	0.005	-1.989	7.409	-0.145
2	30	0.010	-3.682	8.892	0.005
2	75	0.025	-5.625	14.864	0.075
2	150	0.050	-10.165	20.784	0.161
2	225	0.075	-16.171	32.772	0.638
2	300	0.100	-20.577	51.772	5.098
4	15	0.005	-1.848	5.347	0.011
4	30	0.010	-4.155	8.158	-1.601
4	75	0.025	-5.966	9.824	-2.768
4	150	0.050	-10.415	18.036	-3.420
4	225	0.075	-12.881	20.683	-3.516
4	300	0.100	-12.992	26.439	-3.713
4	375	0.125	-22.611	40.796	-3.228

Appendix B

To provide the reader with some specifications on the machine that the implant was milled on, the following specification tables are provided. Table B-1 shows the general specifications of the machine, Table B-2 describes the rotary table specifications and finally, in Figure B-1, the rotational speed / performance diagram for the machine's spindle (HSK-A63 18000rev/min) spindle is shown.

Table B-1: Technical data for the DMG DMU 80 P hi-dyn machine [58]

Work Area	
X- / Y-/ Z- axes (mm)	800/700/600
Rotational speed range (rev/min)	20 – 12,000
Integrated motor spindle (40% DC) (kW/Nm)	20/121
Tool-holder standard	SK 40
Feed range (linear axes) (mm/min)	0 – 50,000
Rapid traverse (linear axes) (m/min)	50
Tool-holder standard	DIN 69872 A
Tool magazine (pockets)	60
NC rotary table (mm)	Ø 900 x 630
Control	TNC 426 M

Table B-2: NC Swivel-Rotary table for the DMG DMU 80 P Machine [58]

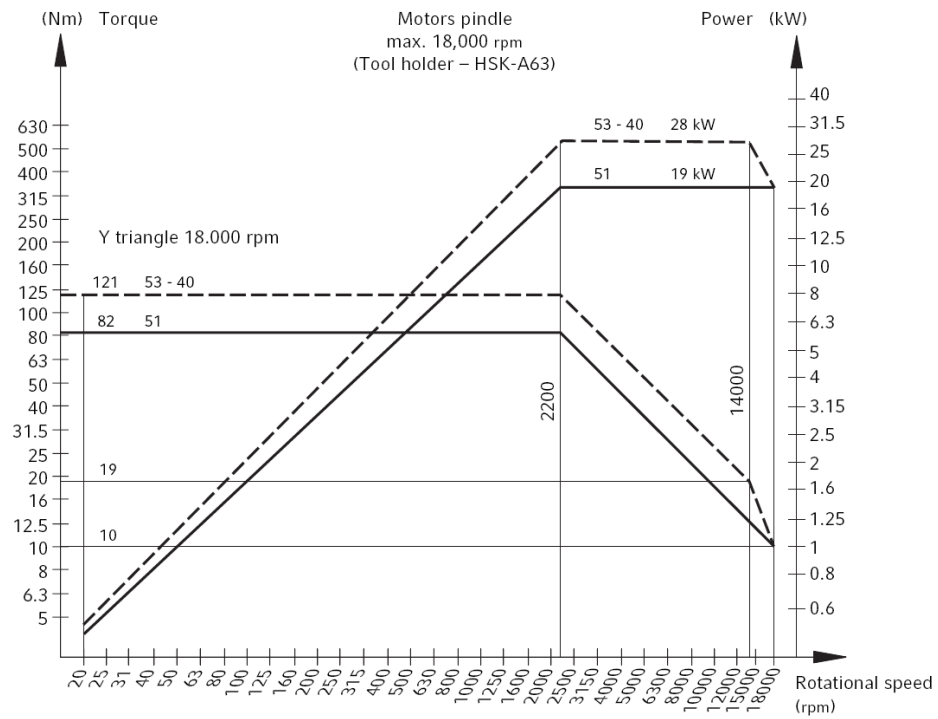|	
Clamping surface	Ø 630
Center bore	Ø 50 H6
Number / distance of T slots	9/63 – 14 H7
Max. table load	600
Rapid traverse Turning / Swivel	9.3/7.3
Feed Turning / Swivel	3,300/2,600

Figure B-1: Rotational speed / performance diagram for the DMG DMU 80 P hi-dyn 18,000 rev/min spindle (HSK-A63) [58]

126